MULTI-DIMENSIONAL CHARACTERIZATION OF BONE AND BONE-IMPLANT INTERFACES

MULTI-DIMENSIONAL CHARACTERIZATION OF BONE AND BONE-IMPLANT INTERFACES

By

XIAOYUE WANG B.S., M.ENG

A Thesis

Submitted to the School of Graduate Studies

In partial Fulfilment of the Requirements

For the Degree

Doctor of Philosophy

McMaster University

DOCTOR OF PHILOSOPHY (2017) McMaster University

(Materials Science and Engineering) Hamilton, Ontario, Canada

TITLE: Multi-Dimensional Characterization of Bone and Bone-Implant Interfaces

AUTHOR: Xiaoyue Wang B.S., M.Eng., (Sun Yat-Sen University, China)

SUPERVISOR: Prof. Dr. Kathryn Grandfield

NUMBER OF PAGES: XIV, 130

Abstract

Metallic bone implant devices are commonly used to tackle a wide array of bone failures in human patients. The success of such implants relies on the biomechanical and functional bonding between the living bone tissue and implant, a process defined as osseointegration. However, the mechanism of osseointegration is still under debate in the scientific community. One efficient method to help understand this complex process is to characterize the interface between human bones and implant devices after the osseointegration has been established, while another approach is to visualize mineralization in real-time under simulated body conditions. Both of these approaches to understand mineralization have been explored in this thesis.

Firstly, due to the inhomogeneous nature of bone and complex topography of implant surfaces, a suitable sample geometry for three-dimensional (3D) characterization was required to fully understand osseointegration. Electron tomography has been proven as an efficient technique to visualize the nanoscale topography of bone-implant interface in 3D. However, resulting from the thickness and shadowing effects of conventional transmission electron microscope (TEM) lamellae at high tilt angles and the limited tilt-range of TEM holders, “missing wedge” artifacts limit the resolution of final reconstructions. In Chapter 3, the exploration of a novel sample geometry to explore osseointegration is reported. Here, on-axis electron tomography based on a needle-shaped sample was applied to solve the problem of the “missing wedge”. This resulted in a near artifact-free 3D visualization of the structure of human bone and laser-modified titanium implant, showing bone growth into the nanotopographies of the implant surface and contributing to the evolution of the definition of osseointegration towards nano-osseointegration.

One of the key issues regarding the mechanism of osseointegration that remains is that of

the chemical structure at the implant interface, namely distribution of calcium-based and carbon-based components at the interface and their origins. Thus, the second objective of this thesis aimed to push characterization techniques further to four dimensions (4D), by incorporating chemical information as the fourth dimension after the spatial X,Y,Z coordinates. In Chapter 4, correlative 4D characterization techniques including electron energy-loss spectroscopy (EELS) tomography and atom probe tomography (APT) and other spectroscopy techniques were used to probe the nanoscale chemical structure of the bone-implant interface. This work uncovered a transitional biointerphase at the bone-implant interface, consisting of morphological and chemical differences compared to bone away from the interface. Also, a TiN layer between the surface oxide and bulk metal was identified in the laser-modified commercial dental implant. Both findings have implications for the immediate and long-term osseointegration.

Since bone formation at the implant interface is a dynamic process, which includes calcium phosphates (CaP) biomineralization as a basis of these reactions, the third objective of this work focused on exploring real-time mineralization processes. Liquid-phase transmission electron microscopy (LP-TEM) is a promising technique to enable real-time imaging with nanoscale spatial resolution and sufficient temporal resolution. In Chapter 5, by using this technique, we present the first real-time imaging of CaP nucleation and growth, which is a direct evidence to demonstrate that CaP mineralization occurs by particle attachment.

Overall, this thesis has applied state-of-the-art advanced microscopy techniques to enhance the knowledge and understanding of osseointegration mechanisms by investigating established biointerfaces and real-time mineralization. The developed correlative 4D tomography workflow is transferable to study other interfacial applications in materials science and biological systems, while the LP-TEM work forms

a basis for further mineralization research.

Key words: Osseointegration, bone-implant interface, electron tomography, atom probe tomography, liquid-phase TEM, 4D

Acknowledgements

First of all, I would like to express my gratitude to my supervisor, Prof. Kathryn Grandfield. I really appreciate your inspiring encouragement, continuous support and valuable guidance throughout my PhD study and research in McMaster University. Your diligence in work, enthusiasm on research and kindness in personality have influenced me deeply and set a great model for my career.

Also, I would like to thank all my committee members, Prof. Gianluigi Botton, Prof. Henry Schwarcz and Prof. Nabil Bassim, for your valuable time on evaluating my research work and insightful suggestions and comments. Additionally, I would like to acknowledge my collaborators, Prof. Anders Palmquist, Dr. Furqan Ali Shah, Prof. Leyla Soleymani, Prof. Adam Hitchcock, Prof. Matthieu Bugnet, Prof. Gregory Wohl and Jie Yang, for their significant contributions and help on the research projects.

Massive thanks to all the people I worked with in the Department of Materials Science and Engineering and Canadian Centre for Electron Microscopy. I would like to acknowledge Jane Mah, Dr. Xiaogang Li, Doug Culley, Dr. Glynis de Silveira, Dr. Andreas Korinek, Dr. Brian Langelier, Dr. Carmen Andrei, Travis Casagrande, Andy Duft and Chris Butcher, for their generous help and support during my study and research. I'm also grateful to the helps from Dr. Danielle Covelli and Elna Luckham in Biointerfaces Institute.

During my PhD, I had a nice and meaningful academic exchange experience in Pacific Northwest National Laboratory. I would like to express my gratitude to all the people I worked with there for their generous help and support. Sincere thanks to Dr. Arun Devaraj, Prof. Robert Schofield, Dr. Daniel E. Perea, Dr. Steven Spurgeon and Dr. Peter Sushko.

Especially, I'm grateful to my group members and friends I met during my PhD. I really enjoyed the wonderful time studying, researching and having fun together with you all! Many thanks to Bryan Lee, Dakota Binkley, Vicky Vuong, James Tedesco, Daniel Osorio, Emily-Rose Creighton, Dr. Lourdes Couoh, Dr. Kezhuan Gu, Dr. Hanshuo Liu, Dr. Steffi Woo, Dr. Edson Bellido Sosa and many other friends whose names haven't been listed here.

Last but not least, I would like to express my love and gratitude to my parents, Dr. Mingming Wang and other family members. I appreciate your unconditional love, care and support!

Declaration of Academic Achievements

The major results of my PhD research work were published or written into manuscripts for publishing in peer-reviewed journals, which are listed in the following:

- Xiaoyue Wang, Furqan A. Shah, Anders Palmquist, Kathryn Grandfield. 3D Characterization of Human Nano-osseointegration by On-Axis Electron Tomography without the Missing Wedge. *ACS Biomaterials Science and Engineering*. 2017, 3, 49.
- Xiaoyue Wang, Brian Langelier, Furqan A. Shah, Andreas Korinek, Matthieu Bugnet, Adam P. Hitchcock, Anders Palmquist and Kathryn Grandfield. Biomineralization at Titanium Revealed by Correlative 4D Tomographic and Spectroscopic Methods. (*submitted)*
- Xiaoyue Wang[※], Jie Yang[※], Carmen Andrei, Leyla Soleymani, and Kathryn Grandfield. Biomineralization of Calcium Phosphate Revealed by *in situ* Liquid-Phase Electron Microscopy. [※]*These authors contributed equally to this work.*

In addition to the work presented in this thesis, I am also co-author of two published papers relevant to my PhD project, which are attached in the Appendix.

- Furqan A. Shah, Xiaoyue Wang, Kathryn Grandfield and Anders Palmquist. High-resolution Visualisation of the Osteocyte Lacuno-canalicular Network Juxtaposed to the Surface of Nanotextured Titanium Implants in Human. *ACS Biomaterials Science and Engineering*. 2015, 1, 305.
- Brian Langelier, Xiaoyue Wang, Kathryn Grandfield. Human Bone Structure from Atom Probe Tomography. *Scientific Reports*, 2017, 7, 39958.

Table of Contents

List of Abbreviations

2D	two-dimensional
3D	three-dimensional
4D	four-dimensional
ACC	amorphous calcium carbonate
ACP	amorphous calcium phosphate
APT	atom probe tomography
BSE	backscattered electron
CaP	calcium phosphate
cp-Ti	commercially pure titanium
cryo-TEM	cryogenic TEM
DC	direct current
EELS	electron energy loss spectroscopy
ELNES	electron energy-loss near-edge structure
EDS	energy dispersive X-ray spectroscopy
EFTEM	energy filtered transmission electron microscopy
FIB	focused ion beam
HAADF	high-angle annular dark-field
IVAS™	Integrated Visualization and Analysis Software
LM	light microscopy
LP-TEM	liquid phase transmission electron microscopy
micro-CT	micro-computed tomography
NMR	multinuclear magnetic resonance
NEXAFS	near edge X-ray absorption fine structure
NCPs	non-collagenous proteins
ROI	region-of-interest
SEM	scanning electron microscopy

STEM	scanning transmission electron microscopy
STXM	scanning transmission X-ray microscope
SE	secondary electron
SIRT	simultaneous iterative reconstruction technique
SR-μCT	synchrotron radiation-based computed microtomography
TEM	transmission electron microscopy
WBP	weighted back-projection

Chapter 1 Introduction

1.1 Research Motivation

Bone is a vital biomineralized tissue in the human body exerting important functions of ion storage, locomotion, support and protection.[1] In order to functionally repair bone tissue, various biomaterials have been developed and applied as bone implants.[2] Bone implants have been widely used worldwide, and in US alone 1 ~ 2 million dental implants and over 600,000 hip and knee replacement implants are placed annually.[3] The success of these reconstructive and regenerative orthopaedic and dental surgeries is based on the long-lasting bonding with biomechanical functions between the living bone and implants, which is the phenomenon termed osseointegration.[4] Many factors have been demonstrated to affect osseointegration, such as chemical composition of implant surface, biochemical molecules attached to the implant surface, and surface topography.[5] Therefore, a complete characterization and understanding of the interface between human bone and implant offers valuable insight into the mechanisms of osseointegration in order to optimize implant surface modification.[5]

Due to the hierarchical structures of bone, correlative multiple length scale characterization techniques are needed. Research has developed dramatically from histological observation with the aid of the light microscope, to micron-scale resolved SEM, and further to nano-scale investigation using transmission electron microscopy (TEM).[6–8] Despite the advancement in spatial resolution, two-dimensional (2D) characterization techniques constrained to 2D projections do not properly present the inhomogeneous nature of bone and complex topography of implant surfaces interface. Thus, it is necessary for osseointegration characterization to progress from 2D to three-dimensional (3D) analyses. X-ray micro-computed tomography (micro-CT),[9–13] serial sectioning with focused ion beam (FIB) dual-beam microscope,[14–22] and transmission electron tomography[23] are well-developed tomographic characterization

techniques with spatial resolution from the microscale to nanoscale. Among them, of great interest is electron tomography using scanning transmission electron microscopy (STEM) in high-angle annular dark-field (HAADF) imaging mode, since it provides not only superior nanoscaled resolution, but also compositional contrast.[24–27] However, due to the thickness and shadowing effects of conventional TEM lamellae at high tilt angles[28] and the limited tilt-range of TEM holders, an artifact called the "missing wedge" is observed[25], which leads to elongation in the direction of the missing wedge so as to limit the resolution in the final reconstruction.[23] On-axis electron tomography is a promising method to solve the missing wedge problem and acquire high-fidelity reconstructions of osseointegration for a more quantitative analysis.[29–32]

Even though, based on electron tomography, the original definition of osseointegration has developed into nano-osseointegration,[26] the mechanism of osseointegration is still under debate. One of the key issues is the distribution of calcium- and carbon-based materials, or mineralized and organic components, at the bone-implant interface and their origins. Thus, it is also vital to understand the nanoscaled chemical structures at human bone implant interfaces in 3D. Electron tomography should step further to four dimension (4D) by adding spectroscopic data as the fourth dimension.[25] Based on the needle-shaped sample geometry, on-axis electron tomography provides possibilities to correlate electron tomography to spectral information (e.g. electron energy loss spectroscopy (EELS)) since specimen thickness remains constant at high tilt angles.

Besides spectroscopic electron tomography, atom probe tomography (APT) is another 4D tomography technique that could be applied to probe the elemental distribution at bone-implant interfaces. APT is based on field evaporation and the implementation of an ultraviolet laser has expanded its application into biological samples, such as chiton teeth or human bone.[33,34] Physico-mechanical interdigitation and bio-chemical bonding have

been reported as the potential contact mode at bone-implant interfaces.[35] Due to its atomic spatial resolution, APT is efficient to determine whether there is atomic continuity at the bone-implant interface, which supports that the interface bonding mode is not merely limited to mechanical interdigitation. In addition, owing to its superior chemical sensitivity (down to 1 ppm) across the entire periodic table,[36] APT is able to identify the trace elements (e.g. Na) and their distribution in bone, which could help further understand the bonding mechanism of bone and implant.

The two advantages of APT mentioned above are a nice complement to spectroscopic tomography. Meanwhile, it is also necessary to correlate APT reconstructions with other techniques, such as STEM images or electron tomography[37], considering the problems related to uneven evaporation during APT data acquisition due to the inhomogeneous nature of biological specimens[38]. In this way, the correlated APT and spectroscopic tomography could support and complement each other to strengthen the concept of 4D tomography. However, 4D tomography only provides the information on the spatial distribution of elements but not their chemical state. To overcome these issues, spectrometric studies of near edge X-ray absorption fine structure (NEXAFS) on scanning transmission X-ray microscope (STXM) and electron energy-loss near-edge structure (ELNES) using STEM are able to correlate to the 4D tomography to investigate chemical states of individual elements by identifying the information such as valence and local coordination, based on the fine structural features at the absorption edge.[39]

The main mineral constituent of bone is hydroxyapatite, whose biomineralization process is the basis of bone remodeling, as well as osseointegration. Since hydroxyapatite is a phase of calcium phosphate (CaP), understanding the mechanism of CaP biomineralization is critical for research on both pathological bone diseases and osseointegration mechanisms.[40] Although the studies based on cryogenic TEM

(cryo-TEM) have proposed that CaP nucleates and grows *via* particle attachment mechanisms, direct experimental support by real-time observation is still needed to demonstrate this hypothesis.[40,41] Liquid phase (LP)-TEM, with the ability to record biomineralization processes *in situ* with nanoscaled spatial resolution and sufficient temporal resolution, is a promising technique to image dynamic nucleation and growth process of CaP and unveil its mechanism of biomineralization. Furthermore, the *in-situ* TEM research on CaP biomineralization could lay a foundation for applying LP-TEM techniques to explore the unsolved issues of bone biomineralization, such as the effects of extracellular matrix on mineralization[42] or the function of non-collagenous proteins during the mineralization process.[43]

1.2 Research Objectives and Hypothesis

The overall aim of this thesis is to enhance the knowledge and understanding of osseointegration mechanisms by applying suitable multi-dimensional microscopy techniques, with the eventual aim that these techniques and conclusions could then be used downstream to improve the surface modification of next generation implant materials. The detailed objectives are summarized as following:

(1) To understand nano-osseointegration at interfaces by using on-axis electron tomography to circumvent missing wedge artifacts.

(2) To develop correlative nano- and sub-nanoscaled 4D tomographies, with chemical information as the fourth dimension, in order to probe the chemical characteristics of the biointerphases between human bone and commercial titanium dental implant.

   (a) To visualize nanoscaled chemical structures at interface by applying EELS tomography.

   (b) To experimentally demonstrate the atomic continuity of osseointegration at interface by using APT.

   (c) To optimize APT experiment parameters for characterizing natural biominerals

and biointerface samples.

(d) To establish the correlative 4D tomography workflow based on the same needle sample, which is transferable to other applications in materials science or biological systems.

(3) To study CaP biomineralization mechanism *via in-situ* liquid TEM.

(a) To image dynamic nucleation and growth process of CaP by using *in-situ* LP-TEM.

(b) To lay a foundation for applying LP-TEM technique to explore CaP biomineralization in more complex organic–inorganic physiological solutions.

The first two sections of this thesis are founded on the hypothesis that hierarchically-structured bone bonds to the engineered implant surface on multiple length scales, from the macroscale down to atomic scale, containing a transition layer with different morphologies and chemical structures from mature bone directly at the bone-implant interface. During this osseointegration process, CaP biomineralization may occur at the implant surface. Therefore, the second part of this thesis focuses on the study of CaP initial nucleation and growth as a first step to lay down a foundation for future research on CaP biomineralization at implant surfaces. In this section, real-time observations of this dynamic process were conducted with the hypothesis is that CaP crystalizes by particle attachment.

1.3 Thesis Outline

Chapter 1: Introduction. This chapter provides a general introduction to this research, which states study motivations, clarifies detailed research objectives and summarizes the thesis outline.

Chapter 2: Literature Review. This chapter reviews relevant literature and fundamental principles related to this thesis. It includes: fundamental principles of bone

structure and osseointegration, and an introduction to state-of-the-art characterization techniques as applied to osseointegration and biomineralization research, including 3D and 4D tomographies (EELS tomography, APT), and *in-situ* liquid TEM.

Chapter 3: "3D Characterization of Human Nano-osseointegration by On-Axis Electron Tomography without the Missing Wedge". This chapter presents the first application of on-axis ET for investigation of human bone and laser-modified titanium implant interfaces without the missing wedge. This work demonstrates a near artifact-free 3D visualization of the nano-topographies of the implant surface oxide layer and bone growth into these features. This approach serves as direct evidence of nano-osseointegration and as a potential platform to evaluate differently structured implant surfaces. This work has been published in the Journal of *ACS Biomaterials Science & Engineering*.[44]

Chapter 4: "Biomineralization at Titanium Revealed by Correlative 4D Tomographic and Spectroscopic Methods". Based on the needle-shaped sample geometry, this chapter reports the first correlative 4D chemical tomography study of a bone-implant interface, including on-axis electron tomography, EELS tomography, and APT performed on the same sample. The combination of these methods reveals both nano and atomic scale information needed to understand biomineralization at the bone-implant interface. The workflow of these correlative 4D tomographic methods presented here are also applicable to other biological systems or materials science applications. This manuscript has been submitted for publication.

Chapter 5: "Biomineralization of Calcium Phosphate Revealed by in situ Liquid-phase Electron Microscopy". This chapter presents the first real-time imaging of CaP nucleation and growth with *in situ* LP-TEM, which is a direct evidence to demonstrate that CaP mineralizes by a particle attachment mechanism. This work lays the foundation for further real-time investigation of CaP biomineralization in more complex organic–inorganic physiological solutions. This work has been written in

manuscript for publication.

Chapter 6: Concluding Remarks. This chapter summarizes key findings, defines major contributions and explores future work for this research.

Chapter 2 Literature Review

2.1 Bone

Bone is a mineralized tissue that serves as the mechanical support and protection for vital organs, and also as the reservoir of calcium (Ca) and phosphorous (P) ions for vertebrates. Its structure, composition, and formation have been important research topics in the fields of physiology and medicine.[45] In addition, as a hierarchical self-assembled composite material with distinct mechanical properties, bone also attracts lots of attention in materials research.[46] The studies presented in this thesis focus on the materials perspective.

2.1.1 Bone Composition

Bone consists of 60% (weight percent) of mineral phase, 30% (weight percent) of organic components and 10% (weight percent) water.[47] The mineral phase of mature bone is primarily carbonated hydroxyapatite ($Ca_{10}(PO_4,CO_3)_6(OH)_2$) with the carbonate ions substituting either phosphates or hydroxyl ions in a hexagonal crystal structure. These mineral crystals have an elongated plate shape with dimensions of 2-6 nm thick, 25-50 nm wide and 50-100 nm long.[48] Recent multinuclear magnetic resonance (NMR) studies proposed that this plate-like morphology of apatite nanocrystals in bone was stabilized by strongly bound citrate on the surface of crystallites.[49] The organic components of bone contain mainly Type I collagen fibrils and non-collagenous proteins (NCPs). The triple-helical collagen molecules that comprise collagen fibrils are also on the nanoscale with dimensions of 1.5 nm in diameter and 300 nm in length.[48] Collagen molecules assemble into arrays to form collagen fibrils with 40 nm gap zones and 27 nm overlap zones, which are observed as characteristic collagen banding of 67 nm in transmission electron microscope (TEM) images.[43] The collagen fibrils and the NCPs form what is referred to as the extracellular matrix.[50] Also, the NCPs are functional proteins that mediate bone mineralization processes by signaling apatite nucleation.[51] In

addition to the main elements that comprise the mineral and organic components of bone (i.e. C, H, O, N, P, Ca), trace elements of Na, Mg, Sr and Zn are also detected in bone.[52,53] Mg is reported to incorporate into the hydroxyapatite crystal structure, which functions as a growth factor to promote bone formation in early stages of osteogenesis.[54] Even though the function of Na in bone is still unclear, its co-localization with organic parts of bone has been observed by atom probe tomography study (APT) in previous studies.[34] Zn is present in bone calcified matrix playing an essential role in bone metabolism.[53] Chemically similar to Ca, Sr is suggested to influence bone turnover processes.[53]

2.1.2 Bone Structure

2.1.2.1 Hierarchical Structure

Bone has a distinct hierarchical structure organized from the millimeter to nanometer scale. Generally, seven levels are classified in bone architecture from the bottom up (Figure 2-1).[55] The basic building units of bone structure are apatite crystals and tropocollagen molecules, which are both on the nanoscale. The collagen fibrils generate from the staggered arrays of tropocollagen molecules and then become mineralized as bone matures.[56] These mineralized fibrils align along their long axis to form bundles and arrays which are collagen fibres. Organized in various patterns such as parallel, tilted woven or circularly rotated arrangements, these collagen fibres then generate the higher hierarchy of lamellae structure on the micro-scale. The concentric lamellae form the characteristic cylindrical motif called osteons with vascular channels in the middle and osteocytes in lacunar-canalicular networks. At the macrostructure level, the whole bone is made up of compact bone which is the dense outer shell and the interior sponge-like trabecular bone.

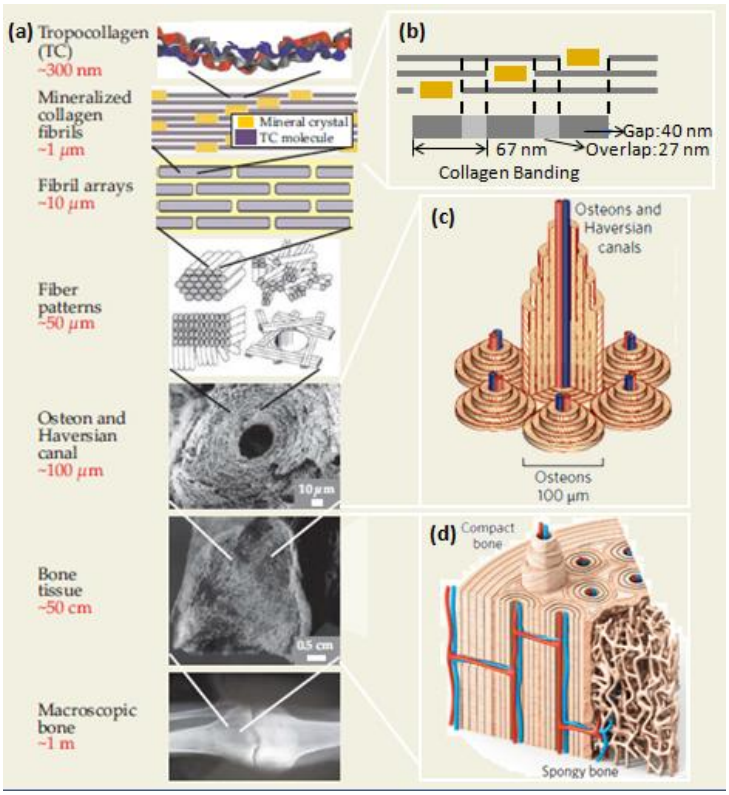

Figure 2-1. (a) Hierarchical levels of bone structure from nano- to macro-scale. (b) the schematic of collagen banding, (c) the structure of osteons, (d) compact bone and trabecular bone structures. (a) was reproduced from reference[56] with permission of the American Institute of Physics. This image was adapted from the original source, reference[55]. And (c,d) was reproduced from reference[46] with permissions.

2.1.2.2 Ultrastructure Model

The ultrastructure of bone is related to the nanoscaled spatial organization of mineral crystals and collagen fibrils. The conventional ultrastructural model insists on the presence of intrafibrillar mineralization, that is apatite crystals mineralized within the gap zones of collagen fibrils with their alignment parallel to the long axes of fibrils (Figure 2-2(a)).[57] However, the mineral phase is known to take up around 50% by volume of bone, which is much larger than the space available in the gap zones of collagen fibrils.[58] Recent studies therefore also suggest the existence of interfibrillar minerals between adjacent collagen fibrils and extrafibrillar minerals external to collagen fibrils.[59] Based on TEM and electron tomography observations by Schwarcz *et al.*, a new model of bone

ultrastructure was proposed.[60,61] As shown in Figure 2-2 (b), in this new model stacks of mineral lamellae with the approximate dimensions of 60 nm wide, 5 nm thick and hundreds of nm long are packed around the collagen fibrils in the diameter of 50 ± 20 nm. The fibrils are wrapped by multiple mineral lamellae and with the distance between adjacent mineral lamellae less than 1 nm. [58]

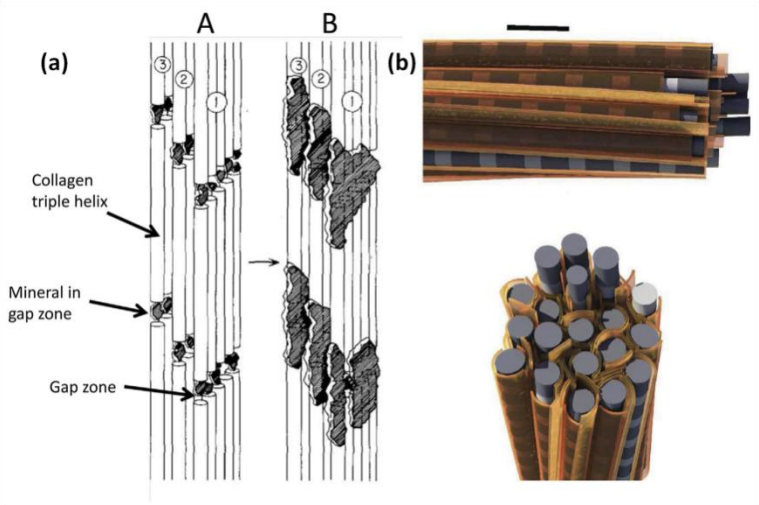

Figure 2-2. (a) Schematic diagram of intrafibrillar ultrastructure (A), interfibrillar ultrastructure formed by minerals extending into adjacent overlap zones (B);[57] (b) schematics of the extrafibrillar ultrastructure, orange sheets represent mineral lamellae and gray cylinders represent collagen fibrils. (a) was reproduced from references[57] and (b) from reference[58] with permissions.

2.1.3 Bone Remodeling

Bone is not only a composite material with hierarchical structure, but also a living tissue with cells responsible for its metabolism and maintenance. Living bone is remodeling throughout life to heal microfractures, adapt to mechanical changes, and maintain homeostasis of calcium and phosphorous. Bone remodeling is a complex process of new bone replacing older bone as the result of coordinated activity of bone cells. [47] (Figure 2-3)

2.1.3.1 Osteoblasts and Bone Formation

Osteoblasts, originating from mesenchymal stem cells, are clusters of cuboidal cells with the function of bone matrix synthesis. Generally, two steps are included in new bone formation by osteoblasts: (1) secreting osteoid, which is the extracellular organic matrix made up of Type I collagen, non-collagenous proteins and proteoglycans, and (2) the subsequent mineralization of osteoid. Nearing the end of bone formation, some mature osteoblasts are trapped in the bone matrix and differentiate into osteocytes which reside inside a space referred to as the lacunae where they act as mechanosensors, others become flat lining cells. [1]

2.1.3.2 Osteoclasts and Bone Resorption

Osteoclasts, with the characteristic feature of a ruffled border, are giant multinucleated cells responsible for bone resorption. After attachment to the bone matrix, osteoclasts form a sealed compartment between the cell and the bone surface for surrounding acidification. The bone matrix and mineral crystals encapsulated within this sealing zone are resorbed by osteoclasts by acidification and proteolysis. This resorption surface of old bone has a highly complex morphological structure in 3D at the sub-micron length scale so as to help with the interdigitation and interlock between old and new bone.[62]

2.1.3.3 Mechanism of Bone Remodeling

Considering morphological differences, bone remodeling is classified as the Haversian remodeling inside cortical bone and the endosteal remodeling on the trabecular bone surface. But, both types of remodeling follow the same coordinated cellular events with the sequence of activation, resorption, and formation. In the initiation stage, as the result of a certain signal, a group of stem cells are recruited to a definite area of the bone surface and then differentiate into osteoclasts for bone resorption. After old bone matrix is resorbed, osteoclasts are detached from the resorption surface and a layer of

mononuclear cells cover it to generate a cement line there. The cement line, an electron denser layer by electron microscopy study, acts as the interface between old and new bone. This is the so-called reversal (or transition) phase. Then, pre-osteoblasts are activated and differentiate into mature osteoblasts for new bone formation. An initial extracellular matrix (osteoid) is formed and then mineralized into new bone. The initially deposited bone is unorganized and referred to as woven bone[63], which continues to remodel over time into organized lamellar bone[64]. The evidence of bone remodeling can be found in bone morphological observations The newly formed osteons cut through the old ones in compact bone.[1,65] During each remodeling cycle, bone resorption takes around 2 to 4 weeks while bone formation needs almost 4 to 6 months to accomplish.[66] An understanding of bone formation and remodeling is essential to then apply this concept to bone growth at a synthetic implant interface.

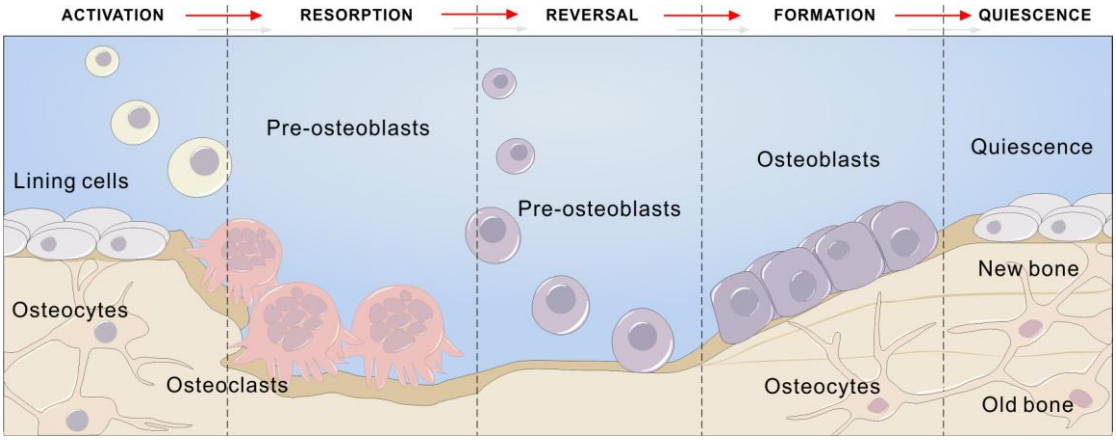

Figure 2-3. Schematics of coordinated cellular events with the sequence of activation, resorption, reversal, formation and quiescence during bone remodeling. The figure adapted from reference[67]

2.2 Bone-Implant Interface

2.2.1 Bone Implants

Every year millions of dental, hip and knee replacement implants and even customized 3D printed bone implants are placed in human body. In Canada, the number of hip (51,272 cases) and knee (61,421 cases) replacement surgeries has increased around 20%

in 2014-2015 compared to five years prior.[68] The majority of commercially available bone implants are made of alloys such as cobalt chromium (Co-Cr) alloys, stainless steel, commercially pure titanium (cp-Ti) and titanium alloys (specifically, Ti_6Al_4V).[2] Among them, cp-Ti has been used extensively in dental and orthopaedic reconstructive surgeries as the result of the excellent corrosion resistance and biocompatibility of the oxide layer on its surface. [69] All the samples in this thesis are cp-Ti dental implants with an oxide layer produced *via* modification by laser ablation.[70,71]

cp-Ti is classified into 4 grades depending on the weight percentage of minute contaminants. Cp-Ti consists of α-phase (hexagonal close-packed structure). When heating up to 883 ℃ and above, cp-Ti will transform from α-phase into β-phase (body-centered cubic structure) and it can be stabilized by adding alloy elements such as Al and V (Ti6Al4V). The mechanical properties of these metallic implant materials are based on the thermomechanical treatments including annealing and aging which changes their microstructures.[69] A thin and amorphous oxide film forms spontaneously on the surface of titanium metal.[72] This surface oxide layer is biocompatible and bioinert. Its physicochemical characteristics and topographies are critical for biomineralization and osseointegration.[73] Rutile is the naturally stable crystalline phase of TiO_2. Due to the lower isoelectric point (5.9) compared with body fluids pH (7.4), the rutile surface tend to deprotonate and consequently attract Ca^{2+} ions, which is beneficial to biomineralization precedence.[74] Compared with the conventional implant surface modification methods such as acid-etching, grit-blasting and anodic oxidation, laser surface modification has multiple merits including precision machining, low contamination and ability to form hierarchical topography.[73] It has been reported that the laser-induced micro- and nano-scaled oxide features on the surface of cp-Ti implant decreased the attachment of inflammatory cells [75] and contributed to bone-implant interlocking.[71]

2.2.2 Osseointegration

Despite the vast developments towards improved bone implant devices, there are still appreciable implant failures demanding revision surgeries. Most of these failures are caused by the lack of a long-lasting bonding between the bone and implant devices.[3] This bonding was initially defined as osseointegration by Brånemark *et al.* in the 1950s [4,76] and has motivated decades of research since then. With the development of characterization techniques, osseointegration at nanometer length scales has been observed by using TEM and electron tomography. Therefore, the original definition of osseointegration has developed from histological perspectives into nano-osseointegration.[26] This term is used to describe not only the morphological phenomenon of bone growing into the nanoscale topography of implant surfaces so as to interdigitate and mechanically interlock with implants, but also the chemical characteristics of the biointerface at the nanoscale.

Osseointegration is believed to be the result of both distant osteogenesis, where bone first approximates the implant surface, and contact osteogenesis, when new bone first forms on the implant surface.[77] Both types of osteogenic processes follow the same cellular processes as bone remodeling. However, what constitutes the direct contact layer, the so-called 'true' interface, [78] is still debated. Many conflicting theories of osseointegration mechanisms have been proposed.

Davies *et al.* proposed the theory of osseointegration where a non-collagenous hypermineralized layer similar to a cement line is generated at the bone-implant interface.[62,79] This sub-micron layer is the conserved extracellular matrix interdigitating new bone with old bone or implant surfaces.[78] In this theory, a highly complex microscale topography is necessary for either implants or old bone surfaces to initiate bone bonding.[79] In contrast, a "proteoglycan-rich" layer was proposed to directly bond

bone with implant surfaces by other researchers.[80] Proteoglycans exist in the extracellular matrix with the physiological function of coordinating cellular activities and stabilizing growth factors in the bone mineralization process.[80] At the ultrastructural level, Albrektsson *et al*. observed a three-zone-structure at the interface between bone and pure titanium layer coated on polycarbonate rods.[81] The zone intimately contacted with the metal surface consisted of a 20-40 nm proteoglycan-rich ground substance, which was followed by the second zone with randomly distributed collagen fibrils and organized collagen fibers in the third zone.[81] Steflik *et al.* confirmed and further developed this bone-proteoglycan implant interface model.[82] They observed the existence of a 20-50 nm electron-dense layer at the interfaces of both titanium and ceramic (alumina oxide) implants by TEM.[82] This layer directly bonding bone and implant surface was determined to be glycosaminoglycan in nature. However, Mckee *et al*. showed the existence of osteopontin-containing cement lines at titanium and hydroxyapatite implant interfaces in rat model experiments. They have theorized that osteopontin in cement lines acts as an interfacial adhesion promoter in both bone-bone and bone-implant bonding.[83]

Based on these above observations, the mechanism of osseointegration is still inconclusive. One of the key remaining issues is the distribution of calcium-based (i.e. inorganic) and carbon-based (i.e. organic) components, at the bone-implant interface and their origins. In Chapter 4, the chemical structure of human bone-implant interface was investigated at both nano- and sub-nanoscale in 3D. We observed morphological and chemical changes at the interfaces from mature bone to the oxide layer on the surface of commercial titanium dental implant. An intervening transition zone was defined with disorganized apatite-rich substrate. Both Ca and C were proven distributing intimately at implant surface. The phase of Ca was identified as amorphous calcium phosphate by spectroscopy characterizations, while the phase of C is not fully understood and requires further research.

Many factors have been demonstrated to affect osseointegration, such as implant chemical compositions, functionalization with biochemical molecules, and topography of implant surfaces.[5] The hierarchical implant surface topography with nano-, micro-, and macroscaled roughness was reported both in *in vitro* and *in vivo* studies to improve osseointegration *via* distinct biological mechanisms related to each length scale.[79] On the nanoscale, it was demonstrated that the cement line matrix proteins can be deposited inside the interstices of implant surfaces and undercut to form bonding.[78] On the microscale, the cement line occupies the implant surface features for bone implant interlocking. On the macroscale, the collagen fibres of new bone wrap around implant surface features and are then mineralized to form a functional interface.[79]

After the initial bone-implant osteogenesis events described above, osteogenic cells lay down the osteoid layer, which later mineralizes to result in the initial woven bone surrounding implant devices.[79] With further bone remodeling, this unorganized initial bone is overturned and replaced by mature bone with hierarchical structures.[77] Grandfield *et al.* have visualized the arrangement of collagen near the bone-implant interface in three-dimensions (3D), and noted that the collagen is oriented parallel to the interface. [24,25,27] Shah *et al.* confirmed a similar parallel alignment of collagen at bone-implant interface and natural interface (bone-osteocyte interface).[84] Further work to investigate the 3D nature of the bone-implant interface will be explored in this thesis.

2.3 Three-Dimensional (3D) Characterization of Bone-Implant Interface

With the development of characterization techniques, we further understand the mechanisms behind the topological and chemical factors influencing osseointegration.[5,78] On one hand, these techniques are used to interpret spatial and chemical structures of bone-implant interfaces to explain how living bone bonds to synthetic biomaterials. On the other hand, these developed techniques are also useful tools to characterize and

evaluate whether certain implant surfaces contribute to faster and better osseointegration in *in vitro* and *in vivo* experiments, so as to provide valuable suggestions for implant designs and surface modifications.

From light microscopy (LM), scanning electron microscopy (SEM), to TEM, multiple length scale imaging techniques have aided researchers to investigate bone-implant interfaces from microscaled observations, such as cell behavior at the interface [84], to nanoscaled descriptions of complex events, such as mineralization[62,79]. However, these predominantly two-dimensional (2D) imaging techniques constrained to 2D projections do not properly present the inhomogeneous nature of bone and complex topography of the bone-implant interface. Thus, tomography for 3D structure analysis has been identified as strategic priority. Figure 2-4 shows different tomographic characterization techniques and their associated resolution and analysis volumes.[17] This thesis will highlight four distinct tomography approaches: micro-computed X-ray, focused ion beam, electron and atom probe tomography.

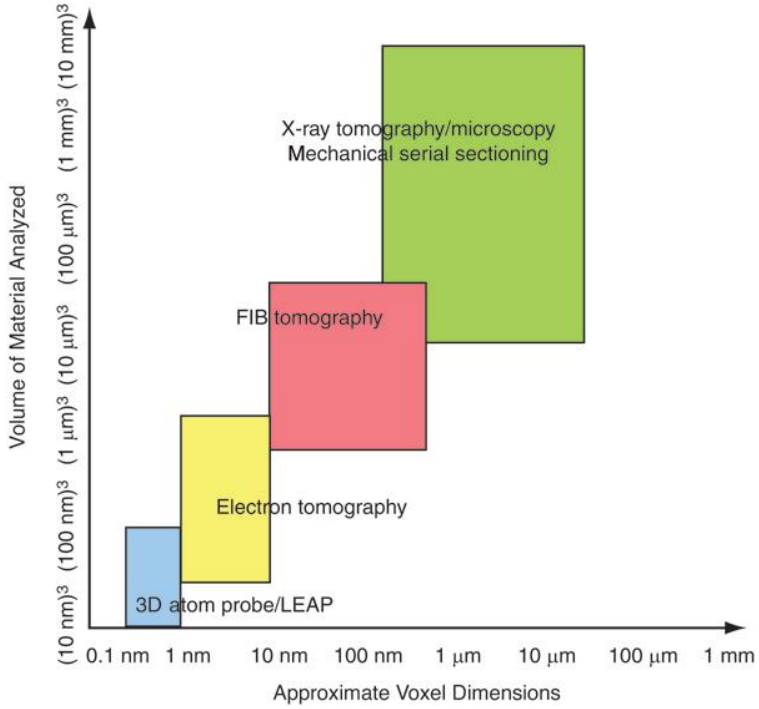

Figure 2-4. Tomographic characterization methods mapped with respective spatial resolution and analysis volume. The figure was reproduced from reference[17] with permissions.

2.3.1 X-ray Micro-Computed Tomography

Micro-computed tomography (Micro-CT) is a nondestructive 3D technique with spatial resolution from millimeter to micrometer.[13] It is not only widely used in clinical applications, but also in materials research such as to image alloys after deformation or mechanical testing.[85] In micro-CT systems, samples are rotated 360 °, and X-rays are used to acquire 2D projections for later 3D reconstruction based on the physical principle of the attenuation of X-rays through different materials.

In osseointegration research, micro-CT reveals the trabecular structure and microscale nature of bone ingrowth surrounding implanted devices. Thorfve *et al.* used micro-CT visualization to compare *in vivo* implant samples from 7 days and 28 days inserted in rat tibia, to highlight the organization and maturation of bone over time. In 28 day samples, the trabecular bone structure had grown toward the implant. But, the 7 day samples only showed woven bone formation and bone fragments from surgery around the implant.[12] In addition, complex topography of modified implant surfaces is also revealed by this technique.[71] Micro-CT has several advantages; it is nondestructive and also offers a large view of a sample, but it is limited in spatial resolution, meaning this technique cannot visualize bone ultrastructure in 3D. If synchrotron radiation is used as a light source, micro-CT can achieve finer resolution down to 100 nm due to the high-intensity parallel beam.[11] Arvidsson *et al.* used synchrotron radiation-based computed microtomography (SR-μCT) to measure bone implant contact and bone area in *ex vivo* retrieved implants. Compared with 2D quantitative histomorphometry using light microscopy, SR-μCT is nondestructive and also provides information of the entire 3D sample.[10] Another technique used to image bone ultrasctructure in 3D is, synchrotron based scanning transmission soft X-ray microscope (STXM), which not only supplies higher spatial resolution but also spectroscopic information of near-edge X-ray absorption fine structure spectroscopy.[86] Buckley *et al.* used STXM to map the distribution of inorganic

(Ca) and organic (C) phase in rat bone.[87] With the ability to visualize the 3D structure of large volume of samples nondestructively, micro-CT has been demonstrated as one of the most efficient 3D characterization techniques for bone-implant interface research.

2.3.2 Focused Ion Beam Tomography

Focused ion beam (FIB) tomography, also known as FIB-serial sectioning, is a technique in which an ion beam sequentially removes thin layers of material in a few nanometer thickness from a sample's cross section, while a scanning electron beam images each layer. After images are acquired, these images are aligned, reconstructed, and visualized in a 3D volume. Secondary electron (SE) and backscattered electron (BSE) images can be acquired simultaneously to improve phase segmentation and analysis.[18] FIB tomography can encompass sample volumes as large as 1000 μm^3 combined with voxel resolution in tens of nanometers, which covers a length-scale gap among modern tomography techniques.[17] This 3D technique was initially used in studies of fuel cells and battery electrode materials, and materials of high porosity[18], but it is now also widely used in biomaterials and bone research.[16] Based on the FIB tomography of demineralized rat bone, Reznikov *et al.* discovered that lamellar bone is composed of two unique type structures. One predominant structure is the well-known ordered arrays of collagen fibrils and the other is poorly oriented individual type Ⅰ collagen fibrils with abundant non-collagenous organic materials.[21,88] Also, canaliculi and their cell processes are notably confined within this disordered structure.[21,2288] Schneider *et al.* was the first to accomplished a quantitative 3D assessment of lacuna-canalicular network of mouse bone achieving a resolution of 30 nm by using FIB tomography.[19] Later, Giannuzzi *et al.* applied this technique into bone-implant interface research on a patient retrieved commercial implant TiUnite.[16] Bone was observed growing into the microscale porous structure of the implant coating. This work has demonstrated the usefulness of FIB tomography to characterize bone-implant interfaces, but the resolution is limited as

images were of the interface on the microscale; leading to the loss of interesting information such as collagen fibril orientation and mineral crystal distribution near the human bone-implant interfaces.[16] Energy dispersive X-ray spectroscopy (EDS) can also be correlated with FIB tomography to help phase segmentation and chemical structures visualization in 3D.[14,15] After appropriate sample preparation such as demineralization and staining, FIB tomography is a promising 3D characterization technique to visualize nanoscale structure of bone-implant interface with an intermediate sample volume.

2.3.3 Electron Tomography

2.3.3.1 Principles

Electron tomography collects 2D projections obtained by TEM over a small angular increment tilt series to reconstruct 3D objects. The projection-slice theorem is a principle of tomography, which confirms the equivalence of the Fourier transform of 2D projections of a 3D object with the central sections of the object's 3D Fourier transform (Figure 2-5). Thus, the 3D object in its entirety can be retrieved by the inverse Fourier transform of the 2D projections of this object. [89]

Electron tomography provides superior spatial resolution (voxel) in the nanoscale, which is not only related to the spatial resolution (pixel) in the 2D projections acquired in TEM, but is also limited by the number of projections and tilt range according to the Crowther criterion[90]. The resolution of the dimension X parallel to the tilt axis only depends on the microscope or sample, whereas the resolution of the dimension Y perpendicular to the tilt axis follows the equation below:

$$d_y = \pi \cdot \frac{D}{N} \qquad (1)$$

Where D is the diameter of the object and N is the number of acquired projections. In the third dimension, the Z direction, the resolution is reduced by the limited tilt angle range:

$$d_z = d_y \cdot e_{yz} \quad (2) \qquad e_{yz} = \sqrt{\frac{\alpha + \sin\alpha \cdot \cos\alpha}{\alpha - \sin\alpha \cdot \cos\alpha}} \quad (3)$$

Where e_{yz} is the elongation factor and α is the maximum tilt angle. [91]

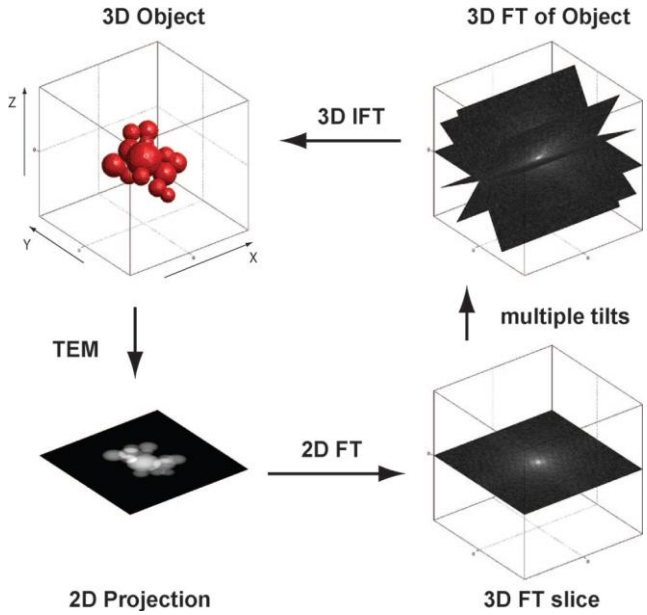

Figure 2-5. Schematic of the principle of electron tomography reconstruction. FT is short for Fourier transform and IFT is short for inverse Fourier transform. In single tilting axis, a series of 2D projections of the 3D object at different tilt angles are recorded. According to projection-slice theorem, the 3D FT of the object can be acquired by combining the FT of the series of 2D projections. Then the 3D object is reconstructed by an IFT. The figure was reproduced from reference[89] with permissions.

2.3.3.2 Imaging Modes

Both TEM and scanning TEM (STEM) have been employed as the imaging modes of electron tomography acquisition in material and biology studies.[91,92] Figure 2-6 shows the different electron beam paths of TEM and STEM. Samples are probed by a parallel electron beam in TEM; whereas, in STEM, a focused beam is used for raster scans across samples. STEM enables dynamic focus at high tilt angles, which optimizes image focus at each raster and compensates for the focus change of tilted samples. High-angle annular dark-field (HAADF) imaging mode in STEM is used for all electron tomography work

presented in this thesis, as, the implant portion of samples are titanium, which has diffraction contrast in TEM. STEM HAADF can eliminate diffraction contrast and Fresnel fringes, which do not satisfy the projection criterion and can cause serious artifacts in reconstruction. Furthermore, the HAADF detector collects elastically scattered electrons so that its signal intensity approximately proportional to the square of atomic number, which provides compositional contrast. [92]

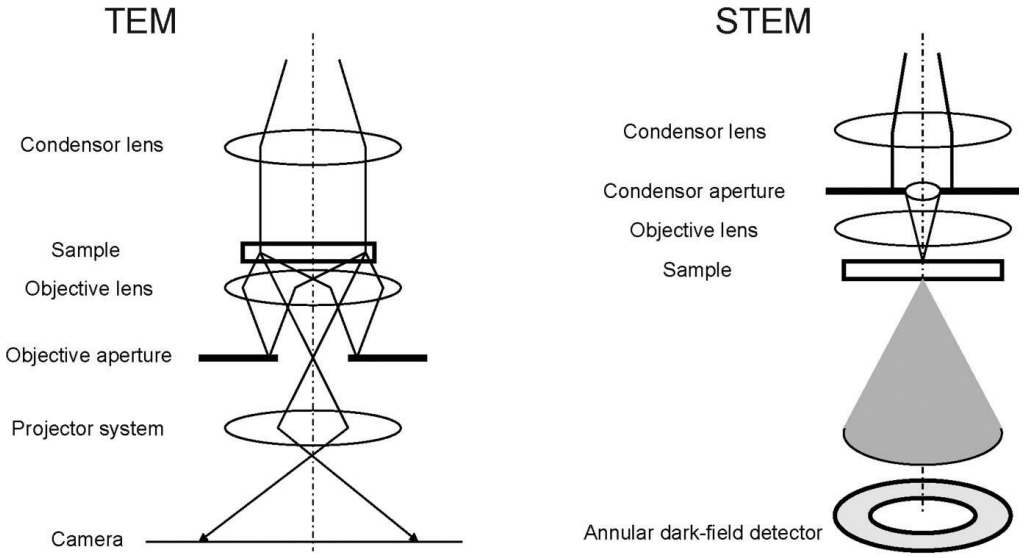

Figure 2-6. Schematic diagrams of the electron beam path in TEM and STEM imaging modes. The main difference between the operation modes is that a broad and parallel electron beam is used to illuminate the interested region of samples in TEM while a fine and highly focused electron beam is used to scan over the samples in STEM. The figure was reproduced from reference[89] with permissions.

2.3.3.3 Workflow

Usually, the workflow of electron tomography contains three steps: acquisition, reconstruction, and visualization (Figure 2-7). When acquiring 2D projections, the sample is typically tilted up to $\pm 70°$ with the step of $1°$ or $2°$ under electron beam. Many commercial software packages have been developed for automating the acquisition process of focusing, imaging, tilting, and tracking. After data collection, the stacks of images are aligned by either a cross correlation method or alignment of fiducial markers

(usually gold nanoparticles). Then, the images are reconstructed into a 3D volume using mathematical algorithms. The weighted back-projection (WBP) algorithm and simultaneous iterative reconstruction technique (SIRT) are the most commonly used reconstruction algorithms. [89] All of the reconstructions in this thesis work used SIRT, which is the re-projection of the reconstructed 3D model is compared to the initial projections to find the projection difference, and then reiterated until the difference is reduced. This has advantages over WBP, such as reducing noise and containing all frequency information. Based on inverse Radon transform, WBP corrects the local over/undersampling frequency information by applying weighting filters.[93] It works fast on large set of data but has edge-enhancement effects. Lastly, the reconstructed 3D objects are visualized by several approaches: volume rendering, isosurfaces or orthoslices through the use of visualization softwares, such as Avizo.

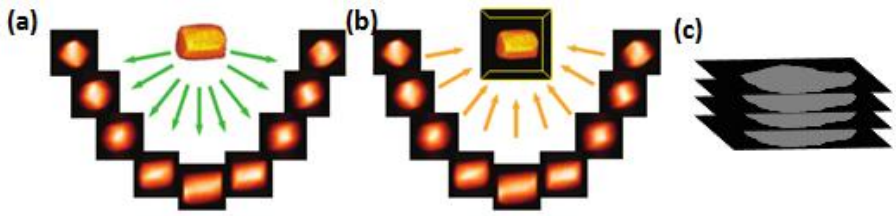

Figure 2-7. The three steps of electron tomography: acquisition (a), reconstruction (b) and visualization (c). (a,b) were reproduced from reference[23] with permissions.

2.3.3.4 Missing Wedge

For conventional lamellar TEM samples, there is a limitation of high tilt angle as the result of the microscopy geometry, and sample thickness and shadowing effects. Thus, a "missing wedge" is created and leads to artifacts and elongation in the direction of the missing wedge in the final reconstruction, as explained mathematically in Eqn. (1-3) and shown graphically in Figure 2-8 (a). One of the most reported solutions to this problem is dual-axis electron tomography, in which a second tilt-axis perpendicular to the original one is employed.[94–96] Although the so-called missing pyramid (Figure 2-8 (b)) left by this

method is considerably reduced compared to the original missing wedge in single-axis electron tomography, it is not the most optimum or practical solution considering that it fails to eliminate the missing wedge completely and needs additional experimental protocols including increased acquisition time. On-axis electron tomography (Figure 2-8 (c)), in which a needle shaped specimen is rotated and imaged through 180 °, is a promising method to solve the missing wedge problem. In Chapter 2, on-axis electron tomography was used to visualize a human bone-implant interface without missing wedge artifacts.

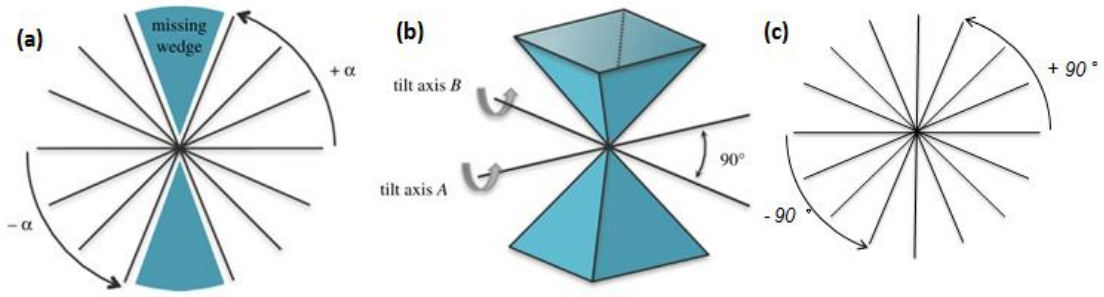

Figure 2-8. Schematics of missing wedge (a), missing pyramid (b) and on-axis tomography (c). (a,b) were reproduced from reference[25] with permissions.

2.4 Four-Dimensional (4D) Characterization of Bone-Implant Interface

The topography and chemical composition of the bone implant surface are both key factors which influence implant osseointegration. Electron tomography enables visualization of the nanoscale structures of the bone-implant interface in 3D, but is unable to provide chemical information at the interface. The nanoscale elemental distribution at this interface can indicate the type of bonding between bone and implant, or the presence of an organic or inorganic intermediate layer. Thus, electron tomography can be extended to 4D with the addition of chemical information as the fourth dimension.[25]

2.4.1 Spectroscopic Electron Tomography

Spectroscopic electron tomography has been reported as a 4D characterization technique to visualize nanoscale chemical structures in 3D in both material and biology studies.[97] Energy filtered TEM (EFTEM) images, STEM-EELS spectrum images and energy dispersive X-ray spectroscopy (EDS) elemental maps can be combined with electron tomography to generate spectroscopic tomography. This is feasible because these element-sensitive images and spectroscopic signals both comply with projection theorem and thus can be utilized in tomography reconstruction.[91]

EFTEM tomography was the first exploited 3D chemical imaging method and has been widely employed in biology and biomaterials research due to the enhanced elemental contrast, light element detection sensitivity and comparatively lower electron beam dose exposure compared to other spectroscopic tomography techniques.[98] EFTEM is based on EELS with imaging filter to only collect the inelastic scattered electron within a selected energy window.[99] The method of three-window elemental mapping is often used to extract the elemental maps of interest for reconstruction.[98] The intrinsic drawbacks of EFTEM tomography, such as offset in alignment of different elements, single element information collected at each acquisition and limited resolution, sometimes limit its applications.[100]

Due to the development of high-acquisition-rate detectors and high-brightness electron-sources, EELS and EDS tomographies have become experimentally practical with reasonable electron beam dose exposure over an acceptable acquisition time.[91] One of the key limitations of EDS tomography is the traditional single detector which results in X-rays being detected within a narrow range of specimen tilt angles. Advances in new designs of detector geometry such as the Super-X detector with four separate detectors placed around the optical axis in symmetry enables a wider range of tilt angles and a

shorter acquisition time.[101] This technique has been applied to visualize nanoscale structures of transistors[102] and nanoparticles.[101,103]

In addition to the challenges provided by detector geometry and detection rate, the increased thickness of specimens at high tilt angles has a negative impact on the quality of spectroscopic signals for tomography reconstruction, especially EELS, which is particular sensitive to specimen thickness.[91] The use of needle-like sample geometry can help to solve this problem by maintaining the same projection thickness at all tilt angles.[104] Through use of this sample geometry, EELS tomography has been applied to probe the nanoscale chemical structure of semiconductor devices[104] and catalyst nanoparticles[105–107] in 3D. In comparison to EFTEM, EELS tomography is based on spectrum images in which each pixel contains a full EELS spectrum in a wider energy range, and thus provides not only elemental distribution information in 3D but also chemical and electronic structure information.[104] At the data acquisition stage, the spectrum images of the interested region of sample over a series of tilt angles are collected together with dark field STEM images. Afterwards, this EELS data can be processed by two methods. One is to extract chemical distribution maps of certain relevant elements from each spectrum image and then reconstruct them into a 3D elemental volume following the same reconstruction approaches as traditional electron tomography.[106,107] In Chapter 4, this type of EELS tomography was applied to explore the distribution of the mineral and organic components of bone at the bone-implant interface in 3D. The second type is to use the full 4D dataset consisting of three spatial dimensions and energy loss as the fourth dimension to reconstruct the EELS spectrum volume (Figure 2-9) in which each voxel contains a complete EELS spectrum.[105] However, this approach demands intensive computation and is more useful for detecting unknown elements in 3D instead of studying the interested element distribution.

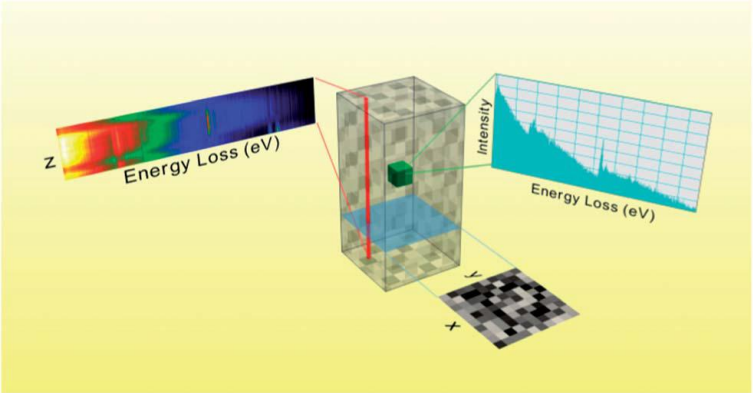

Figure 2-9. Schematic of the EELS spectrum volume. The 4D dataset shown here combines three spatial dimensions (X, Y, Z) with the energy loss as the fourth dimension. The figure was reproduced from reference[105] with permissions.

Additionally, spectroscopic X-ray data and EELS spectra images can be acquired simultaneously in HAADF STEM imaging mode. Thus, the simultaneous EDS and EELS tomography on the same specimen allows for correlative data while decreasing electron beam dose exposure. This correlative technique has been used to investigate the distribution of trace elements Na and Yb in Al-Si alloys.[108] The complementary use of the two analytical electron tomographies not only validates the presence of elements and their distribution but also builds towards nanoscale compositional quantification analysis in 3D.

2.4.2 Atom Probe Tomography

Atom probe tomography (APT), different from electron-based imaging instruments, is another promising 4D tomography technique which combines the capabilities of 3D imaging with sub-nanometer scale spatial resolution with equal chemical sensitivity for all elements at ppm mass resolution.[109,110] Evolving from the field ion microscope (FIM), APT is based on the time-controlled field evaporation of atoms at the specimen surface. The APT samples are prepared in a sharp needle shape with a tip radius approximate to 50 nm so that the high electrostatic field in the range of 10^{10} Vm^{-1}, which is necessary for field evaporation, can be produced at the sample tip surface by biasing the sample to a

few kilovolts.[111] Figure 2-10 shows the schematic view of APT and briefly outlines the data acquisition process.[109,111] In an APT experiment, a needle-shaped sample tip is subjected to a direct current (DC) voltage field which is just below threshold of atom evaporation. Additional energy, in the form of pulsed voltage for conductive materials or laser pulses for non-conductive samples, is superimposed onto the DC electrostatic field to enable pulsed field evaporation. The evaporated ions are accelerated by the electric field and fly through the counter-electrode to hit the 2D position-sensitive detector. The time from pulse to impact on the detector is recorded as time of flight t_{flight}. According to conservation laws, in this system the kinetic energy of an ion equals to its electric potential energy. Thus,

$$\frac{1}{2}mv^2 = neV \qquad (4)$$

Where m is the mass of the ion, v is the velocity of the ion flight, n is the charge number of the ion, e is the elementary charge and V is the voltage of the electrostatic field.

Also,

$$v = \frac{L_{flight}}{t_{flight}} \qquad (5)$$

where L_{flight} is the distance of the ion flight. After rearranging these two equations, it is shown that the mass to charge ratio of an ion is proportional to the time of flight.

$$\frac{m}{n} = \frac{2eV}{L_{flight}^2} t_{flight}^2 \qquad (6)$$

Thus, APT enables the elemental identification of the pulsed evaporated ions by using the time-of-flight mass spectrometry. Following data acquisition, the time-of-flight and 2D position of each ion recorded by the position-sensitive detector are reconstructed into a 3D point cloud where every point represents an elementally identified ion that has been positioned in the sample volume. This reconstructed volume can be further analyzed in the Integrated Visualization and Analysis Software (IVAS^{TM}) to extract and visualize the

nanoscale structural and chemical features of samples in 3D.

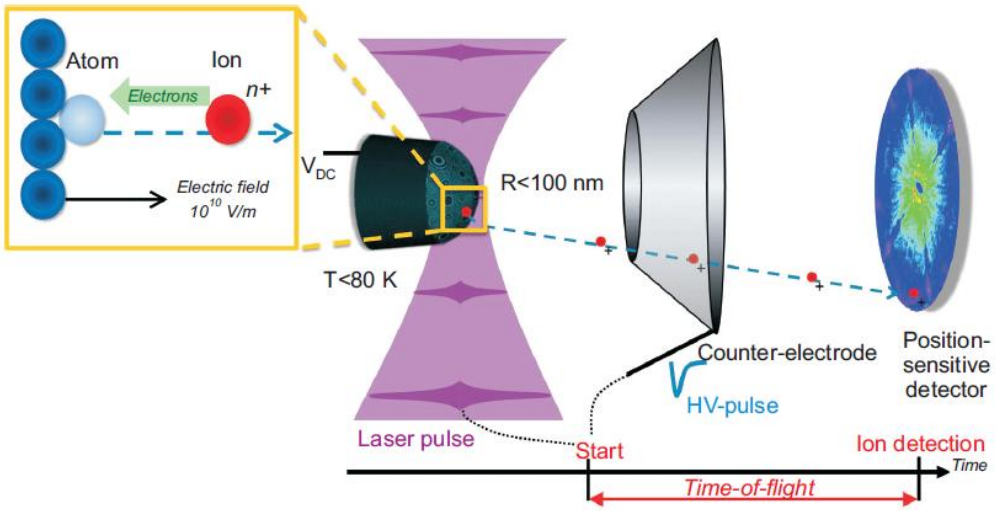

Figure 2-10. Schematic view of APT data acquisition. Ions are evaporated from the top tip of needle-shaped samples by the pulsed-voltage or pulsed-laser. Then, the evaporated ions are accelerated in the electric field and fly to hit the position-sensitive detector. The figure was reproduced from reference[109] with permissions.

APT data acquisition demands a strictly sharp needle-shaped sample geometry. The most prevalent sample preparation method is electrochemical polishing which is mostly feasible and reliable for conductive materials.[112] Advances in sample preparation using dual beam FIB SEM has expanded the range of APT applications to non-conductive materials such as semiconductor or biological samples.[113] Figure 2-11 shows an example FIB-based APT sample preparation protocol. A specific site of sample for lift-out is selected and protected by a layer of Pt or W deposition. This region-of-interest (ROI) is lifted out by a micromanipulator after being trenched on both sides to form a triangular wedge. This wedge is mounted on the Si microtip posts which are prefabricated on a silicon wafer and annularly milled by the Ga ion beam accelerated with 30 kV voltage. At the final sharpening and polishing step, a lower acceleration voltage in the range of a few kilovolts is used to minimize Ga implantation.

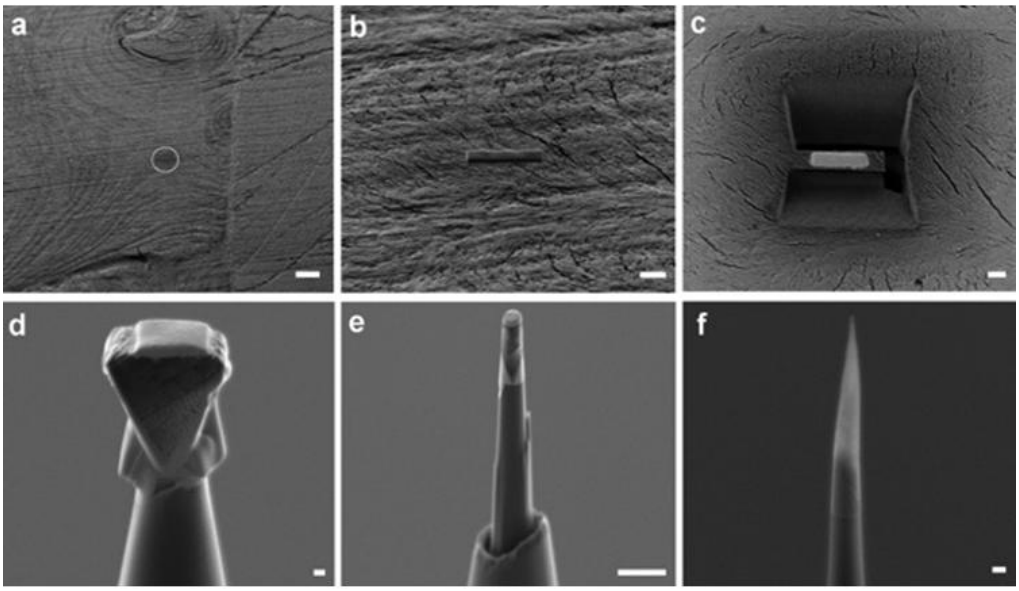

Figure 2-11. FIB-based APT sample preparation protocol. After an interested region is selected, a layer of tungsten is deposited for protection. Then the rough trenches are milled away for lift-out. The wedge is lifted out and mounted on the posts for annular milling to a final needle-shaped APT sample. Scale bars are 40 μm (a), 4 μm (b-e) and 200 nm (f) respectively. The figure was reproduced from our work in reference[34] with permissions.

Current studies are increasingly correlating APT results with other characterization techniques to refine APT reconstructions and provide complementary information. Correlative APT has been defined as conducting multimodal microscopy and spectroscopy analyses together with APT on the same needle sample.[110] One important motivation for correlative APT analyses is to improve the accuracy of APT reconstructions. SEM images, especially TEM or STEM images, can provide additional information about the specimen such as tip tangent or orientations of nanoscale features which can serve as reconstruction parameters or markers to assess or improve the accuracy of reconstructions.[38] It is also useful to correlate APT with TEM to understand the artifacts caused by trajectory aberration, as complex heterogeneous materials often evaporate unevenly in an APT experiment. Another significant motivation for correlative APT analyses is that APT can only provide elemental distribution in 3D but not chemical state or electronic structure information, which can be complemented by EELS or other

spectroscopy techniques.[110] In Chapter 4, we correlated APT with on-axis electron tomography, EELS tomography and spectroscopy techniques to probe the nanoscale chemical structure of the interface between human bone and a commercial titanium dental implant. The sample preparation for APT-TEM correlative studies follows the same FIB-based APT sample preparation protocol, but lift-outs need to be mounted on specimen holders which are compatible with a TEM. Electropolished W wire and pre-sharpened FIB half-grids have been reported as feasible specimen holders for this correlative technique.[114] In addition, mounting a heterogeneous specimen with the lower evaporation field value at the tip, i.e. bone before titanium, has higher probability of running smoothly in the APT. A specialized stub with two stems perpendicular to each other was designed to accomplish mounting lift-out wedge with expected orientation in FIB.[115]

Advances in instrumentation to implement laser-pulsing enabled the examination of non-conductive materials including biological samples and biomaterials in APT.[36] Gordon *et al.* used APT to visualize 3D chemical maps of organic fibres with surrounding nano-crystalline magnetite in chiton, from which they noticed the co-localization of sodium or magnesium within these fibres.[33] Additional research on elephant tusk dentin and rat bone also identified the preference of ion (Na^+) bonding with organic fibres.[116] Karlsson *et al.* applied APT to rat bone-implant interface research and observed Ca atoms contacting the implant surface directly, which supports the pure inorganic interface theory of osseointegration.[117] They also complemented APT results with TEM imaging in the study of a clinical-retrieved Ti-based dental implant with a sand-blasted acid etched surface to reveal the atomic structure of the human bone-implant interface.[118] Dental enamel has also been studied with APT as researchers have shown Mg-rich amorphous calcium phosphate (ACP) in the grain boundaries of the hydroxyapatite nanowires both in unpigmented rodent enamel[119] and mature human

dental enamel[120]. Despite significant progress of APT applications in biomaterials research, especially biominerals, there are still challenges. Firstly, these biominerals have poor thermal conductivity which leads to thermal tails in the mass spectrum. These thermal tails can mask peaks and can also influence quantitative analysis by contributing to a high background signal. Metallic coating or embedding the biomaterial samples in metallic matrix have been reported as efficient methods.[121] Gordon *et al.* embedded ferritin in a sandwiched Au-Pd metal matrix and presented the first 3D compositional structure of individual ferritin molecules.[122] In the study of human bone structure with APT, we sputter coated a 50 nm-thick Ag film on the surface of sample needles so as to improve the conductivity of samples and reduce the thermal tails in the mass spectrum.[34] Secondly, the heterogeneous nature of biomaterials results in uneven ion evaporation which leads to artifacts and aberrations in the reconstruction.[110] Correlating APT results with other imaging techniques has been regarded valuable in biomaterials APT research to conquer this challenge. In Chapter 4, the correlation of on-axis electron tomography with APT is presented.

2.5 *In-situ* Liquid Cell Transmission Electron Microscopy (TEM) Applications in Biomineralization Research

2.5.1 Introduction of Liquid Cell TEM

Liquid cell TEM has expanded the applications of TEM from imaging and analyzing solid samples to investigating real-time processes in the liquid state.[123] Advances in equipment and experimental techniques have enabled its wide applications in material science and biological research.[124] The key part of the liquid cell TEM equipment is the enclosed liquid cell which encapsulates a thin liquid layer within the vacuum of the TEM.[125] Figure 2-12 shows the schematic diagram of a liquid cell for TEM.[124] The commercialized modern microfabricated liquid cells are made of silicon chips containing vacuum-tight silicon nitride membranes that act as electron-transparent windows.[126] Two of such chips are sealed in the liquid cell holder with membrane windows aligned to

confine the liquid in a thin layer for imaging. The liquid is traditionally placed between chips by static or flowing approaches. In static cells, a limited volume of liquid is dropped on the window of one chip and then the other chip is placed on the top of it, sealing the liquid. This static experiment method was used to study the nucleation and growth process of calcium phosphate presented in Chapter 5. In flow cells, two liquid reagents are pumped separately at controlled speeds through fluid tubes into the liquid cell, allowing for the solutions to mix close to the upstream of the liquid cell. After imaging, the mixed solution exits the liquid cell through a third fluid tube as waste. The schematic drawing of a dual-inlet liquid flow holder was shown in Figure 2-13.[127]

Apart from encapsulating a thin layer liquid for imaging, the functions of liquid cell have been extended to investigate more complex processes by adding electrochemical electrodes and a controlled heater.[124] The apparatus that incorporates electrochemical electrodes enables the observation of ongoing electrochemical reactions, which has aided in the research of batteries and fuel cells.[128] Based on the heater coils patterned on chip membranes, the heating capability of liquid cells allow for the evaluation of the impact of temperature on the structural evolution of nanoparticles[129] and provide temperature-controlled liquid environment for temperature-sensitive biological studies.[130] Another significant ongoing development in liquid cell TEM is the correlative application of analytical microscopy including EDS, EELS, and diffraction patterns to reveal the chemical information and phase of samples.[131]

Despite the remarkable progress in technique development, liquid cell TEM has two intrinsic limitations: low image resolution and electron beam effects.[124] The thickness of the liquid cell that contains the liquid layer and two window membranes is the main reason imaging resolution is reduced. In addition, the membrane bulging effect, caused by the different pressure of the interior of the liquid cell from the microscope vacuum,

usually increases the thickness of liquid cell, in some cases up to several microns at the center of the windows.[126] In order to mitigate this deflection, many strategies have been made on window fabrications, e.g. fabricating long and narrow windows or using thicker and stiffer membranes with small wells as imaging windows. The second key limitation of liquid cell TEM is the radiation damage and artifacts caused by the electron beam. The radiolysis products of liquid including water, e.g. OH radicals, hydrated electrons, have complex effects on sample structures or processes under study.[132] They may also induce nanoparticle growth from solvated species.[133] Thus, it is important to determine the threshold of beam dose for each specific liquid cell experiment,[134] and also validate the results by comparing with *ex-situ* experiments.[124] The low-dose imaging method originally well-developed for cryogenic TEM (cryo-TEM) has been applied in liquid cell TEM experiments to limit the beam dose exposure of samples.[135]

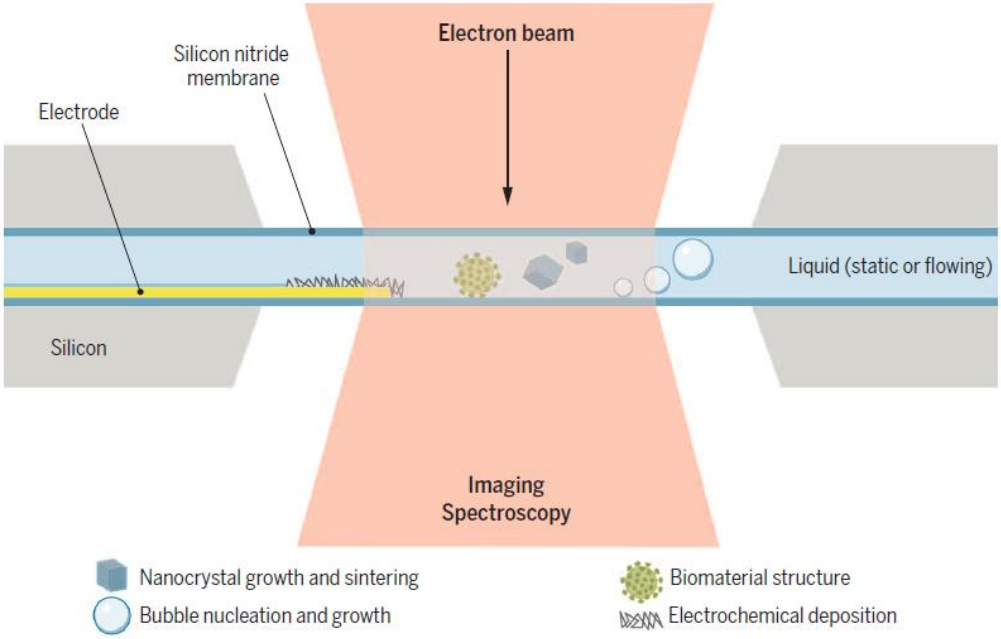

Figure 2-12. Schematic drawing of a liquid cell for TEM. The static or flowing liquid is confined between two electron-transparent silicon nitride membranes for imaging and spectroscopic analysis. This typical liquid cell for TEM has been applied in physical, biological and materials research. The figure was reproduced from reference[124] with permissions.

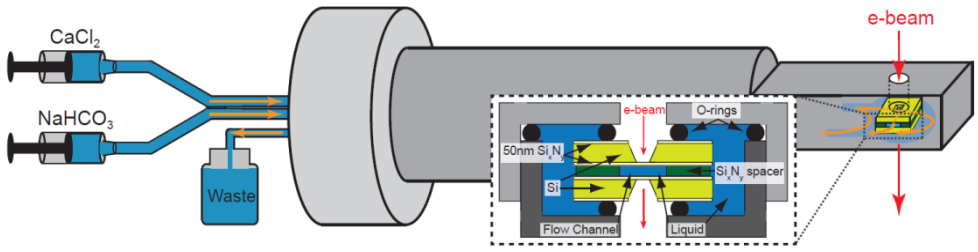

Figure 2-13. Schematic diagram of dual-inlet liquid flow holder. Two liquid reagents in syringes are pumped separately into the liquid cell through fluid tubes. They mix to react within the liquid cell region and exit the liquid cell through a third fluid tube as waste. The figure was reproduced from reference[127] with permissions.

2.5.2 Applications in Biomineralization Research

Biomineralization, the process by which minerals nucleate and grow under the direction of organic matrices, has widespread impacts on environmental, pathological, and materials research.[127] One of the most prevalent biominerals, calcium carbonate ($CaCO_3$), significantly influences the carbon cycling on a global scale.[136] In mammals, calcium phosphate (CaP) is the key component of mineralized tissues i.e. bones and teeth.[43] It is also involved in the pathological calcification processes of kidney stones and vascular calcification.[137] Biominerals usually have exquisite hierarchical structure and distinctive mechanical properties, which inspires studies on unveiling their biomineralization mechanisms, to allow us to synthesize biomimetic functional materials.[138] Since biomineralization is a dynamic process, *in-situ* X-ray microscopy[139] and spectroscopy[140] techniques have been applied to record the transition of morphology and phases during this process. However, considering that the early events of biomineral nucleation and growth are all on the nanometer length scale, these X-ray based characterization methods fail to provide enough spatial resolution. Cryo-TEM with the nanoscale spatial resolution has been proven as a useful technique to image the biomineralization process at different time points.[40,51,141] However, these snapshots over comparatively long time intervals cannot be direct evidence to elucidate pathways of nucleation and growth.[41] *In-situ* liquid cell TEM, combining nanoscale spatial and adequate temporal resolutions, allows for

real-time observation of initial particle formation from solvated states and subsequent morphology transformation.[127] Nielsen *et al.* reported the first real-time observation on $CaCO_3$ nucleation process using liquid cell TEM.[142] Multiple nucleation pathways were demonstrated to occur simultaneously, including the direct formation of crystalline phases (vaterite, aragonite, and calcite) from solution, and the indirect pathways transforming from amorphous calcium carbonate (ACC) into crystalline phases (vaterite and aragonite). Organic matrices have been known to play significant roles in directing biomineralization.[143] Smeets *et al.* used *in-situ* liquid cell TEM data to illustrate the precise functions of a macromolecular matrix of polystyrene sulphonate (PSS) in $CaCO_3$ biomineralization process.[134] By binding Ca ions, PSS forms hydrated globules which act as preferred nucleation sites to generate metastable phase ACC. In Chapter 5, we also applied the liquid cell TEM to study the initial nucleation and growth process of CaP. Since CaP biomineralization is the basis of bone formation at implant surface, this work provides the foundation for further investigating the dynamic bone mineralization process on implant interfaces in liquid.

References

(1) Florencio-Silva, R.; Sasso, G. R. D. S.; Sasso-Cerri, E.; Simões, M. J.; Cerri, P. S. Biology of Bone Tissue: Structure, Function, and Factors That Influence Bone Cells. *Biomed Res. Int.* **2015**, *2015*, 1–17.

(2) Saini, M. Implant Biomaterials: A Comprehensive Review. *World J. Clin. Cases* **2015**, *3*, 52.

(3) Grandfield, K. Bone, Implants, and Their Interfaces. *Phys. Today* **2015**, *68*, 40–45.

(4) Brånemark, R.; Brånemark, P. I.; Rydevik, B.; Myers, R. R. Osseointegration in Skeletal Reconstruction and Rehabilitation: A Review. *J. Rehabil. Res. Dev.* **2001**, *38*, 175–181.

(5) Goutam, M.; Chandu, G. S.; Mishra, S. K.; Singh, M.; Tomar, B. S. Factors Affecting Osseointegration : A Literature Review. *J. Orofac. Res.* **2013**, *3*, 197–201.

(6) Palmquist, A.; Lindberg, F.; Emanuelsson, L.; Brånemark, R.; Engqvist, H.; Thomsen, P. Biomechanical,histological, and Ultrastructural Analyses of Laser Micro- and Nano-Structured Titanium Alloy Implants : A Study in Rabbit. *J. Biomed. Mater. Res. Part A* **2008**, *92A*, 1476–1485.

(7) Palmquist, A.; Jarmar, T.; Emanuelsson, L.; Brånemark, R.; Engqvist, H.; Thomsen, P. Forearm Bone-Anchored Amputation Prosthesis. *Acta Orthop.* **2008**, *1*, 78–85.

(8) Jarmar, T.; Palmquist, A.; Brånemark, R.; Hermansson, L.; Engqvist, H.; Thomsen, P. Characterization of the Surface Properties of Commercially Available Dental Implants Using

Scanning Electron Microscopy, Focused Ion Beam, and High-Resolution Transmission Electron Microscopy. *Clin. Implant Dent. Relat. Res.* **2008**, *10*, 11–22.

(9) Swain, M. V; Xue, J. State of the Art of Micro-CT Applications in Dental Research. *Int. J. Oral Sci.* **2009**, *1*, 177–188.

(10) Arvidsson, A.; Sarve, H.; Johansson, C. B. Comparing and Visualizing Titanium Implant Integration in Rat Bone Using 2D and 3D Techniques. *J. Biomed. Mater. Res. Part B Appl. Biomater.* **2015**, *103*, 12–20.

(11) Carlo, M.; Adriano, P.; Francesco, M.; Franco, R.; Awad, S. J.; Giovanna, L.; Alessandra, G. Histological and Synchrotron Radiation-Based Computed Microtomography Study of 2 Human-Retrieved Direct Laser Metal Formed Titanium Implants. *Implant Dent.* **2013**, *0*, 1–5.

(12) Thorfve, A.; Palmquist, A.; Grandfield, K. Three-Dimensional Analytical Techniques for Evaluation of Osseointegrated Titanium Implants. *Mater. Sci. Technol.* **2015**, *31*, 174–179.

(13) Van Lenthe, G. H.; Hagenmüller, H.; Bohner, M.; Hollister, S. J.; Meinel, L.; Müller, R. Nondestructive Micro-Computed Tomography for Biological Imaging and Quantification of Scaffold-Bone Interaction in Vivo. *Biomaterials* **2007**, *28*, 2479–2490.

(14) Kotula, P. G.; Keenan, M. R.; Michael, J. R. Microscopy Microanalysis Tomographic Spectral Imaging with Multivariate Statistical Analysis : Comprehensive 3D Microanalysis. *Microsc. Microanal.* **2006**, *12*, 36–48.

(15) Lasagni, F. A.; Lasagni, A. F.; Huertas-Olivares, I.; Holazapfel, C.; Mücklich, F. 3D Nano-Characterisation of Materials by FIB-SEI/EDS Tomography. *IOP Conf. Ser. Mater. Sci. Eng.* **2010**, *7*, 012016.

(16) Giannuzzi, L. A.; Phifer, D.; Giannuzzi, N. J.; Capuano, M. J. Two-Dimensional and 3-Dimensional Analysis of Bone/Dental Implant Interfaces With the Use of Focused Ion Beam and Electron Microscopy. *J. Oral Maxillofac. Surg.* **2007**, *65*, 737–747.

(17) Uchic, M. D.; Holzer, L.; Inkson, B. J.; Principe, E. L.; Munroe, P. Three-Dimensional Microstructural Characterization Using Focused Ion Beam Tomography. *MRS Bull.* **2007**, *32*, 408–416.

(18) Cantoni, M.; Holzer, L. Advances in 3D Focused Ion Beam Tomography. *MRS Bull.* **2014**, *39*, 354–360.

(19) Schneider, P.; Meier, M.; Wepf, R.; Müller, R. Serial FIB/SEM Imaging for Quantitative 3D Assessment of the Osteocyte Lacuno-Canalicular Network. *Bone* **2011**, *49*, 304–311.

(20) Grandfield, K.; Engqvist, H. Focused Ion Beam in the Study of Biomaterials and Biological Matter. *Adv. Mater. Sci. Eng.* **2012**, *2012*, 6.

(21) Reznikov, N.; Shahar, R.; Weiner, S. Three-Dimensional Structure of Human Lamellar Bone: The Presence of Two Different Materials and New Insights into the Hierarchical Organization. *Bone* **2014**, *59*, 93–104.

(22) Reznikov, N.; Almany-Magal, R.; Shahar, R.; Weiner, S. Three-Dimensional Imaging of Collagen Fibril Organization in Rat Circumferential Lamellar Bone Using a Dual Beam Electron Microscope Reveals Ordered and Disordered Sub-Lamellar Structures. *Bone* **2013**, *52*, 676–683.

(23) Midgley, P. A; Dunin-Borkowski, R. E. Electron Tomography and Holography in Materials Science. *Nat. Mater.* **2009**, *8*, 271–280.

(24) Grandfield, K.; Palmquist, A.; Engqvist, H. Three-Dimensional Structure of Laser-Modified Ti6Al4V and Bone Interface Revealed with STEM Tomography. *Ultramicroscopy* **2013**, *127*, 48–52.

(25) Grandfield, K.; Palmquist, A.; Engqvist, H. High-Resolution Three-Dimensional Probes of Biomaterials and Their Interfaces. *Philos. Trans. R. Soc. A* **2012**, *370*, 1337–1351.

(26) Grandfield, K.; Gustafsson, S.; Palmquist, A. Where Bone Meets Implant: The Characterization of Nano-Osseointegration. *Nanoscale* **2013**, *5*, 4302–4308.

(27) Grandfield, K.; McNally, E. A; Palmquist, A; Botton, G. A; Thomsen, P.; Engqvist, H. Visualizing Biointerfaces in Three Dimensions: Electron Tomography of the Bone-Hydroxyapatite Interface. *J. R. Soc. Interface* **2010**, *7*, 1497–1501.

(28) Kaneko, T.; Nishioka, H.; Nishi, T.; Jinnai, H. Reduction of Anisotropic Image Resolution in Transmission Electron Microtomography by Use of Quadrangular Prism-Shaped Section. *J. Electron Microsc. (Tokyo).* **2005**, *54*, 437–444.

(29) Kawase, N.; Kato, M.; Nishioka, H.; Jinnai, H. Transmission Electron Microtomography without the "Missing Wedge" for Quantitative Structural Analysis. *Ultramicroscopy* **2007**, *107*, 8–15.

(30) Ke, X.; Bals, S.; Cott, D.; Hantschel, T.; Bender, H.; Van Tendeloo, G. Three-Dimensional Analysis of Carbon Nanotube Networks in Interconnects by Electron Tomography without Missing Wedge Artifacts. *Microsc. Microanal.* **2010**, *16*, 210–217.

(31) Yaguchi, T.; Konno, M.; Kamino, T.; Watanabe, M. Observation of Three-Dimensional Elemental Distributions of a Si Device Using a 360 °-Tilt FIB and the Cold Field-Emission STEM System. *Ultramicroscopy* **2008**, *108*, 1603–1615.

(32) Biermans, E.; Molina, L.; Batenburg, K. J.; Bals, S.; Van Tendeloo, G. Measuring Porosity at the Nanoscale by Quantitative Electron Tomography. *Nano Lett.* **2010**, *10*, 5014–5019.

(33) Gordon, L. M.; Joester, D. Nanoscale Chemical Tomography of Buried Organic-Inorganic Interfaces in the Chiton Tooth. *Nature* **2011**, *469*, 194–197.

(34) Langelier, B.; Wang, X.; Grandfield, K. Atomic Scale Chemical Tomography of Human Bone. *Sci. Rep.* **2017**, *7*, 39958.

(35) Sul, Y. T. The Significance of the Surface Properties of Oxidized Titanium to the Bone Response: Special Emphasis on Potential Biochemical Bonding of Oxidized Titanium Implant. *Biomaterials* **2003**, *24*, 3893–3907.

(36) Gault, B.; Moody, M. P.; Cairney, J. M.; Ringer, S. P. Atom Probe Crystallography. *Mater. Today* **2012**, *15*, 2–10.

(37) Devaraj, A.; Gu, M.; Colby, R.; Yan, P.; Wang, C. M.; Zheng, J. M.; Xiao, J.; Genc, A.; Zhang, J. G.; Belharouak, I.; *et al.* Visualizing Nanoscale 3D Compositional Fluctuation of Lithium in Advanced Lithium-Ion Battery Cathodes. *Nat. Commun.* **2015**, *6*, 8014.

(38) Arslan, I.; Marquis, E. A.; Homer, M.; Hekmaty, M. A.; Bartelt, N. C. Towards Better 3-D Reconstructions by Combining Electron Tomography and Atom-Probe Tomography. *Ultramicroscopy* **2008**, *108*, 1579–1585.

(39) Zhu, X.; Hitchcock, A. P.; Bittencourt, C.; Umek, P.; Kruger, P. Individual Titanate Nanoribbons Studied by 3D-Resolved Polarization Dependent X-Ray Absorption Spectra Measured with Scanning Transmission X-Ray Microscopy. *J. Phys. Chem. C* **2015**, *119*, 24192–24200.

(40) Habraken, W. J. E. M.; Tao, J.; Brylka, L. J.; Friedrich, H.; Bertinetti, L.; Schenk, A. S.; Verch, A.; Dmitrovic, V.; Bomans, P. H. H.; Frederik, P. M.; *et al.* Ion-Association Complexes Unite Classical and Non-Classical Theories for the Biomimetic Nucleation of Calcium Phosphate. *Nat. Commun.* **2013**, *4*, 1507.

(41) De Yoreo, J. J.; Gilbert, P. U. P. a.; Sommerdijk, N. a. J. M.; Penn, R. L.; Whitelam, S.; Joester, D.; Zhang, H.; Rimer, J. D.; Navrotsky, a.; Banfield, J. F.; *et al.* Crystallization by Particle Attachment in Synthetic, Biogenic, and Geologic Environments. *Science.* **2015**, *349*, aaa6760–aaa6760.

(42) Lausch, A. J.; Quan, B. D.; Miklas, J. W.; Sone, E. D. Extracellular Matrix Control of Collagen Mineralization in Vitro. *Adv. Funct. Mater.* **2013**, *23*, 4906–4912.

(43) Olszta, M. J.; Cheng, X.; Jee, S. S.; Kumar, R.; Kim, Y. Y.; Kaufman, M. J.; Douglas, E. P.; Gower, L. B. Bone Structure and Formation: A New Perspective. *Mater. Sci. Eng. R Reports* **2007**, *58*, 77–116.

(44) Wang, X.; Shah, F. A.; Palmquist, A.; Grandfield, K. 3D Characterization of Human Nano-Osseointegration by On-Axis Electron Tomography without the Missing Wedge. *ACS Biomater. Sci. Eng.* **2017**, *3*, 49–55.

(45) Baron, R. Chapter 1 . Anatomy and Ultrastructure of Bone - Histogenesis, Growth and Remodeling. Bone as an Organ : Macroscopic Organization Bone as a Tissue : Bone Matrix and Mineral. In; 2008; Vol. i, pp. 1–24.

(46) Wegst, U. G. K.; Bai, H.; Saiz, E.; Tomsia, A. P.; Ritchie, R. O. Bioinspired Structural Materials. *Nat. Mater.* **2008**, *14*, 1053–1054.

(47) Fogelman, I.; Van Der Wall, H.; Gnanasegaran, G. Radionuclide and Hybrid Bone Imaging. *Radionucl. Hybrid Bone Imaging* **2012**, *9783642024*, 1–1046.

(48) Beniash, E. Biominerals - Hierarchical Nanocomposites : The Example of Bone. **2012**, 1–41.

(49) Hu, Y.-Y.; Rawal, A.; Schmidt-Rohr, K. Strongly Bound Citrate Stabilizes the Apatite Nanocrystals in Bone. *Proc. Natl. Acad. Sci.* **2010**, *107*, 22425–22429.

(50) Nudelman, F.; Lausch, A. J.; Sommerdijk, N. A. J. M.; Sone, E. D. In Vitro Models of Collagen Biomineralization. *J. Struct. Biol.* **2013**, *183*, 258–269.

(51) Nudelman, F.; Pieterse, K.; George, A.; Bomans, P. H. H.; Friedrich, H.; Brylka, L. J.; Hilbers, P. A.; de With, G.; Sommerdijk, N. A. J. M. The Role of Collagen in Bone Apatite Formation in the Presence of Hydroxyapatite Nucleation Inhibitors. *Nat. Mater.* **2010**, *9*, 1004–1009.

(52) Takata, M. K.; Saiki, M.; Sumita, N. M.; Saldiva, P. H. N.; Pasqualucci, C. A. Trace Element Determinations in Human Cortical and Trabecular Bones. *J. Radioanal. Nucl. Chem.* **2005**, *264*, 5–8.

(53) Pemmer, B.; Roschger, A.; Wastl, A.; Hofstaetter, J. G.; Wobrauschek, P.; Simon, R.; Thaler, H. W.; Roschger, P.; Klaushofer, K.; Streli, C. Spatial Distribution of the Trace Elements Zinc, Strontium and Lead in Human Bone Tissue. *Bone* **2013**, *57*, 184–193.

(54) Farzadi, A.; Bakhshi, F.; Solati-Hashjin, M.; Asadi-Eydivand, M.; Osman, N. A. A. Magnesium Incorporated Hydroxyapatite: Synthesis and Structural Properties Characterization. *Ceram. Int.* **2014**, *40*, 6021–6029.

(55) Weiner, S.; Wagner, H. D. The Material Bone: Structure-Mechanical Function Relations. *Annu. Rev. Mater. Sci.* **1998**, *28*, 271–298.

(56) Ritchie, R. O.; Buehler, M. J.; Hansma, P. Plasticity and Toughness in Bone. *Phys. Today* **2009**, *62*, 41–47.

(57) Landis, W. J.; Song, M. J.; Leith, A.; Mcewen, L.; Mcewen, B. F. Mineral and Organic Matrix Interaction in Normally Calcifying Tendon Visualized in Three Dimensions by High-Voltage Electron Microscopic Tomography and Graphic Image Reconstruction. *J. Struct.* **1993**, *110*, 39–54.

(58) Schwarcz, H. P. The Ultrastructure of Bone as Revealed in Electron Microscopy of Ion-Milled Sections. *Semin. Cell Dev. Biol.* **2015**, *46*, 44–50.

(59) Alexander, B.; Daulton, T. L.; Genin, G. M.; Lipner, J.; Pasteris, J. D.; Wopenka, B.; Thomopoulos, S. The Nanometre-Scale Physiology of Bone: Steric Modelling and Scanning Transmission Electron Microscopy of Collagen-Mineral Structure. *J. R. Soc. Interface* **2012**, *9*, 1774–1786.

(60) McNally, E. A.; Schwarcz, H. P.; Botton, G. A.; Arsenault, A. L. A Model for the Ultrastructure of Bone Based on Electron Microscopy of Ion-Milled Sections. *PLoS One* **2012**, *7*, 1–12.

(61) Schwarcz, H. P.; McNally, E. A.; Botton, G. A. Dark-Field Transmission Electron Microscopy of Cortical Bone Reveals Details of Extrafibrillar Crystals. *J. Struct. Biol.* **2014**, *188*, 240–248.

(62) Davies, J. E. Bone Bonding at Natural and Biomaterial Surfaces. *Biomaterials* **2007**, *28*, 5058–5067.

(63) Su, X.; Sun, K.; Cui, F. Z.; Landis, W. J. Organization of Apatite Crystals in Human Woven Bone. *Bone* **2003**, *32*, 150–162.

(64) Kuzyk, P. R.; Schemitsch, E. H. The Basic Science of Peri-Implant Bone Healing. *Indian J. Orthop.* **2011**, *45*, 108–115.

(65) Cooper, D. M. L.; Erickson, B.; Peele, A. G.; Hannah, K.; Thomas, C. D. L.; Clement, J. G. Visualization of 3D Osteon Morphology by Synchrotron Radiation Micro-CT. *J. Anat.* **2011**, *219*, 481–489.

(66) Clarke, B. Normal Bone Anatomy and Physiology. *Clin. J. Am. Soc. Nephrol.* **2008**, *3 Suppl 3*, 131–139.

(67) Murthy, K. R.; Morrow, P. .; Theriault, R. L. Bone Biology and the Role of RANK Ligand Pathway. *Oncol. J.* **2009**, *23*, 30–31.

(68) Canada Institute for Health Information. *Canadian Joint Replacement Registry Annual Report: Hip and Knee Replacements in Canada, 2014-2015*; 2017; pp. 2014–2015.

(69) Shah, F. A.; Trobos, M.; Thomsen, P.; Palmquist, A. Commercially Pure Titanium (cp-Ti) versus Titanium Alloy (Ti6Al4V) Materials as Bone Anchored Implants - Is One Truly Better than the Other? *Mater. Sci. Eng. C* **2016**, *62*, 960–966.

(70) Palmquist, A.; Grandfield, K.; Norlindh, B.; Mattsson, T.; Branemark, R.; Thomsen, P. Bone-Titanium Oxide Interface in Humans Revealed by Transmission Electron Microscopy and Electron Tomography. *J. R. Soc. Interface* **2012**, *9*, 396–400.

(71) Shah, F. A.; Nilson, B.; Brånemark, R.; Thomsen, P.; Palmquist, A. The Bone-Implant Interface-Nanoscale Analysis of Clinically Retrieved Dental Implants. *Nanomedicine* **2014**, *10*, 1729–1737.

(72) McCracken, M. Dental Implant Materials: Commercially Pure Titanium and Titanium Alloys. *J. Prosthodont.* **1999**, *8*, 40–43.

(73) Shah F.A.; Grandfield K.; Palmquist A.. Laser Surface Modification and the Tissue-Implant Interface. In *Laser Surface Modification of Biomaterials*; 2016; pp. 253–275.

(74) Forsgren, J.; Svahn, F.; Jarmar, T.; Engqvist, H. Formation and Adhesion of Biomimetic Hydroxyapatite Deposited on Titanium Substrates. *Acta Biomater.* **2007**, *3*, 980–984.

(75) Palmquist, A.; Johansson, A.; Suska, F.; Brånemark, R.; Thomsen, P. Acute Inflammatory Response to Laser-Induced Micro- and Nano-Sized Titanium Surface Features. *Clin. Implant Dent. Relat. Res.* **2013**, *15*, 96–104.

(76) Brånemark, P. I.; Breine, U.; Adell, R.; Hansson, B. O.; Lindström, J.; Ohlsson, A. Intra-Osseous Anchorage of Dental Prostheses. I. Experimental Studies. *Scand. J. Plast. Reconstr. Surg.* **1969**, *3*, 81–100.

(77) Davies, J. E. Understanding Peri-Implant Endosseous Healing. *J. Dent. Educ.* **2003**, *67*, 932–949.

(78) Davies, J. E.; Ajami, E.; Moineddin, R.; Mendes, V. C. The Roles of Different Scale Ranges of Surface Implant Topography on the Stability of the Bone/implant Interface. *Biomaterials* **2013**, *34*, 3535–3546.

(79) Davies, J. E.; Mendes, V. C.; Ko, J. C. H.; Ajami, E. Topographic Scale-Range Synergy at the Functional Bone/implant Interface. *Biomaterials* **2014**, *35*, 25–35.

(80) Klinger, M. M.; Rahemtulla, F.; Prince, C. W.; Lucas, L. C.; Lemons, J. E. Proteoglycans at the Bone-Implant Interface. *Crit. Rev. Oral Biol. Med.* **1998**, *9*, 449–463.

(81) Albrektsson T. and Hansson H-A. Interface Analysis of Titanium and Zirconium Bone Implants. Biomaterials **1985**, *6*, 97-101.

(82) Steflik D. E., Sisk A. L., Parr G. R., Gardner L. K., Hanes P. J., Lake F. T., *et al.* High-Voltage Electron Microscopy and Conventional Transmission Electron Microscopy of the Interface Zone between Bone and Endosteal Dental Implants. *J. Biomed. Mater. Res.* **1992**, *26*, 529-545.

(83) McKee, M. D.; Nanci, A. Osteopontin at Mineralized Tissue Interfaces in Bone, Teeth, and Osseointegrated Implants: Ultrastructural Distribution and Implications for Mineralized Tissue Formation, Turnover, and Repair. *Microsc. Res. Tech.* **1996**, *33*, 141–164.

(84) Shah, F. A.; Wang, X.; Thomsen, P.; Grandfield, K.; Palmquist, A. High-Resolution Visualization of the Osteocyte Lacuno-Canalicular Network Juxtaposed to the Surface of Nanotextured Titanium Implants in Human. *ACS Biomater. Sci. Eng.* **2015**, *1*, 305–313.

(85) Withers, P. J.; Preuss, M. Fatigue and Damage in Structural Materials Studied by X-Ray Tomography. *Annu. Rev. Mater. Res.* **2012**, *42*, 81–103.

(86) Obst, M.; Wang, J.; Hitchcock, A. P. Soft X-Ray Spectro-Tomography Study of Cyanobacterial Biomineral Nucleation. *Geobiology* **2009**, *7*, 577–591.

(87) Buckley, C. J.; Khaleque, N.; Bellamy, S. J.; Robbins, M.; Zhang, X. Mapping the Organic and Inorganic Components of Osteoporotic Bone. *X-ray Microsc. Spectromicroscopy* **1997**.

(88) Reznikov, N.; Shahar, R.; Weiner, S. Bone Hierarchical Structure in Three Dimensions. *Acta Biomater.* **2014**, *10*, 3815–3826.

(89) Friedrich, H.; De Jongh, P. E.; Verkleij, A. J.; De Jong, K. P. Electron Tomography for Heterogeneous Catalysts and Related Nanostructured Materials. *Chem. Rev.* **2009**, *109*, 1613–1629.

(90) R.A.Crowther; L.A.Amos; J.T.Finch; Rosier, D. J. De; A. Klug. Three Dimensional Reconstructions of Spherical Viruses by Fourier Synthesis from Electron Micrographs. *Nature* **1970**, *226*, 421–425.

(91) Ercius, P.; Alaidi, O.; Rames, M. J.; Ren, G. Electron Tomography: A Three-Dimensional Analytic Tool for Hard and Soft Materials Research. *Adv. Mater.* **2015**, *27*, 5638–5663.

(92) Kübel, C.; Voigt, A.; Schoenmakers, R.; Otten, M.; Su, D.; Lee, T.-C.; Carlsson, A.; Bradley, J. Recent Advances in Electron Tomography: TEM and HAADF-STEM Tomography for Materials Science and Semiconductor Applications. *Microsc. Microanal.* **2005**, *11*, 378–400.

(93) Penczek, P. A. Fundamentals of Three-Dimensional Recostruction from Projections. *Methods Enzymol.* **2010**, *482*, 1–28.

(94) Sugimori, H.; Nishi, T.; Jinnai, H. Dual-Axis Electron Tomography for Three-Dimensional Observations of Polymeric Nanostructures. *Macromolecules* **2005**, *38*, 10226–10233.

(95) Penczek, P.; Marko, M.; Buttle, K.; Frank, J. Double-Tilt Electron Tomography. *Ultramicroscopy* **1995**, *60*, 393–410.

(96) Mastronarde, D. N. Dual-Axis Tomography: An Approach with Alignment Methods That Preserve Resolution. *J. Struct. Biol.* **1997**, *120*, 343–352.

(97) Möbus, G.; Doole, R. C.; Inkson, B. J. Spectroscopic Electron Tomography. *Ultramicroscopy* **2003**, *96*, 433–451.

(98) Verbeeck, J.; Van Dyck, D.; Van Tendeloo, G. Energy-Filtered Transmission Electron Microscopy: An Overview. *Spectrochim. Acta - Part B At. Spectrosc.* **2004**, *59*, 1529–1534.

(99) Jin-Phillipp, N. Y.; Koch, C. T.; van Aken, P. A. Toward Quantitative Core-Loss EFTEM Tomography. *Ultramicroscopy* **2011**, *111*, 1255–1261.

(100) Aronova M. A.; Leapman R. D.. Development of Electron Energy Loss Spectroscopy in the Biological Sciences. *MRS Bull.* **2013**, *37*, 53–62.

(101) Slater, T. J. a; Janssen, A.; Camargo, P. H. C.; Burke, M. G.; Zaluzec, N. J.; Haigh, S. J. STEM-EDX Tomography of Bimetallic Nanoparticles: A Methodological Investigation. *Ultramicroscopy* **2016**, *162*, 61–73.

(102) Lepinay, K.; Lorut, F.; Pantel, R.; Epicier, T. Chemical 3D Tomography of 28nm High K Metal Gate Transistor: STEM XEDS Experimental Method and Results. *Micron* **2013**, *47*, 43–49.

(103) Genc, A.; Kovarik, L.; Gu, M.; Cheng, H.; Plachinda, P.; Pullan, L.; Freitag, B.; Wang, C. XEDS STEM Tomography for 3D Chemical Characterization of Nanoscale Particles. *Ultramicroscopy* **2013**, *131*, 24–32.

(104) Jarausch, K.; Thomas, P.; Leonard, D. N.; Twesten, R.; Booth, C. R. Four-Dimensional STEM-EELS: Enabling Nano-Scale Chemical Tomography. *Ultramicroscopy* **2009**, *109*, 326–337.

(105) Yedra, L.; Eljarrat, A.; Rebled, J. M.; López-Conesa, L.; Dix, N.; Sánchez, F.; Estradé, S.; Peiró, F. EELS Tomography in Multiferroic Nanocomposites: From Spectrum Images to the Spectrum Volume. *Nanoscale* **2014**, *6*, 6646–6650.

(106) Yedra, L.; Eljarrat, A.; Arenal, R.; Pellicer, E.; Cabo, M.; López-Ortega, A.; Estrader, M.; Sort, J.; Baró, M. D.; Estradé, S.; *et al.* EEL Spectroscopic Tomography: Towards a New Dimension in Nanomaterials Analysis. *Ultramicroscopy* **2012**, *122*, 12–18.

(107) Yedra, L.; Eljarrat, A.; Arenal, R.; López-Conesa, L.; Pellicer, E.; López-Ortega, A.; Estrader, M.; Sort, J.; Baró, M. D.; Estradé, S.; *et al.* Electron Energy-Loss Spectroscopic Tomography of $Fe_XCo_{(3-x)}O_4$ Impregnated Co_3O_4 Mesoporous Particles: Unraveling the Chemical Information in Three Dimensions. *Analyst* **2016**, *141*, 4968–4972.

(108) Haberfehlner, G.; Orthacker, A.; Albu, M.; Li, J.; Kothleitner, G. Nanoscale Voxel Spectroscopy by Simultaneous EELS and EDS Tomography. *Nanoscale* **2014**, *6*, 14563–14569.

(109) Gault, B. A Brief Overview of Atom Probe Tomography Research. *Appl. Microsc.* **2016**, *46*, 117–126.

(110) Devaraj, A.; Perea, D. E.; Liu, J.; Gordon, L. M.; Prosa, T. J.; Parikh, P.; Diercks, D. R.; Meher, S.; Kolli, R. P.; Meng, Y. S.; *et al.* Three-Dimensional Nanoscale Characterisation of Materials by Atom Probe Tomography. *Int. Mater. Rev.* **2017**, *6608*, 1–34.

(111) Miller, M. K; Forbes, R.G.. *Atom Probe Tomography and the Local Electrode Atom Probe*; 2000; Springer.

(112) Larson, D. J.; Prosa, T. J.; Ulfig, R. M.; Geiser, B. P.; Kelly, T. F. *Local Electrode Atom Probe Tomography*; 2013; Springer.

(113) Thompson, K.; Lawrence, D.; Larson, D. J.; Olson, J. D.; Kelly, T. F.; Gorman, B. In Situ Site-Specific Specimen Preparation for Atom Probe Tomography. *Ultramicroscopy* **2007**, *107*, 131–139.

(114) Gorman, B.; Diericks, D.; Salmon, N. Hardware and Techniques for Cross-Correlative TEM and Atom Probe Analysis. *Micros. Today* **2008**, *4*, 42–48.

(115) Huang, J.; Wang, X.; Grandfield, K. FIB Preparation of Bone-Implant Interfaces for Correlative On-Axis Rotation Electron Tomography and Atom Probe Tomography. *Microsc. Microanal.* **2014**, *20*, 352–353.

(116) Gordon, L. M.; Tran, L.; Joester, D. Atom Probe Tomography of Apatites and Bone-Type Mineralized Tissues. *ACS Nano* **2012**, *6*, 10667–10675.

(117) Karlsson, J.; Sundell, G.; Thuvander, M.; Andersson, M. Atomically Resolved Tissue Integration. *Nano Lett.* **2014**, *14*, 4220–4223.

(118) Sundell, G.; Dahlin, C.; Andersson, M.; Thuvander, M. The Bone-Implant Interface of Dental Implants in Humans on the Atomic Scale. *Acta Biomater.* **2016**, *48*, 445–450.

(119) Gordon, L. M.; Cohen, M. J.; MacRenaris, K. W.; Pasteris, J. D.; Seda, T.; Joester, D. Amorphous Intergranular Phases Control the Properties of Rodent Tooth Enamel. *Science.* **2015**, *347*, 746–750.

(120) La Fontaine, A.; Zavgorodniy, A.; Liu, H.; Zheng, R.; Swain, M.; Cairney, J. Atomic-Scale Compositional Mapping Reveals Mg-Rich Amorphous Calcium Phosphate in Human Dental Enamel. *Sci. Adv.* **2016**, *2*, e1601145.

(121) Adineh, V. R.; Marceau, R. K. W.; Velkov, T.; Li, J.; Fu, J. Near-Atomic Three-Dimensional Mapping for Site-Specific Chemistry of "Superbugs." *Nano Lett.* **2016**, *16*, 7113–7120.

(122) Gordon, L. M.; Cohen, M. J.; Joester, D. Towards Atom Probe Tomography of Hybrid Organic-Inorganic Nanoparticles. *Microsc. Microanal.* **2013**, *19*, 952–953.

(123) De Jonge, N.; Ross, F. M. Electron Microscopy of Specimens in Liquid. *Nat. Nanotechnol.* **2011**, *6*, 695–704.

(124) Ross, F. M. Opportunities and Challenges in Liquid Cell Electron Microscopy. *Science.* **2015**, *350*, 1–9.

(125) Liao, H.-G.; Zheng, H. Liquid Cell Transmission Electron Microscopy. *Annu. Rev. Phys. Chem.* **2016**, *67*, 719–747.

(126) Jensen, E.; Mølhave, K. Encapsulated Liquid Cells for Transmission Electron Microscopy. In *liquid cell electron microscopy*; 2017; pp. 35–55.

(127) Nielsen, M. H.; Yoreo, J. J. De. Liquid Cell TEM for Studying Environmental and Biological Mineral Systems. In *liquid cell electron microscopy*; 2017; pp. 316–333.

(128) Ross, F. M.; Wang, C.; De Jonge, N. Transmission Electron Microscopy of Specimens and Processes in Liquids. *MRS Bull.* **2016**, *41*, 791–803.

(129) Dillon, S. J.; Chen, X. Temperature Control in Liquid Cells for TEM. In *Liquid Cell Electron Microscopy*; 2016; pp. 127–139.

(130) Elgrabli, D.; Dachraoui, W.; Ménard-Moyon, C.; Liu, X. J.; Bégin, D.; Bégin-Colin, S.; Bianco, A.; Gazeau, F.; Alloyeau, D. Carbon Nanotube Degradation in Macrophages: Live Nanoscale Monitoring and Understanding of Biological Pathway. *ACS Nano* **2015**, *9*, 10113–10124.

(131) Holtz, M. E.; Muller, D. A; Zaluzec, N. J. Analytical Electron Microscopy during In Situ Liquid Cell Studies. *Liq. Cell Electron Microsc.* **2016**, 410–436.

(132) Schneider, N. M.; Norton, M. M.; Mendel, B. J.; Grogan, J. M.; Ross, F. M.; Bau, H. H. Electron-Water Interactions and Implications for Liquid Cell Electron Microscopy. *J. Phys. Chem. C* **2014**, *118*, 22373–22382.

(133) Grogan, J. M.; Schneider, N. M.; Ross, F. M.; Bau, H. H. Bubble and Pattern Formation in Liquid Induced by an Electron Beam. *Nano Lett.* **2014**, *14*, 359–364.

(134) Smeets, P. J. M.; Cho, K. R.; Kempen, R. G. E.; Sommerdijk, N. A. J. M.; De Yoreo, J. J. Calcium Carbonate Nucleation Driven by Ion Binding in a Biomimetic Matrix Revealed by in Situ Electron Microscopy. *Nat. Mater.* **2015**, 1–6.

(135) Park, J.; Park, H.; Ercius, P.; Pegoraro, A. F.; Xu, C.; Kim, J. W.; Han, S. H.; Weitz, D. A. Direct Observation of Wet Biological Samples by Graphene Liquid Cell Transmission Electron Microscopy. *Nano Lett.* **2015**, *15*, 4737–4744.

(136) Dhami, N. K.; Reddy, M. S.; Mukherjee, M. S. Biomineralization of Calcium Carbonates and Their Engineered Applications: A Review. *Front. Microbiol.* **2013**, *4*, 1–13.

(137) Yiu, A. J.; Callaghan, D.; Sultana, R.; Bandyopadhyay, B. C. Vascular Calcification Stone Disease: A New Look towards the Mechanism. *J. Cardiovasc. Dev. Dis.* **2015**, *2*, 141–164.

(138) Fratzl, P. Biomimetic Materials Research: What Can We Really Learn from Nature's Structural Materials? *J. R. Soc. Interface* **2007**, *4*, 637–642.

(139) Rieger, J.; Thieme, J.; Schmidt, C. Study of Precipitation Reactions by X-Ray Microscopy: CaCO3 Precipitation and the Effect of Polycarboxylates. *Langmuir* **2000**, *16*, 8300–8305.

(140) Bots, P.; Benning, L. G.; Rodriguez-Blanco, J.-D.; Roncal-Herrero, T.; Shaw, S. Mechanistic Insights into the Crystallization of Amorphous Calcium Carbonate (ACC). *Cryst. Growth Des.* **2012**, *12*, 3806–3814.

(141) Dey, A; Bomans, P. H.; Muller, F. A; Will, J.; Frederik, P. M.; de With, G.; Sommerdijk, N. A. The Role of Prenucleation Clusters in Surface-Induced Calcium Phosphate Crystallization. *Nat. Mater.* **2010**, *9*, 1010–1014.

(142) Nielsen, M. H.; Aloni, S.; Yoreo, J. J. De. In Situ TEM Imaging of $CaCO_3$ Nucleation Reveals Coexistence of Direct and Indirect Pathways. *Science.* **2013**, *218*, 213–218.

(143) Gower, L. B. Biomimetic Model Systems for Investigating the Amorphous Precursor Pathway and Its Role in Biomineralization. *Chem. Rev.* **2008**, *108*, 4551–4627.

Chapter 3 3D Characterization of Human Nano-osseointegration by On-Axis Electron Tomography without the Missing Wedge

---

In Chapter 3, all experiments and data analysis were conducted by myself with aid from Dr. Kathryn Grandfield. The manuscript was initially drafted by myself, and edited by Furqan A. Shah and Dr. Anders Palmquist, and was edited to the final version by Dr. Kathryn Grandfield. This chapter has been published in ACS Biomaterials Science & Engineering, 2017, 3, pp 49-55. DOI: 10.1021/acsbiomaterials.6b00519.

ACS Biomaterials SCIENCE & ENGINEERING

Article

pubs.acs.org/journal/abseba

3D Characterization of Human Nano-osseointegration by On-Axis Electron Tomography without the Missing Wedge

Xiaoyue Wang,[†] Furqan A. Shah,[‡,§] Anders Palmquist,[‡,§] and Kathryn Grandfield*[,†]

[†]Department of Materials Science and Engineering, McMaster University, Hamilton, Ontario L8S 4L8, Canada

[‡]Department of Biomaterials, Institute of Clinical Sciences, Sahlgrenska Academy at University of Gothenburg, SE-405 30 Göteborg, Sweden

[§]BIOMATCELL VINN Excellence Center of Biomaterials and Cell Therapy, Göteborg, Sweden

Supporting Information

ABSTRACT: Three-dimensional (3D) visualization of bone-implant interfaces via electron tomography (ET) has contributed to the novel perspective of nano-osseointegration and offers evidential support for nanoscaled biomaterial surface modification. Conventional single-axis ET provides a relatively large field of view of the human bone to titanium implant interface showing bone structure arrangement near the interface. However, the "missing wedge" associated with conventional single-axis ET leads to artifacts and elongation in the reconstruction, limiting the resolution and fidelity of reconstructions, as well as the ability to extract quantitative information from nanostructured interfaces. On-axis ET, performed by 180° rotation of a needle-shaped sample, is a promising method to solve this problem. In this work, we present the first application of on-axis ET for investigation of human bone and laser-modified titanium implant interfaces without the missing wedge. This work demonstrates a near artifact-free 3D visualization of the nanotopographies of the implant surface oxide layer and bone growth into these features. Complementary electron energy-loss spectroscopy (EELS) mapping was used to illustrate the gradual intermixing of carbon and calcium (characteristic elements of bone) with the nanoscaled oxide layer of the implant surface. Ultimately, this approach serves as direct evidence of nano-osseointegration and as a potential platform to evaluate differently structured implant surfaces.

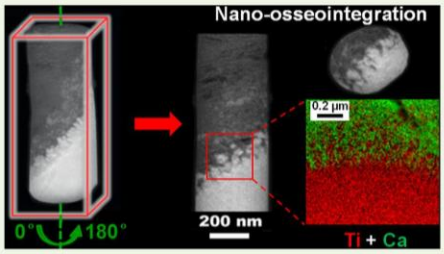

KEYWORDS: *osseointegration, electron tomography, bone, titanium, dental implant, on-axis*

INTRODUCTION

Osseointegration, classically defined as "a direct structural and functional connection between ordered living bone and the surface of a load-carrying implant", plays a crucial role in the success of reconstructive and regenerative interventions in orthopedics, dentistry, and bone-anchored hearing or prosthetic devices.[1−4] A complete characterization and understanding of the interface between human bone and implant offers valuable insight into the mechanisms of osseointegration in order to optimize implant surface modification.[5] From simple histological observations made with the aid of the light microscope, the analytical techniques used for evaluating osseointegration now regularly include micron-scale resolved scanning electron microscopy (SEM), and nanoscale investigation by transmission electron microscopy (TEM).[4,6−8] With breakthroughs in ultrastructural characterization of the bone-implant interface, the definition of osseointegration has also evolved from the original clinically oriented perspective to a comprehensive multiscale structural[9] and functionally graded tissue integration.[10] Besides the advancement in spatial resolution afforded by advanced imaging techniques, interface characterization has also progressed from two-dimensional (2D) to three-dimensional (3D) analyses with, for example, X-ray microcomputed tomography (micro-CT),[11,12] serial surface visualization (SSV) with focused ion beam (FIB),[13] and transmission electron tomography (ET).[14] Among them, of great interest is ET using scanning transmission electron microscopy (STEM) in high-angle annular dark-field (HAADF) mode, because it provides not only superior nanoscale resolution to X-ray-based analyses, but also compositional contrast sensitive enough to discern bone from the implant, and ultrastructural features within the bone itself. Many interesting results have been reported with this method, including the orientation of bone apatite adjacent to synthetic hydroxyapatite scaffolds, collagen fiber alignment, and the interdigitation of bone with nanostructured implant features.[10,14−16] However, because of the shadowing effects introduced by the increased thickness of conventional TEM lamellae at high tilt angles[17] and the limited tilt-range of TEM holders, the "missing wedge", the geometric region of unsampled projection data in Fourier space, cannot be avoided,[14] which leads to artifacts and elongation in the

Received: September 7, 2016
Accepted: November 16, 2016
Published: November 16, 2016

DOI: 10.1021/acsbiomaterials.6b00519
ACS Biomater. Sci. Eng. 2017, 3, 49−55

direction of the missing wedge so as to limit the resolution in the final reconstruction.[18]

One widely reported solution to this problem is dual-axis ET, in which a second tilt-axis perpendicular to the original one is employed.[19−21] Although the so-called missing pyramid left by this method is considerably reduced compared with the original missing wedge in single-axis ET, it is not the most optimum or practical solution considering that it fails to eliminate the missing wedge completely and needs additional experimental protocols including increased acquisition time. Most biological samples are sensitive to electron beam exposure. A promising alternative method to solve the missing wedge problem and to acquire high-fidelity 3D reconstructions for significantly improved quantitative analysis of nano-osseointegration is on-axis electron tomography, whereby a needle-shaped sample is rotated through an angular range of 180°.[22−25] Highlighted in Figure 1, the difference between conventional single-axis

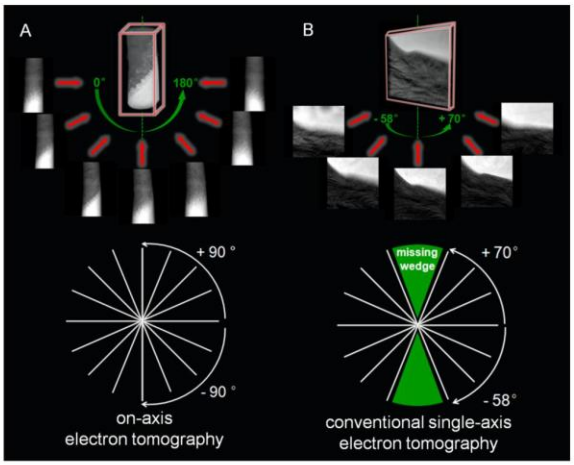

Figure 1. Schematic representation of the differences between specimen geometry and acquisition approaches for (a) on-axis electron tomography, and (b) conventional electron tomography. Due to the limited tilt-range in conventional single-axis tomography of a lamellar sample, some angles are inaccessible, and a missing wedge of data results in Fourier space. The on-axis holder allows complete rotation of a cylindrical specimen, and therefore no missing angles or missing wedge artifacts arise.

electron tomography of a lamellar sample and on-axis tomography of a cylindrical sample is illustrated. The on-axis sample can rotate completely within the TEM, meaning that no angular range is left unsampled and therefore no missing wedge is present unlike single-axis electron tomography. Furthermore, the needle-shaped sample geometry also provides the possibilities to correlate electron tomography with spectral information acquired by electron energy loss spectroscopy (EELS) because the specimen thickness remains constant at high tilt angles, or with atom probe tomography, which utilizes a similarly sharpened sample.

In this paper, we demonstrate the novel use of on-axis ET to investigate the human bone and laser-modified titanium implant interface on nanoscale without the missing wedge. A needle-shaped sample prepared by FIB of diameter 200 nm is employed together with an on-axis 360° rotation tomography holder. In addition, conventional single-axis ET of a lamellar TEM sample obtained from the same specimen is presented for comparison along with spectral analysis demonstrating nano-osseointegration.

■ EXPERIMENTAL METHODS

Implant and Patient Data. The specimen used in this study was a clinically retrieved failed dental implant from a 66-year-old female patient. Research was conducted under ethical approval for Biobank 513 at the University of Gothenburg and from the Human Integrated Research Ethics Board at McMaster University. This screw-shaped commercially pure titanium dental implant (BioHelix, Brånemark Integration AB, Mölndal, Sweden) was partly laser-modified in the thread valleys resulting in a nanostructured titanium dioxide surface layer on the order of a few hundred nanometers. After retrieval with a surrounding collar of bone, the specimen was fixed in formalin, dehydrated in a graded series of ethanol, embedded in plastic resin (LR White, London Resin Company, UK) and bisected longitudinally for further study. Further details on the implant material, preparation for microscopy and histology and histomorphometry study on this specimen can be found elsewhere.[11]

Sample Preparation with Focused Ion Beam. ET samples were prepared using in situ lift-out protocols in a dual-beam FIB system (Zeiss NVision 40, Carl Zeiss AG). After the intact bone-implant interface was selected, ion beam deposited tungsten (10 μm × 3 μm × 0.5 μm) was laid down to protect the region of interest. For conventional single-axis ET, a wedge-shaped sample was lifted out after rough milling of trenches and was attached to a FIB-TEM grid for further thinning to electron transparency. The resulting specimen was rectangular (lamellar) in shape with approximate dimensions of 10 μm × 5 μm × 200 nm. For on-axis ET, a needle-shaped pillar (containing both the bone tissue at one end and titanium of the implant at the opposite end) was prepared according to a protocol described in detail previously.[26] A region of interest within the sample was lifted out and the titanium end was attached to the top of the copper tomography post. The modified stub was then tilted 90° in order to orient the sample post with attached specimen vertically. A thin layer of tungsten was deposited to protect the top bone surface, and the sample was annularly milled into a needle shape with a final diameter of approximately 200 nm using a 30 kV ion beam at successively lower ion beam currents (150−10 pA). In order to minimize surface damage and Ga ion implantation, the needle-shaped sample was further subjected to low keV beam polishing (10 kV, 80 pA). It is important to note that due to the nature of this technique and the requirement for extremely thin (100−200 nm) specimens, this imaging approach cannot be applied to living organisms or tissues, they must first be fixed and embedded in resin for electron microscopy. For more information on focused ion beam as a preparation tool for transmission electron microscopy of samples, please refer to more detailed works.[27]

Electron Tomography. A Titan 80−300 STEM (FEI Company, The Netherlands) operated at 300 kV with convergence angle of 8 mrad was employed to acquire HAADF images via FEI's Explore 3D (FEI Company, The Netherlands) software package for tomography. The conventional single-axis ET, the lamellar sample was mounted on the single-tilt tomography holder, and a tilt-series from −58° to +70° was acquired with images recorded every 2°. The needle-shaped sample was mounted in a model 2050 on-axis rotation tomography holder (E.A. Fischione Instruments, Inc., Export, PA) and tilted through ±90° also with an angular step size of 2°. The acquired projections were aligned via cross-correlation after low-pass filtering and then reconstructed with a simultaneous iterative reconstruction method (SIRT) with 25 iterations in the Inspect 3D software (FEI Company, The Netherlands). The software Amira (FEI Company, The Netherlands) completed the visualization of reconstructed volumes via volume rendering and orthoslices.

Chemical Analysis. The STEM EELS spectral images and dark-field images of the lamellar sample were recorded on a FEI Titan 80−300 microscope (FEI Company, The Netherlands), operated at 300 kV. The microscope is equipped with a CEOS probe and image corrector (CEOS GmbH, Heidelberg, Germany), and a Gatan GIF

DOI: 10.1021/acsbiomaterials.6b00519
ACS Biomater. Sci. Eng. 2017, 3, 49−55

Quantum energy filter (Gatan Inc., Pleasanton, CA). Chemical distribution maps were obtained for elements calcium, carbon, oxygen and titanium from the EELS spectral images using a power-law background model.

RESULTS AND DISCUSSION

Osseointegration of titanium and other implant devices has been studied extensively by a variety of techniques, including histology, scanning electron microscopy, transmission electron microscopy, electron tomography, and more recently, atom probe tomography.[9,28−30] Each of these presents advantages and disadvantages.

Using conventional single-axis electron tomography techniques, 2D HAADF-STEM images (Figure 2a) and corresponding 3D reconstructions (Figure 2b) of the lamellar sample by conventional single-axis ET of human bone and implant interface provide a relatively large field of view (several micrometers). The bone−implant interfacial contact zone is characterized by an intimate connection of bone to the surface oxide layer, and the characteristic collagen banding in the bone structure perpendicular to the implant surface. Consistent with previous studies, the orientation of groups of mineralized collagen fibrils at the interface appears to be parallel to the implant surface.[10,16] The nanotexture of the 100 nm thick oxide layer is clearly revealed in 3D. However, bone ingrowth into this oxide layer is difficult to decipher perhaps due to the missing wedge artifact that leads to a loss of resolution of the 3D reconstruction. A video clip showing the 3D reconstructed volume obtained by conventional single-axis ET is available (Video S1).

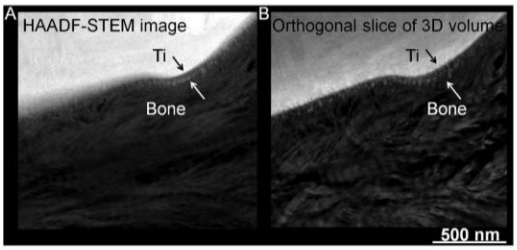

Figure 2. (a) 2D HAADF-STEM image of a lamellar sample of the human bone-implant interface. (b) Orthogonal slice through the thickness of the reconstructed 3D volume after single-axis ET clearly showing the collagen banding pattern, indicating collagen arrangement parallel the implant surface over a large field of view. Arrows indicate the bone−implant interface. A video clip showing the 3D reconstructed volume obtained by conventional single-axis ET is available (Video S1).

To improve the resolution and generate a more accurate representation of the bone interface to the implant surface oxide, on-axis electron tomography of a needle-shaped specimen was performed. On-axis electron tomography has the advantage of both a complete tilt range without the missing wedge, and constant image intensity. A comparison of the mean image intensity with tilt angle is shown (Figure 3) for both on-axis tomography and single-axis tomography of a lamellar sample.[22] In conventional tomography, the thickness of a lamellar sample increases with increasing tilt-angle, and so does the image intensity due to the mass−thickness contrast mechanism in HAADF-STEM. In very thick specimens, this may disrupt the projection condition that all projections are a monotonic function of intensity. By contrast, the constant thickness of a cylindrical specimen in on-axis tomography results in constant image intensity, which contributes to the quality of the 3D reconstruction.

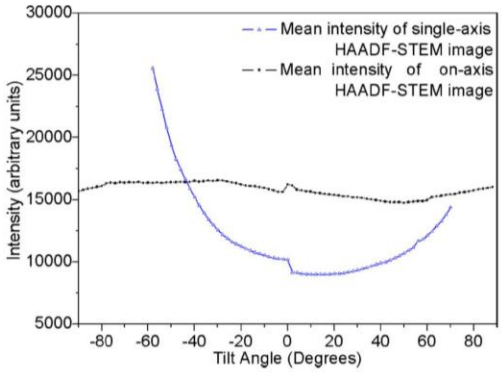

Figure 3. Graphical representation of the mean intensity of HAADF-STEM images with tilt-angles for conventional single-axis and on-axis ET. The thickness variation with increasing tilt angles in conventional single-axis ET causes a large variation in image intensity that results in distorted features, and also interferes with reconstruction algorithms. Conversely, on-axis ET shows constant image intensity.

In a HAADF-STEM image of the needle-shaped specimen (Figure 4a), the nanofeatures of the oxide layer are indiscernible, and appear continuous and blurry due to information overlap along the *Z*-axis, i.e., through the thickness of the specimen. However, 3D reconstructions of on-axis ET of the interface by gray scale 3D volume rendering (Figure 4b), and by orthoslices—virtual sections through the thickness of the reconstructed volume (Figure 4c−g) offer a more detailed visualization of the nanotopography of the implant surface. Here, we can easily identify the circular shaped nanoscale

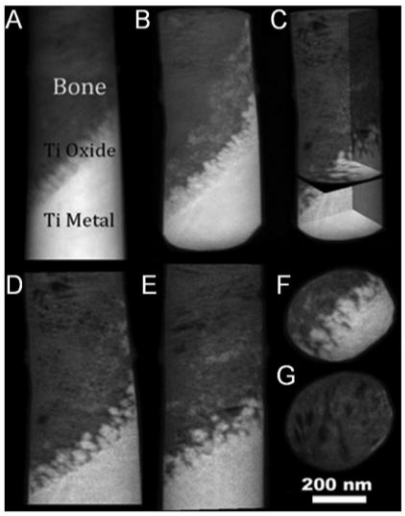

Figure 4. (a) HAADF-STEM image of a needle-shaped bone-implant interface sample. (b) 3D reconstruction of the bone-implant interface after on-axis ET, shown here in gray scale. (c−g). Orthoslices through the reconstructed volume showing the fine-scaled features of the oxide surface and intervening bone tissue, taken at (c) orthogonal directions, (d) planes XY, (e) YZ, and (f, g) XZ. A video clip showing the 3D reconstructed volume obtained by on-axis ET is available (Video S2).

DOI: 10.1021/acsbiomaterials.6b00519
ACS Biomater. Sci. Eng. 2017, 3, 49−55

features that make up the titanium oxide modified surface. Bone ingrowth into this nanoscaled rough oxide layer and an intact nanoscale interface can also be appreciated. From the orthogonal slices of the 3D volume (Figure 4c–g), the features in the bone and at the interface are free from elongations along the *Z*-axis caused by the missing wedge. A video clip showing the 3D reconstructed volume obtained by on-axis ET is available (Video S2).

This clearly demonstrates that the nanoscale features of the implant are contributing to the osseointegration of the material. Nanoscale phenomena in other biomineralization scenarios have been reported previously with advanced electron microscopy techniques. Recent studies focusing on in vitro investigations of biomineralization have contributed to interesting findings related specifically to mineral in bone formation. For example, the role of collagen as a template for the growth of amorphous calcium phosphate has been demonstrated with cryogenic transmission electron microscopy and conventional cryogenic electron tomography, i.e., not on-axis tomography.[31] This study has provided a useful basis for visualizing bone-like mineral integration into collagen fibrils in vitro. Other works have attempted to replicate the cellular process of bone mineral formation using mouse osteoblast cells and techniques such as TEM and electron tomography.[32] While making important contributions to the process of mineral formation and certainly technically challenging to carry out, in many ways these investigations that focus on in vitro collagen, or single cell cultures, are much simpler than analyzing the in vivo bone growth scenario, which is complicated by the sheer complexity of bone tissue itself.

Even tomography techniques, which are widely used to assess biomineralization[31] and bone growth,[9,10,33] present artifacts due to the missing wedge. To demonstrate the effect of the missing wedge, we computed a reconstructed slice through the same on-axis data set using varying angular ranges from ±90° to ±40° (Figure 5). It was observed that as the angular range of a given tilt series decreases from ±90°, there is an obvious elongation in the direction of the *Z*-axis so as to make the circular cross-section of the sample appear more ovoid and grossly distorted (Figure 5a–c). This type of artifact can also

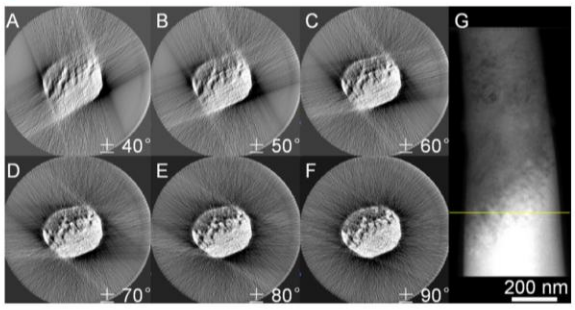

Figure 5. Effect of the missing wedge is demonstrated through this series of XZ cross-sections through a single reconstructed slice (denoted by the yellow horizontal line in g) as reconstructed with (a–f) various maximum tilt ranges from ±40° to ±90°, showing the effect of the missing wedge. Artifacts such as elongation are quite clearly seen at (a–c) smaller tilt ranges, whereas (d–f) larger tilt ranges show a more accurate representation of the exterior shape of the sample allowing for the visualization of the oxide layer and bone growth, which is almost indiscernible at smaller tilt ranges.

contribute to the loss of quality of the 3D reconstruction so that features in the specimen become blurry and may even disappear completely. For example, for a tilt series with a maximum angular range of ±40° (Figure 5a), demarcating the border between bone and implant is difficult, and the oxide layer cannot be resolved clearly. Therefore, on-axis electron tomography using a complete ±90° data set (Figure 5f) contributes greatly to improving the fidelity of 3D reconstruction of the bone-implant interface, offering an accurate understanding and a clearer picture of nano-osseointegration. However, one major limitation of using needle-shaped samples is their small size, thereby restricting the visualization of bone microstructure and organization to only a small region near the interface. Therefore, conventional single-axis ET and on-axis ET techniques may be applied in a complementary manner to investigate materials exhibiting a heterogeneous and/or a hierarchical architecture.

There are some fundamental distinctions between this tomography technique and, the perhaps more familiar, microcomputed tomography (micro-CT). Although both are tomographic in nature, meaning that a 3D representation of the structure of interest can be created, their imaging source, i.e., X-rays or electrons, results in vastly different resolving capabilities. For example, typical laboratory-based X-ray micro-CT instruments can reach a resolution around 1–1.5 μm. In contrast, electron tomography provides a resolution down to the nanometer level. Moreover, micro-CT investigations of bone-implant interfaces result in beam hardening artifacts that obscure visualization of the first few micrometers from the bone-implant interface. Therefore, micro-CT is capable of large-scale measurements of bone-implant contact similar to histomorphometry,[34] but it cannot resolve the details we observe within this study, including collagen fibrils, that are on the nanoscale. Furthermore, micro-CT provides no reliable information on the composition of bone, whereas HAADF imaging is inherently based on compositional contrast. Furthermore, TEM in general couples imaging and a variety of spectroscopic techniques to simultaneously probe composition.

For example, although nano-osseointegration is qualitatively deduced from the structural representation of bone growth into the oxide from on-axis ET, chemical analysis, such as by EELS spectral imaging for elemental distributions at the bone-implant interface can provide correlative quantitative information (Figure 6). The respective elemental maps of C, O, Ti and Ca in the region of interest are shown (Figure 6a, b). An overlap of C and Ca with O and Ti of the oxide layer, as well as fingers of Ca and C (representative of bone) reaching into the nanoscale "channels" of the surface oxide can be appreciated (Figure 6c–e), which supports the existence of nano-osseointegration from the perspective of chemical analysis. Although the elemental maps of Ca indicate that the bone mineral integrates into the titanium oxide interface, the origin of Ca from different biominerals requires higher energy resolution to discriminate EELS near-edge structures, as shown by Klosowski et al.[35] Further investigation on the fine structure of EELS data at interfaces with higher energy resolution, as well as incorporating chemical analysis into a three-dimensional structural reconstruction to enable a 4D tomography approach (where the fourth dimension after spatial coordinates is the chemical composition) is needed. Using a needle-shaped specimen, as reported herein, makes this simultaneous structural and chemical analysis possible in the

DOI: 10.1021/acsbiomaterials.6b00519
ACS Biomater. Sci. Eng. 2017, 3, 49–55

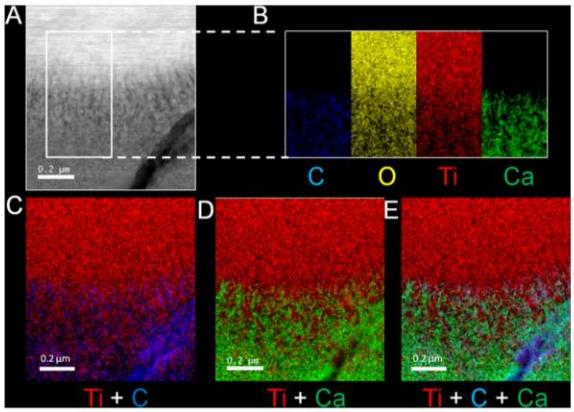

Figure 6. EELS elemental distribution maps of the human bone-implant interface. (a) Corresponding HAADF image (with rectangular region of interest marked). (b) Elemental distributions of C, O, Ti, Ca corresponding to (a). (c–e) RBG color maps of (c) Ti and C, (d) Ti and Ca, and (e) Ti and C and Ca clearly show the interdigitation of Ca and C (representative of bone) within the nanostructured oxide layer.

future due to the constant sample thickness over all tilt ranges, unlike lamellar samples whose thickness increases with increasing tilt angle, reducing the intensity of the EELS signal detected.[36]

The gold standard in assessing bone integration of implant devices has been backscattered electron scanning electron microscopy and histological studies.[10] Although these techniques have certain advantages, particularly the ability to stain for specific biological features in the case of histology, neither is capable of probing the interaction of nanoscale features with bone. Used in combination with these traditional analyses, on-axis electron tomography can provide the advantage of a clear visualization of the role of the implant surface features on bone integration. With increasing interest in the nanofunctionalization of implant surfaces, and the demonstrated role of nanotopography on bone cell and tissue response,[37,38] the use of on-axis electron tomography provides a suitable approaches to evaluate the effectiveness of these devices. Furthermore, the technique can certainly be applied to other biological interfaces of interest, including soft or connective tissues, and other tissue engineering constructs. Using similar preparation methods by focused ion beam, and incorporating appropriate staining methods all biological matter that can be analyzed by TEM, could in theory be investigated by on-axis electron tomography. Established methods for staining, reducing beam dose and perform cryo- electron tomography of soft materials are widespread.[39] In particular, for the evaluation and accurate quantification of porosity in nano- or mesoporous scaffolds or biomaterials, on-axis ET could be particularly well-suited, as demonstrated for quantitative pore analysis in nonbiological materials.[25] The technique could also be extended to the investigation of mineralized tissues themselves. For example, a recent study investigating bone ultrastructure and mechanical properties used pillar-like specimens, some of which were on the range of 250 nm and could be correlatively investigated by on-axis electron tomography to fully understand the link between nano- or ultrastructure of bone and its mechanical properties.[40] Therefore, the possibilities for expansion of this technique in biomaterials research are yet to be fully realized.

■ CONCLUSIONS

In this work, the application of conventional single-axis ET (using lamellar samples) and on-axis ET (using needle-shaped samples) of the human bone-titanium implant interface has been presented. Although both techniques allow direct visualization of the oxide layer on the implant surface and bone growth in the immediate vicinity, the lamellar samples allowed a larger field of view of the interface, which showed the structural arrangement of bone both near to and distant from the implant surface, albeit with the missing wedge being a major drawback of the technique. On the other hand, on-axis ET offered a more detailed visualization of the 3D volume of the oxide structure and intervening bone in high fidelity due to the tilt-series spanning the entire ±90° angular range, without introducing the missing wedge artifact. Therefore, although on-axis tomography provides near artifact-free 3D reconstruction, both ET techniques reveal useful and complementary information about the bone-implant interfaces. Moreover, revealed via EELS mapping, the presence of C and Ca within the nanoscaled oxide layer provides direct evidence in favor of nano-osseointegration from the perspective of elemental distribution. More work is clearly needed to understand from which bone mineral phase the calcium signal originates. Therefore, on-axis ET is a promising method to correlate 3D structure with the chemical composition in the future (e.g., combined with EELS[36] or atom probe tomography) because of the needle-shaped sample geometry. Ultimately, this method of characterization provides an approach to visualizing bone ingrowth into nanoscale features. This serves as a technological platform for investigating the influence of differently manufactured nanosurfaces on bone attachment mechanisms.

■ ASSOCIATED CONTENT

Supporting Information

The Supporting Information is available free of charge on the ACS Publications website at DOI: 10.1021/acsbiomaterials.6b00519.

Video S1, film clip of the 3D reconstructed volume obtained by conventional single-axis ET (MPG)

Video S2, film clip showing the 3D reconstructed volume obtained by on-axis ET (MPG)

■ AUTHOR INFORMATION

Corresponding Author

*E-mail: kgrandfield@mcmaster.ca.

ORCID

Kathryn Grandfield: 0000-0002-0188-9580

Author Contributions

Experiments were conducted by X.W., K.G., and A.P. Data analysis was performed by X.W. The manuscript was written by X.W. and F.A.S. and edited by all authors. All authors have given approval to the final version of the manuscript.

Funding

This work was supported by the Natural Sciences and Engineering Research Council of Canada (NSERC) Discovery Grant program. X.W. acknowledges support from the Ontario Trillium Scholarship. Financial support from the Swedish Research Council, the BIOMATCELL VINN Excellence Center of Biomaterials and Cell Therapy, the Region Västra Götaland, ALF/LUA grant, the Inga Britt and Arne Lundberg Foundation and the Hjalmar Svensson Foundation is acknowl-

DOI: 10.1021/acsbiomaterials.6b00519
ACS Biomater. Sci. Eng. 2017, 3, 49–55

edged. F.A.S. holds a PhD position financed by the Swedish Government Strategic Funding of Materials Science Area of Advance, provided to Chalmers and Department of Biomaterials, University of Gothenburg.

Notes

The authors declare no competing financial interest.

■ ACKNOWLEDGMENTS

Electron microscopy was performed at the Canadian Centre for Electron Microscopy at McMaster University, a facility supported by NSERC and other governmental agencies.

■ REFERENCES

(1) Brånemark, P. I.; Breine, U.; Adell, R.; Hansson, B. O.; Lindström, J.; Ohlsson, A. Intra-Osseous Anchorage of Dental Prostheses. I. Experimental Studies. *Scand. J. Plast. Reconstr. Surg.* **1969**, *3*, 81−100.

(2) Brånemark, R.; Brånemark, P. I.; Rydevik, B.; Myers, R. R. Osseointegration in Skeletal Reconstruction and Rehabilitation: A Review. *J. Rehabil. Res. Dev.* **2001**, *38*, 175−181.

(3) Shah, F. A.; Johansson, M. L.; Omar, O.; Simonsson, H.; Palmquist, A.; Thomsen, P. Laser-Modified Surface Enhances Osseointegration and Biomechanical Anchorage of Commercially Pure Titanium Implants for Bone-Anchored Hearing Systems. *PLoS One* **2016**, *11*, e0157504.

(4) Palmquist, A.; Jarmar, T.; Emanuelsson, L.; Brånemark, R.; Engqvist, H.; Thomsen, P. Forearm Bone-Anchored Amputation Prosthesis. *Acta Orthop.* **2008**, *79* (1), 78−85.

(5) Mavrogenis, A. F.; Dimitriou, R.; Parvizi, J.; Babis, G. C. Biology of Implant Osseointegration. *J. Musculoskelet. Neuronal Interact.* **2009**, *9*, 61−71.

(6) Jarmar, T.; Palmquist, A.; Brånemark, R.; Hermansson, L.; Engqvist, H.; Thomsen, P. Characterization of the Surface Properties of Commercially Available Dental Implants Using Scanning Electron Microscopy, Focused Ion Beam, and High-Resolution Transmission Electron Microscopy. *Clin. Implant Dent. Relat. Res.* **2008**, *10*, 11−22.

(7) Palmquist, A.; Lindberg, F.; Emanuelsson, L.; Brånemark, R.; Engqvist, H.; Thomsen, P. Biomechanical, histological, and Ultrastructural Analyses of Laser Micro- and Nano-Structured Titanium Alloy Implants: A Study in Rabbit. *J. Biomed. Mater. Res., Part A* **2010**, *92* (4), 1476−1485.

(8) Grandfield, K. Bone, Implants, and Their Interfaces. *Phys. Today* **2015**, *68*, 40−45.

(9) Shah, F. A.; Wang, X.; Thomsen, P.; Grandfield, K.; Palmquist, A. High-Resolution Visualization of the Osteocyte Lacuno-Canalicular Network Juxtaposed to the Surface of Nanotextured Titanium Implants in Human. *ACS Biomater. Sci. Eng.* **2015**, *1*, 305−313.

(10) Grandfield, K.; Gustafsson, S.; Palmquist, A. Where Bone Meets Implant: The Characterization of Nano-Osseointegration. *Nanoscale* **2013**, *5*, 4302−4308.

(11) Shah, F. A.; Nilson, B.; Brånemark, R.; Thomsen, P.; Palmquist, A. The Bone-Implant Interface-Nanoscale Analysis of Clinically Retrieved Dental Implants. *Nanomedicine* **2014**, *10*, 1729−1737.

(12) Swain, M. V.; Xue, J. State of the Art of Micro-CT Applications in Dental Research. *Int. J. Oral Sci.* **2009**, *1*, 177−188.

(13) Giannuzzi, L. A.; Phifer, D.; Giannuzzi, N. J.; Capuano, M. J. Two-Dimensional and 3-Dimensional Analysis of Bone/Dental Implant Interfaces With the Use of Focused Ion Beam and Electron Microscopy. *J. Oral Maxillofac. Surg.* **2007**, *65*, 737−747.

(14) Grandfield, K.; Palmquist, A.; Engqvist, H. High-Resolution Three-Dimensional Probes of Biomaterials and Their Interfaces. *Philos. Trans. R. Soc., A* **2012**, *370*, 1337−1351.

(15) Grandfield, K.; McNally, E. A.; Palmquist, A.; Botton, G. A.; Thomsen, P.; Engqvist, H. Visualizing Biointerfaces in Three Dimensions: Electron Tomography of the Bone-Hydroxyapatite Interface. *J. R. Soc., Interface* **2010**, *7*, 1497−1501.

(16) Grandfield, K.; Palmquist, A.; Engqvist, H. Three-Dimensional Structure of Laser-Modified Ti6Al4V and Bone Interface Revealed with STEM Tomography. *Ultramicroscopy* **2013**, *127*, 48−52.

(17) Kaneko, T.; Nishioka, H.; Nishi, T.; Jinnai, H. Reduction of Anisotropic Image Resolution in Transmission Electron Microtomography by Use of Quadrangular Prism-Shaped Section. *J. Electron Microsc.* **2005**, *54*, 437−444.

(18) Midgley, P. A.; Dunin-Borkowski, R. E. Electron Tomography and Holography in Materials Science. *Nat. Mater.* **2009**, *8*, 271−280.

(19) Penczek, P.; Marko, M.; Buttle, K.; Frank, J. Double-Tilt Electron Tomography. *Ultramicroscopy* **1995**, *60*, 393−410.

(20) Mastronarde, D. N. Dual-Axis Tomography: An Approach with Alignment Methods That Preserve Resolution. *J. Struct. Biol.* **1997**, *120*, 343−352.

(21) Sugimori, H.; Nishi, T.; Jinnai, H. Dual-Axis Electron Tomography for Three-Dimensional Observations of Polymeric Nanostructures. *Macromolecules* **2005**, *38*, 10226−10233.

(22) Kawase, N.; Kato, M.; Nishioka, H.; Jinnai, H. Transmission Electron Microtomography without the "Missing Wedge" for Quantitative Structural Analysis. *Ultramicroscopy* **2007**, *107*, 8−15.

(23) Yaguchi, T.; Konno, M.; Kamino, T.; Watanabe, M. Observation of Three-Dimensional Elemental Distributions of a Si Device Using a 360°-Tilt FIB and the Cold Field-Emission STEM System. *Ultramicroscopy* **2008**, *108*, 1603−1615.

(24) Ke, X.; Bals, S.; Cott, D.; Hantschel, T.; Bender, H.; Van Tendeloo, G. Three-Dimensional Analysis of Carbon Nanotube Networks in Interconnects by Electron Tomography without Missing Wedge Artifacts. *Microsc. Microanal.* **2010**, *16*, 210−217.

(25) Biermans, E.; Molina, L.; Batenburg, K. J.; Bals, S.; Van Tendeloo, G. Measuring Porosity at the Nanoscale by Quantitative Electron Tomography. *Nano Lett.* **2010**, *10*, 5014−5019.

(26) Huang, J.; Wang, X.; Grandfield, K. FIB Preparation of Bone-Implant Interfaces for Correlative On-Axis Rotation Electron Tomography and Atom Probe Tomography. *Microsc. Microanal.* **2014**, *20*, 352−353.

(27) Grandfield, K.; Engqvist, H. Focused Ion Beam in the Study of Biomaterials and Biological Matter. *Adv. Mater. Sci. Eng.* **2012**, *2012*, 841961.

(28) Thorfve, A.; Palmquist, A.; Grandfield, K. Three-Dimensional Analytical Techniques for Evaluation of Osseointegrated Titanium Implants. *Mater. Sci. Technol.* **2015**, *31*, 174−179.

(29) Porter, A. E.; Patel, N.; Skepper, J. N.; Best, S. M.; Bonfield, W. Effect of Sintered Silicate-Substituted Hydroxyapatite on Remodelling Processes at the Bone-Implant Interface. *Biomaterials* **2004**, *25*, 3303−3314.

(30) Karlsson, J.; Sundell, G.; Thuvander, M.; Andersson, M. Atomically Resolved Tissue Integration. *Nano Lett.* **2014**, *14*, 4220−4223.

(31) Nudelman, F.; Pieterse, K.; George, A.; Bomans, P. H. H.; Friedrich, H.; Brylka, L. J.; Hilbers, P. A.; de With, G.; Sommerdijk, N. a. J. M. The Role of Collagen in Bone Apatite Formation in the Presence of Hydroxyapatite Nucleation Inhibitors. *Nat. Mater.* **2010**, *9*, 1004−1009.

(32) Boonrungsiman, S.; Gentleman, E.; Carzaniga, R.; Evans, N. D.; McComb, D. W.; Porter, A. E.; Stevens, M. M. The Role of Intracellular Calcium Phosphate in Osteoblast-Mediated Bone Apatite Formation. *Proc. Natl. Acad. Sci. U. S. A.* **2012**, *109*, 14170−14175.

(33) Palmquist, A.; Grandfield, K.; Norlindh, B.; Mattsson, T.; Brånemark, R.; Thomsen, P. Bone-Titanium Oxide Interface in Humans Revealed by Transmission Electron Microscopy and Electron Tomography. *J. R. Soc., Interface* **2012**, *9*, 396−400.

(34) Rebaudi, A.; Koller, B.; Laib, A.; Trisi, P. Microcomputed Tomographic Analysis of the Peri-Implant Bone. *Int. J. Periodontics Restorative Dent.* **2004**, *24*, 316−325.

(35) Klosowski, M. M.; Friederichs, R. J.; Nichol, R.; Antolin, N.; Carzaniga, R.; Windl, W.; Best, S. M.; Shefelbine, S. J.; McComb, D. W.; Porter, A. E. Probing Carbonate in Bone Forming Minerals on the Nanometre Scale. *Acta Biomater.* **2015**, *20*, 129−139.

DOI: 10.1021/acsbiomaterials.6b00519
ACS Biomater. Sci. Eng. 2017, 3, 49−55

(36) Jarausch, K.; Thomas, P.; Leonard, D. N.; Twesten, R.; Booth, C. R. Four-Dimensional STEM-EELS: Enabling Nano-Scale Chemical Tomography. *Ultramicroscopy* **2009**, *109*, 326−337.
(37) Brånemark, R.; Emanuelsson, L.; Palmquist, A.; Thomsen, P. Bone Response to Laser-Induced Micro- and Nano-Size Titanium Surface Features. *Nanomedicine* **2011**, *7*, 220−227.
(38) Ajami, E.; Bell, S.; Liddell, R. S.; Davies, J. E. Early Bone Anchorage to Micro- and Nano-Topographically Complex Implant Surfaces in Hyperglycemia. *Acta Biomater.* **2016**, *39*, 169−179.
(39) Ercius, P.; Alaidi, O.; Rames, M. J.; Ren, G. Electron Tomography: A Three-Dimensional Analytic Tool for Hard and Soft Materials Research. *Adv. Mater.* **2015**, *27*, 5638−5663.
(40) Tertuliano, O. A.; Greer, J. R. The Nanocomposite Nature of Bone Drives Its Strength and Damage Resistance. *Nat. Mater.* **2016**, *15*, 1195−1202.

DOI: 10.1021/acsbiomaterials.6b00519
ACS Biomater. Sci. Eng. 2017, 3, 49−55

Chapter 4 Biomineralization at Titanium Revealed by Correlative 4D Tomographic and Spectroscopic Methods

---

In Chapter 4, the project design was performed by myself with consultation from Dr. Kathryn Grandfield. Electron tomography experiments were conducted by myself. Dr. Andreas Korinek provided assistance with EELS tomography data collection. Dr. Matthieu Bugnet aided with ELNES data collection. Dr. Brian Langelier performed APT experiments and Dr. Adam Hitchcock performed STXM-XAS experiments. All data were analyzed by myself with much useful discussion with Dr. Matthieu Bugnet, Dr. Brian Langelier and Dr. Adam Hitchcock. This manuscript was written by myself and edited by Dr. Kathryn Grandfield, Furqan A. Shah and Dr. Anders Palmquist. The final revisions and proofreading were kindly provided by all authors. This manuscript version of chapter has been submitted for publication in 2018.

Biomineralization at Titanium Revealed by Correlative 4D Tomographic and Spectroscopic Methods

Xiaoyue Wang[1], Brian Langelier[2], Furqan A. Shah[3], Andreas Korinek[2], Matthieu Bugnet[4], Adam P. Hitchcock[5], Anders Palmquist[3], Kathryn Grandfield[1,6*]

[1.] Department of Materials Science and Engineering, McMaster University, Hamilton, L8S 4L7 Canada.
[2.] Canadian Centre for Electron Microscopy, McMaster University, Hamilton, L8S 4L7 Canada.
[3.] Department of Biomaterials, Sahlgrenska Academy at University of Gothenburg, Göteborg, 405 30 Sweden.
[4.] University of Lyon, INSA Lyon, UCBL Lyon 1, MATEIS, UMR 5510 CNRS, 69621Villeurbanne Cedex, France.
[5.] Department of Chemistry and Chemical Biology, McMaster University, Hamilton, L8S 4M1Canada.
[6.] School of Biomedical Engineering, McMaster University, Hamilton, L8S 4L7 Canada.

4.1 Abstract

Biominerals often have intricate hierarchical structures linked to the physiological functions of living organisms. Calcium phosphate (CaP), a typical example, is a building block of the bones and teeth of vertebrates. The biomineralization of CaP at biomaterials interfaces plays a key role in the interlocking of living bone with dental or orthopaedic implants. However, the exact bonding mechanism between bone and implants is still unclear. The distribution of both the mineralized and organic components of bone at the interface, and their origins, requires improved characterization. Here, we report the first correlative application of on-axis electron tomography, electron energy-loss spectroscopy (EELS) tomography, and atom probe tomography (APT), as well as spectroscopy techniques to probe the nanoscale chemical structure of the biointerface between human bone and commercial titanium dental implant in four dimensions (4D). The correlative 4D tomography workflow established is transferable to other applications in materials or biological sciences.

4.2 Introduction

Biominerals are abundant natural materials formed from the interaction of organic and inorganic components mediated by living organisms.[1] Their intricate hierarchical structure and distinctive mechanical properties have attracted interest to unveil their formation mechanisms, as these mechanisms could form the basis for model systems for

the design and synthesis of biomimetic materials.[2] Calcium phosphates (CaP) are one of the most highly researched classes of biominerals since the carbonated apatite crystal is the building block of both bones and teeth of vertebrates, and consequently, they have extensive biomedical applications.[3] The mechanism of CaP mineralization in bone is not fully understood. A transient phase of amorphous calcium phosphate (ACP),[4] and the mediating roles of collagen[5] and non-collagenous proteins[6] have been reported from both *in vivo* and *in vitro* studies. Bone regeneration and remodeling play a key role in the maintenance of healthy bone quality, for example in repairing naturally occurring microfractures, maintaining ionic balance, and enabling the interlocking of living bone tissue to artificially synthesized biomaterial surfaces, i.e. in the case of dental or orthopaedic implants. Every year, millions of dental implants, hip and knee replacements, prosthesis, and even 3D-printed customized bone implants are placed in human bodies.[7] One key to the success of these dental and orthopaedic surgeries is whether mineralized bone is able to form at these artificial interfaces to form a long-lasting and biomechanically load-bearing bond, termed osseointegration.[8,9] The research on osseointegration not only explores the strategies of bone-implant design and modification to accelerate bone regeneration[10], but also helps to shed light on the mechanism of biomineralization at these interfaces between natural organisms and engineered biomaterials.

However, the mechanism of osseointegration is still debated. Physico-mechanical interdigitation and bio-chemical bonding have been reported as the potential contact modes at bone-implant interfaces.[11] Davies *et al.* proposed a non-collagenous hypermineralized layer similar to the cement line as the layer responsible for direct bonding of bone and implant.[12,13] Steflik *et al.* observed the existence of proteoglycans at the interface which are highly polyanionic and able to bind Ca^{2+} by electrostatic bonding so as to generate an initial amorphous Ca-rich layer.[14,15] McKee *et al.* showed that

osteopontin in cement lines acts as an interfacial adhesion promoter in bone-bone bonding and bone-implant bonding.[16] In addition, an osseohybridization model was recently put forward suggesting the potential presence of a $CaTiO_3$ hybridized layer at the titanium dental implant-bone interface.[17] One of the key remaining issues is the distribution of calcium-based (i.e. inorganic) and carbon-based (i.e. organic) components, at the bone-implant interface and their origins. Until now, this has not been fully understood, particularly with spatial and chemical clarity at the nanometer scale.

Owing to the hierarchically structured nature of bone and the inhomogeneous topographical quality of the implant surface, multiple-length-scale three dimensional (3D) visualization characterization techniques have been exploited to visualize bone-implant interfaces[7]. The understanding of osseointegration has also evolved with breakthroughs in discerning finer structures at the interface. X-ray micro- computed tomography (X-ray CT) enables visualization of large volumes with micron resolution to reveal microscaled bone ingrowth surrounding the implant for histological-like quantitative analysis.[18] The concept of nano-osseointegration was put forward based on electron tomography (ET) observations with scanning transmission electron microscopy (STEM) high-angle annular dark-field (HAADF) imaging mode that enhanced compositional contrast.[19] Recently, the atomic continuity at the bone-implant interface was also investigated by atom probe tomography (APT).[20,21] However, in order to contribute to the unresolved mechanisms of osseointegration, both nanoscale structural and elemental distribution at the bone-implant interface is needed across three dimensions. Thus, spatial 3D characterization techniques should step further towards so-called four dimensional (4D) techniques by adding chemical information as the fourth dimension.[22]

Spectroscopic electron tomography is a recently developed 4D technique to visualize 3D chemical information with nanometer resolution.[23] Based on acquiring energy filtered

images or spectroscopic images at different tilt angles, it comprises either energy-filtered TEM (EFTEM) tomography, or more recently energy-dispersive X-ray spectroscopy (EDS) tomography, or electron energy-loss spectroscopy (EELS) tomography in STEM mode.[24]. With the development of detector technology, EELS tomography is able to limit the electron beam dose exposure to biological specimens and has high sensitivity to light elements.[25] Atom probe tomography (APT), another 4D imaging technique, is based on field emission of surface atoms under a strong electric field or pulsed UV laser illumination. APT combines sub-nanometer spatial resolution with chemical sensitivity across the entire periodic table.[26, 27] APT has been successfully applied to study biomaterials such as biominerals[28, 29], dentin[30], and human bone[31]. X-ray absorption spectroscopy (XAS) in soft X-ray scanning transmission X-ray microscopes (STXM) provides speciation-based chemical mapping in 2D[32] and 3D[33] with better than 30 nm spatial resolution and has been applied to several biomineralization systems,[34,35] including bone.[36] Furthermore, STEM-EELS and STXM-XAS are able to probe the chemical states of each element at the nanoscale on the basis of characteristic fine structural features at the core level excitation edge. However, considering the complex nature of biomaterials and the limitations of each single technique, correlative characterization using complementary techniques is essential for reliable analysis and validation.[37–39]

Here, we report the first correlative application of on-axis ET, EELS tomography, and APT, as well as complementary electron energy-loss near-edge structure (ELNES), and STXM-XAS to acquire nanoscaled structural and chemical information from the intricate biointerface between human bone and titanium dental implant to provide insights on bone attachment mechanisms.

4.3 Results and Discussion

Osseointegration on multiple length scales

Human bone has complex hierarchical structures with nanoscaled building units of Type

I collagen and carbonated hydroxyapatite crystals. After a titanium implant is placed *in vivo*, new bone forms along the implant surface to generate a biomechanically functional integration. Due to the hierarchical character of bone, this integration should also exist on multiple length scales. As revealed in Figure 4-1, correlative tomographic reconstructions of the same sample sharpened into a needle can be used to visualize the human bone-implant interface from nanometer to atomic length scales. Figure 4-1 (a) shows the reconstructed 3D volume from on-axis HAADF-STEM ET, which provides Z- (atomic number) contrast to differentiate the Ti implant (the brightest structure), collagen fibrils (the darkest structure), and apatite (the intermediate contrast flake-like structures).[40] The continuous incorporation of bone structure with the nano-topographic oxide layer on the surface of this laser-modified commercially pure titanium (cp-Ti) dental implant is visualized in 3D, providing experimental evidence of nano-osseointegration. Since this implant has been placed in the human body for 47 months, the bone near the interface has likely been remodeled and the ultrastructure of mature bone can be identified in orthoslices of the reconstructed volume (Supplementary Figure 4-1, Video S1 in the Supplementary Information). On-axis ET not only circumvents the "missing wedge" problem, which causes artifacts and limits the resolution of 3D reconstructions[40], but it is also suitable to correlate with 4D EELS tomography (Figure 4-1 (b)) and APT (Figure 4-1 (c)) due to its needle-like sample geometry.

The EELS tomographic reconstruction (Figure 4-1 (b)) of the same needle, after sharpening to 100 nm in diameter to enable spectroscopy, complements the nano-scale chemical distributions to the 3D structures at the interface. Even though the Z-contrast of HAADF imaging in ET helps to differentiate the different phases in the sample, the EELS elemental reconstructed volume offers more accurate chemical visualization. Ca concentrated areas (in green), representing bone apatite, are distributed complementary to C concentrated areas (in red), representing organic components of bone. For APT

characterization, the same needle was further sharpened down to around 50 nm in diameter using focused ion beam (FIB). The 3D reconstructed APT volume (Figure 4-1(c)) is rendered in ions and both Ca and C were shown in direct contact with the oxide layer, suggesting osseointegration at the atomic level. This correlative tomography workflow helps to visualize the inhomogenous and hierarchical bone-implant interface, and it is also applicable to the investigation of other complex biointerphases.

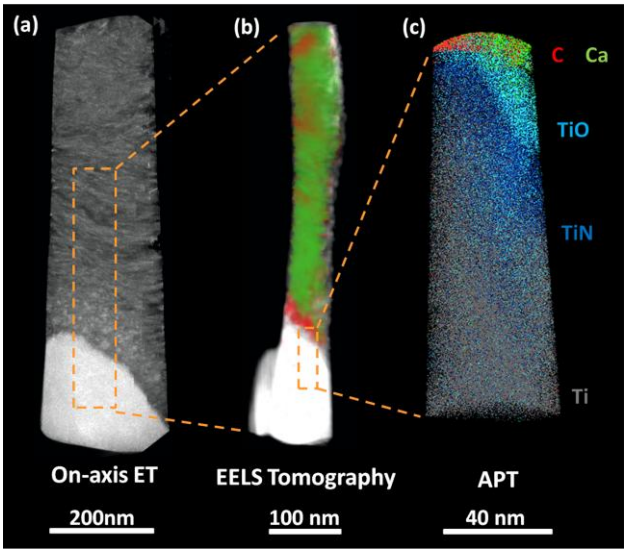

Figure 4-1. Correlative tomographic reconstructions of the human bone-implant interface from the same sample needle. (a) On-axis electron tomographic reconstruction of the bone (top)-implant (bottom) interface with 3D renderings in grey scale. (b) A representative 3D on-axis EELS volume, where red represents Carbon (C), green represents Calcium (Ca) and white represents Titanium (Ti). (c) Atom probe tomography 3D reconstruction with Ca-containing ions displayed in green, C-containing ions in red, TiO ions in bright blue, TiN ions in dark blue and Ti ions in grey.

Nanoscale elemental distribution in 3D

Based on the conflicting mechanisms of osseointegration, elucidating the elemental distribution at the bone-implant interface is a vital piece of experimental evidence. Two-dimensional EELS or EDX elemental mapping has been the gold-standard to present elemental distribution at interfaces. However, these spectroscopic methods in TEM are based on 2D projections of a 3D sample, which are therefore difficult to interpret as many overlapping features in the sample volume are collapsed into 2D. EELS

tomography enables visualization of elemental distribution in 3D reconstructed volumes, and much more clearly correlates the chemical information to the structures identified by HAADF STEM tomography than the granular and sparse 2D EELS maps. Figure 4-2 (a) and (b) show a comparison between 2D EELS elemental maps and EELS tomography reconstructions, respectively. Collagen fibrils, visualized as the higher contrast, highly C-concentrated areas, are clearly identified from the 3D EELS orthoslices (Figure 4-2 (c)) as structures distributed parallel to the implant interface throughout the bone (highlighted in the yellow box), while other collagenous structures are more randomly distributed near the interface (highlighted in the red box). This morphology change could be described as a transitional layer, where bone structure is less ordered, with randomly distributed collagen fibrils and denser bone apatite distribution directly at the oxide layer surface (Supplementary Figure 4-2, Video S2 in the Supplementary Information). The titanium oxide layer is highlighted by two blue dotted lines through the 3D EELS orthoslices (Figure 4-2 (c)). Both C and Ca were observed penetrating this oxide layer, which correlates with our observations presented in Figure 4-1 from APT (elaborated in Figure 4-3), supporting an atomic-scale integration of bone constituents into the surface oxide.

Due to the considerable electron beam exposure during the EELS tomography acquisition, the effect of beam damage should be taken into consideration. A clear beam-induced hydrocarbon contamination shell was observed on the surface of the sample needle (Figure 4-2 (c)). Since bone is an organic and inorganic composite material, it acts as a local source of hydrocarbons. Studies have proven that this thin C contamination layer covering the sample could act as a C coating to reduce mass loss.[41] By comparing EELS tomography with electron tomography, no obvious structural artifacts, besides the formation of the C shell, are seen. This C shell has been cropped from reconstructed volumes for easier visualization (Figure 4-2 (b)).

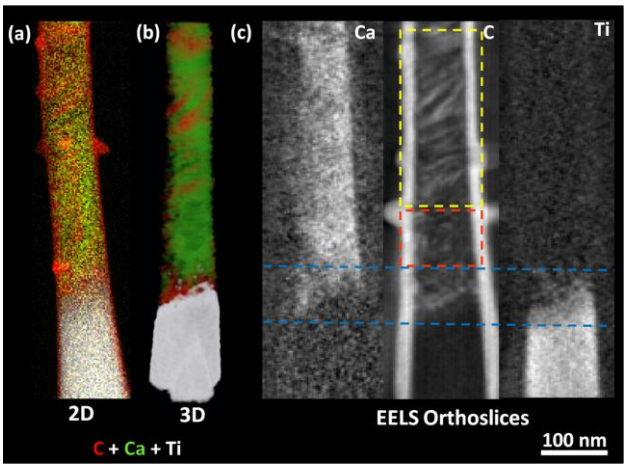

Figure 4-2. Representative elemental distribution of bone-implant interface revealed by on-axis EELS tomography. (a) EELS elemental distribution 2D maps of C (red), Ca (green) and Ti (white) from the 0 ° tilt angle. (b) The corresponding 3D reconstructed elemental volumes from EELS maps acquired over a tilt range of ±70 °. (c) XY orthoslices extracted from the 3D reconstructed EELS tomograms showing the elemental distribution of Ca, C and Ti inside of the sample volume. The implant oxide layer is highlighted by blue lines, and the ordered collagen fibrils are highlighted by the yellow box, with an intermediary unorganized zone in red.

Atomic level mapping of osseointegration

Figure 4-3 (a) shows another representative APT reconstruction of the interface between human bone and oxidized Ti implant. Both Ca, which represents bone mineral, and C, which represents organic components, are shown in direct contact with the oxide layer, corroborating the observations in our correlative EELS tomography and previous APT datasets mentioned above. From the proxigram (Figure 4-3 (c-d)), the gradient concentration change of Ca and Ti across the interface provides authenticity to the atomic continuum of osseointegration. Other APT studies on different implant surfaces, such as mesoporous titania coatings[21] and a sand-blasted acid etched (SLA, Straumann)[20] also showed Ca immediately adjacent to titanium implant surfaces. In this work, a small N enrichment is noted between Ti metal and oxide layer, which may be attributed to the laser surface modification process carried out in ambient air. Although APT provides atomic scale 3D visualization of element distributions, it is unable to determine the exact chemical environment of each element, which is complemented by a more detailed

spectroscopic study in the following section. However, due to the high sensitivity of APT (down to 1 ppm), trace elements of magnesium (Mg) and sodium (Na) were detected at the interface. Previous APT research on human bone has demonstrated the co-localization of Na with C-rich regions in bone structure.[31] This result agrees well with observations from secondary ion mass spectroscopy (SIMS), which stated that abundant Na exists largely in organic material in bone.[42] Na^+ plays a key function in ion exchange and transportation during cell activations involved in the bone generation process. Inorganic phosphate (Pi) is an essential component for bone mineralization, which has been known to be accumulated and transported by sodium-dependent (NaPi) transporters in osteogenic cells.[43] Also, a similar functional protein sodium-dependent citrate transporter is reported to regulate citrate take-up and release in osteoblasts.[44] Citrate has been reported to bind strongly on the surface of apatite to regulate crystal growth orientation and size.[45,46]

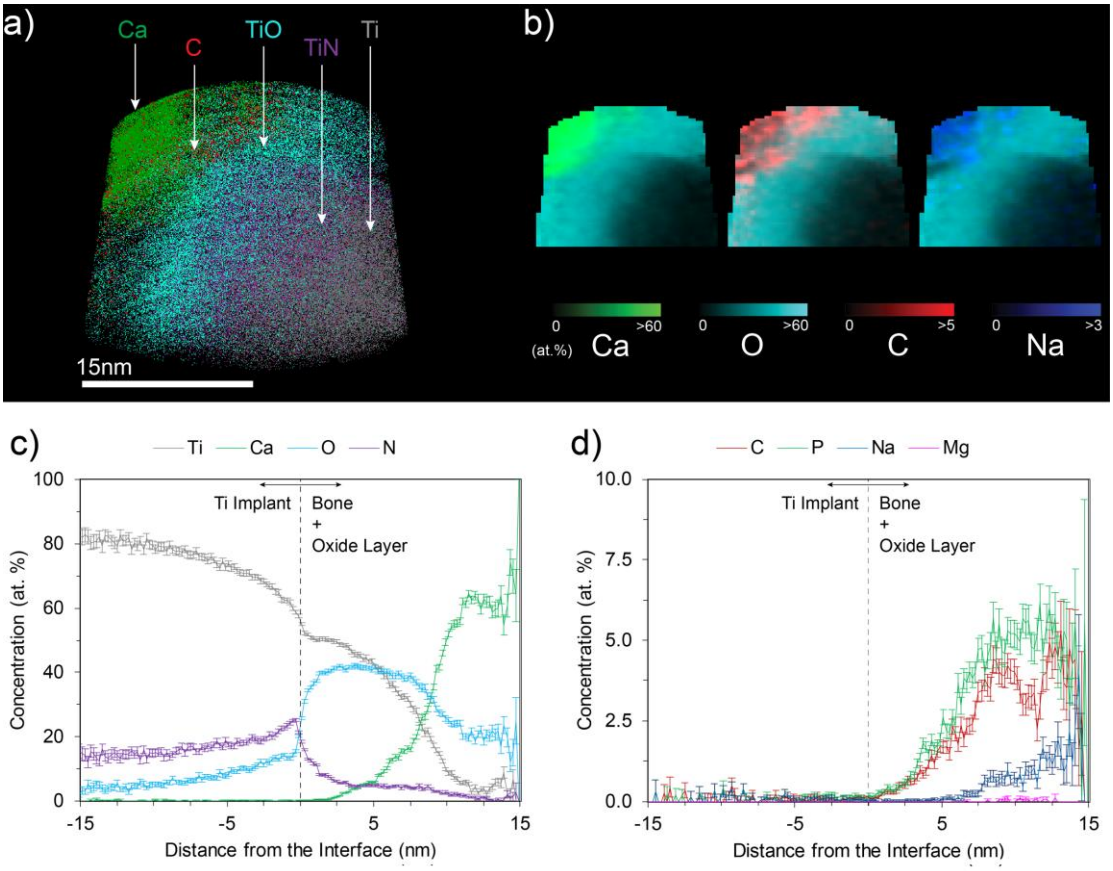

Figure 4-3. Atom probe tomography of the human bone-implant interface. (a) 3D reconstructed APT volume with Ca-containing ions displayed in green, C-containing ions displayed in red, TiO ions displayed in bright blue/cyan, TiN ions in purple and Ti ions displayed in grey. Atomic-scale integration of Ca ions with the oxide layer is noted. (b) Overlay of Ca, C, and Na ion positions on oxygen concentration maps. (c) Supporting proximity histograms across the implant-bone interface showing the integration of Ca within the oxide, and (d) the presence of trace elements like Mg and Na in the bone structure which presents immediately adjacent to the oxide lay of the implant.

Transient mineral phase at bone-implant interface

Hydroxyapatite or its carbonate-substituted form is generally accepted to be the inorganic constituent of bone, which, evidence suggests, passes through different apatite phase transitions during its mineralization process. Different apatite phases have significantly different Ca/P concentration ratios, and thus Ca/P ratio is a traditional method to differentiate apatite phases.[47] However, the atomic ratio determined by APT is quantitatively unreliable for such inhomogeneous composites. Due to the comparatively high background and thermal tails in the APT spectra, which are caused by the low thermal conductivity of the sample, many small peaks are obscured, thus reducing the accuracy of quantitative analysis. This is particularly important for quantification of P, as it has a tendency to form numerous complex ions when evaporating during the APT data acquisition stage.[31] However, ELNES can probe the local environment of Ca atoms so as to differentiate different apatite phases, combining superior spatial resolution with high energy resolution.[48] Figure 4-4 (c) compares Ca-$L_{2,3}$ ELNES from bone (blue box in Figure 4-4 (a)) and the bone-implant interface (red box in Figure 4-4 (b)). The double peak spectrum can be deconvoluted into four components by Gaussian fitting (Supplementary Figure 4-3). While the two main spin-orbit split peaks L_3 (peak 3), and L_2 (peak 1) are positioned identically among different apatites, the positions of peaks 2 and 4 are characteristically used to identify the apatite phase.[49] The detailed peak positions of interest together with reference apatites are listed in Table 4-1[49]. A slight shift in peak 4 is discerned by comparing the Ca-$L_{2,3}$ ELNES of bone (Figure 4-4 (c) blue line) and the interface (Figure 4-4 (c) red line). Based on the comparison with reference

apatites in Table 4-1, the Ca of bone should originate from hydroxyapatite (HA), whereas the Ca at the interface is similar to amorphous calcium apatite (ACP). ACP has been suggested as a transient phase during mineralization processes by many studies. e.g. mouse tooth enamel[49], and zebrafish fin ray bone[50]. Here, the transient phase of ACP was observed displaying direct contact with the implant oxide layer at the human bone-implant biomineralization interface. The existence of a different Ca species at the interface is also supported by STXM-XANES of Ca-$L_{2,3}$ (Supplementary Figure 4-4).

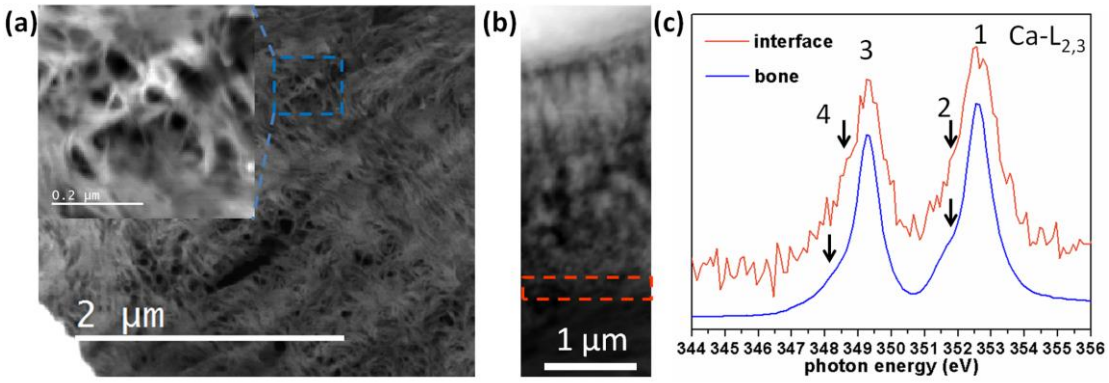

Figure 4-4. ELNES comparison of Ca-$L_{2,3}$ from bone and interface. HAADF-STEM images of mature bone (a) and interface (b). (c) Ca-$L_{2,3}$ edges of bone (in blue) and interface (in red) are extracted from the regions highlighted by the dashed squares in corresponding colors in (a) and (b). Four discernable peaks are indicated by arrows and their accurate positions are included in Table 1.

Table 4-1. Energy positions of four main peaks Ca-$L_{2,3}$ ELNES. The energy separation (Δ) of peaks 3 and 4 highlights the crystalline nature of the minerals.

	Peak 1 position (eV)	Peak 2 position (eV)	Peak 3 position (eV)	Peak 4 position (eV)	$\Delta_{peak3 - peak4}$ (eV)
Reference HA	352.6	351.6	349.3	348.4	0.9
Reference ACP	352.6	351.6	349.3	348.8	0.5
Bone	352.6	351.6	349.3	348.4	0.9
Interface	352.6	351.6	349.3	348.7	0.6

TiN layer in the commercial dental implant

A distinct N-rich layer was observed between the oxide layer and Ti metal in the APT 3D reconstructed volume (Figure 4-5 (d)). In order to identify the origin of N in this layer,

the N-K edge was studied by STXM-XANES on a similar lamellar TEM sample from the same specimen to gain a large-scale overview of the spatial distribution of N-containing species. The optical density difference map (Figure 4-5 (b)) shows an obvious N-rich layer which is correlated to the APT results. From the STEM-HAADF (Figure 4-5 (a)) and STXM (Figure 4-5 (b)) images, this N-rich layer distributes perfectly along the interface. XANES spectra extracted from representative regions of the bone (green), N-rich layer (blue), and implant (red) (Figure 4-5 (e)) were used to fit the N-K edge stack (images at 50 energies from 395 to 421 eV) to derive component maps of the 3 distinct N-containing species. These component maps are presented as a combined rescaled color coded composite (Figure 4-5 (c)). Spectroscopically, the narrow double peak around 400 eV in the N-K edge spectrum of the N-rich layer (blue in Figure 4-5) is the characteristic "fingerprint" of TiN.[51] The N-K edge spectrum of the implant region (red in Figure 4-5) has a completely different fine structure with only one sharp peak followed by a broad signal in the N-K continuum. The shape of the N-K edge spectrum of localized band in the implant region matches that of the hexagonal Ti_2N phase.[52] The implant used in this study is made from commercially pure titanium (cp-Ti)[40], which has a hexagonal close-packed atomic structure. Nitrogen is soluble in the hexagonal structure to a limited extent.[53] The N-K edge spectrum of the bone region (green in Figure 4-5) is likely the mixture of signals from different organic components of bone [48], such as collagen and other functional non-collagenous proteins. The fine structure in the 400 to 403 eV region is typical of N-K edge XANES of proteins, which are dominated by N 1s $\rightarrow \pi^*_{peptide}$ transitions.[54,55] The map of the bone component and a comparison to the N-K edge spectrum of collagen are shown in supplemental Figure 4-7.

In order to investigate whether this N-rich layer was formed *in vivo*, the same dental implant prior to implantation was characterized by EELS. A similar N-rich region was also discernible from the elemental mapping (Supplementary Figure 4-5), suggesting that,

as suspected, it was formed during the laser modification of the implant surface in an ambient air environment. In other studies, a titanium hydride layer has been reported as a result of argon plasma treatment, sand-blasting and acid-etching of titanium implant surfaces.[56,57] However, this is the first time that this N-rich layer localized on the sub-surface of a commercial dental implant has been observed. Due to the different mechanical properties and biocompatibility of TiN compared to titanium dioxide, the introduction of TiN during machining should be considered during implant design.

In addition, the spectra of the C-K, Ti- $L_{2,3}$ and O-K edges were also investigated by STXM-XANES over the area displayed in Figure 4-5 (b). Different types of TiO_x signals are observed in the bone-implant interface region in both the Ti-$L_{2,3}$ and O-K edges. They are subtly different but reliably fit two separate regions distributed at the implant oxide layer: one region in connection with the bone, and the other directly adjacent to the implant surface (Supplementary Figure 4-6). This finding indicates the need for further investigation on the formation of these different phases of the oxide layer, in particular, to determine whether they are formed *in vivo* or during implant surface modification by laser. As for the spectra of C-K edge, two distinct C spectral signatures were found in the bone region, showing the existence of two species of C: carbonate and collagen (Supplementary Figure 4-7). However, the possible effects of electron beam damage in TEM and ion beam in FIB should be taken into consideration when analyzing the fine structures of C spectra.

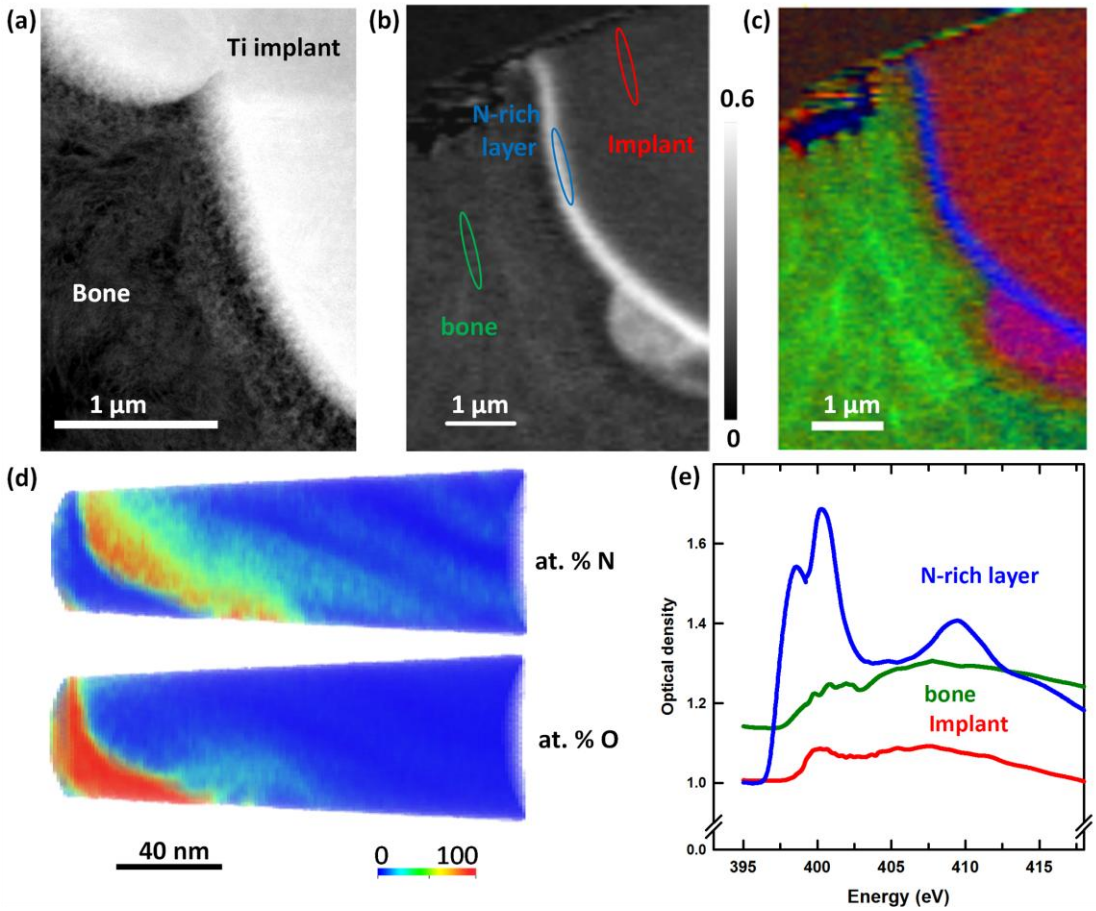

Figure 4-5. Correlative APT and XANES characterization of the human bone-implant interface. (a) HAADF-STEM image of the bone-implant interface. (b) Optical density difference map ($OD_{400\ eV}$ –$OD_{396\ eV}$) showing N-rich band. (c) Color coded map of 3 N-containing components: N-rich layer (blue), bone (green) and implant (red), derived from the fit of N-K edge stack to the N spectra in (e). The N-rich interfacial layer is also observed in the APT 3D reconstructions in (d) showing the atomic concentration of N and O. (e) N-K edge XANES spectra from the N-rich layer, bone region and implant region, extracted from the regions indicated in (b).

4.4 Conclusion

This paper reports the first correlative 4D chemical tomography study of a bone-implant interface, including on-axis electron tomography, EELS tomography, and APT performed on the same sample. The combination of these methods reveals both nano and atomic scale information needed to understand biomineralization at the bone-implant interface. Based on morphological and chemical changes, observed by correlative 4D tomographic methods with supportive ELNES and XANES analyses, evidence for the existence of a

transitional biointerphase at the bone-implant interface was demonstrated. On this particular laser modified Ti dental implant, this intervening transition zone consisted of a disorganized apatite rich material, which was identified as ACP immediately at the oxide surface by ELNES. In addition, the correlative APT analysis and spectroscopy characterizations provided new insights on the implant modification process and identified a TiN layer between the surface oxide and bulk metal of the commercial dental implant. Both findings have implications for the immediate and long-term osseointegration of dental implants. The correlative 4D tomographic workflow presented here for the bone-implant interface is applicable to other biological systems or materials science applications.

4.5 Materials and Methods

Implant and human bone interface sample preparation. The sample used in this study was from Biobank 513 at the University of Gothenburg, Sweden and was a dental implant (BioHelix™, Brånemark Integration AB, Mölndal, Sweden) retrieved from a 66-year old female patient after 47 months in service. This study was conducted under the ethical approval from the Hamilton Integrated Research Ethics Board at McMaster University. This screw-shaped commercial pure titanium dental implant was partly laser-modified in the thread valleys via a Q-switched Nd:YAG laser (Rofin-Sinar Technologies Inc., Plymouth, USA) at an infrared wavelength of 1064 nm and spot size 100 μm, in ambient air. The implant with the surrounding human bone was fixed in formalin, dehydrated in a graded series of ethanol, embedded in plastic resin (LR White, London Resin Company, UK) and cut longitudinally for further study.

On-axis electron tomography, EELS tomography and APT sample preparation. A dual-beam FIB instrument (Zeiss NVision 40, Carl Zeiss AG) equipped with a 30 kV gallium ion column, FEG SEM, carbon and tungsten gas injector system (GIS), and Kleindiek micromanipulator (Kleindiek Nanotechnik GmbH) was employed to prepare

all TEM lamellae and needle-shaped samples for on-axis electron tomography, EELS tomography and APT following published protocols[40]. A site of interest at the bone-implant interface was selected from the thread valleys where the implant was laser-modified, and was protected by a layer of tungsten deposition (10 µm x 2 µm x 0.5 µm). After rough milling of trenches, a wedge-shaped sample was lifted out and attached to the top of electropolished tungsten wires mounted in 1.8 mm copper tubes. The mounted wedge was annularly milled into needles to a final diameter of approximately 200 nm using a 30 kV ion beam at successively lower currents (150-10 pA). A final low keV beam (10 kV, 80 pA) polishing step was performed to reduce surface damage and Ga ion implantation. After on-axis electron tomography, the needle-shaped sample was put back into the FIB and milled to 70 nm in diameter, which was suitable for both EELS tomography and APT using a low keV beam (10 kV, 80 pA). After the EELS tomography, FIB was also used to remove the surface C contamination using the same low beam of 10 kV and 80 pA.

On-axis electron tomography methods. The prepared needle of 200 nm diameter on the tungsten wire was mounted a Model 2050 on-axis rotation tomography holder (E.A. Fischione Instruments, Inc., Export, PA) and rotated through $\pm 90°$ with an angular step size of $2°$ in the scanning transmission electron microscope (STEM) (Titan 80-300, operated at 300kV). This tomographic tilt-series was acquired using on a high-angle annular dark-field (HAADF) detector which provides Z contrast and by using FEI's Explore 3D software. The post-acquisition image alignment via cross-correlation and reconstruction with simultaneous iterative reconstruction (SIRT, 20 iterations) were completed with the Inspect 3D (FEI Company, The Netherlands) software. The reconstructed volume was visualized via volume rendering and orthoslices using software Avizo (FEI Company, The Netherlands). The reconstructed volume was cropped by a custom MATLAB script (The Mathworks, Natick, MA).

EELS tomography and ELNES methods. A series of STEM-EELS spectrum images and corresponding dark-field images of the prepared 70 nm diameter needle were acquired in the tilt range $\pm 70°$ with $2°$ tilt increment on a FEI Titan 80-300 microscope (FEI Company, Eindhoven, The Netherlands), operated at 300 kV. The microscope is equipped with a CEOS Probe Corrector, CEOS Image Corrector (CEOS GmbH, Heidelberg, Germany), and Gatan Quantum energy filter (Gatan Inc., Pleasanton, CA). The collection semi-angle was 40 mrad and the probe current was ~30 pA. The pixel size in the object plane was set to 1.56 nm, the exposure time for each pixel was 5 ms. The high-speed acquisition capability of the Quantum energy filter reduced acquisition time to about 2 minutes per spectrum image. Elemental distribution maps were extracted for Ca, C, Ti and O from EELS spectrum images at every tilt angle using a power-law background model. For reconstruction, the alignment of the dark-field images was completed via cross-correlation by the software Inspect 3D (FEI Company, Eindhoven, The Netherlands) and the same shifts were applied to stacks of the chemical distribution maps of each element. The reconstruction of all stacks was performed using Inspect 3D with SIRT (25 iterations). The reconstructed volumes were visualized using Amira. The reconstructed needle showed a shell of carbon contamination which accumulated on the needle's surface during data acquisition. In order to better visualize the carbon signal from the interior of the needle, the outside shell was removed by manually segmenting the needle surface and removing the outside carbon signal using a custom MATLAB script (The Mathworks, Natick, MA).

For ELNES, the spectrometer was set to an energy dispersion of 0.1 eV/channel to obtain the best energy resolution at the zero-loss peak (0.3 eV). The collection angle and convergence angle were 55 mrad and 19 mrad, respectively. The collection aperture was 5 mm in radius and a dwell time of 0.015 sec/pixel was used. Linear least-square fitting was used to remove background with a power law model.

APT methods. Before APT, the needle-shaped samples were cleaned in the FIB and sputter coated with 15 nm of Ag. The atom probe experiments were conducted on a LEAP 4000XHR atom probe microscope (CAMECA Scientific Instruments, Madison, WI). A laser pulse (λ = 355 nm, 120 pJ, 100 kHz) was used to incite field evaporation from the sample with a base temperature of approximately 43.4 K and the chamber pressure of 4.0×10^{-9} Pa. The evaporation rate was maintained around 0.005 ions/pulse (0.5%) by controlling the direct-current potential on the sample. Reconstruction and analysis was completed using the Integrated Visualization and Analysis Software package (IVAS) v3.6.8 (CAMECA Scientific Instruments, Madison, WI) assuming the shape was a hemispherical tip on a truncated cone. The reconstruction was spatially defined by assuming the tip radius to evolve as a function of a constant specimen shank angle. The input parameters for this algorithm of initial tip radius and specimen shank angle were obtained from STEM images of the sample, taken both before and after the APT experiment. This is critical for ensuring the accuracy of the reconstruction.

STXM-XANES analysis. The soft X-ray spectromicroscopy beamline 10ID1 (SM)[58] at the Canadian Light Source (CLS, Saskatoon, SK, Canada) was used for the STXM-XANES study. STXM methodology has been described in detail previously.[32] Briefly, monochromated X-rays are focused to ~30 nm by a Fresnel zone plate. The sample is positioned at the focal point and mechanically x-y raster scanned (1 ms/pixel) while recording the transmitted X-rays. Spectral data at the C-K, Ca-L_{23}, N-K, Ti- L_{23}, and O-K edges was collected by image sequences over the area displayed in Figure 4-5 (b). All data was analyzed by aXis2000.[59]

4.6 References

(1) Addadi, L.; Weiner, S. Biomineralization: Mineral Formation by Organisms. *Phys. Scr.* **2014**, *89*, 098003.

(2) Wegst, U. G. K.; Bai, H.; Saiz, E.; Tomsia, A. P.; Ritchie, R. O. Bioinspired Structural Materials. *Nat. Mater.* **2014**, *14*, 23–36.

(3) Habraken, W.; Habibovic, P.; Epple, M.; Bohner, M. Calcium Phosphates in Biomedical Applications: Materials for the Future? *Mater. Today* **2016**, *19*, 69–87.

(4) Nudelman, F.; Lausch, A. J.; Sommerdijk, N. a J. M.; Sone, E. D. In Vitro Models of Collagen Biomineralization. *J. Struct. Biol.* **2013**, *183*, 258–269.

(5) Lausch, A. J.; Quan, B. D.; Miklas, J. W.; Sone, E. D. Extracellular Matrix Control of Collagen Mineralization in Vitro. *Adv. Funct. Mater.* **2013**, *23*, 4906–4912.

(6) Rodrigues, D. E.; Thula-Mata, T.; Toro, E. J.; Yeh, Y.-W.; Holt, C.; Holliday, L. S.; Gower, L. B. Multifunctional Role of Osteopontin in Directing Intrafibrillar Mineralization of Collage and Activation of Osteoclasts. *Act Biomater.* **2014**, *10*.

(7) Grandfield, K. Bone, Implants, and Their Interfaces. *Phys. Today* **2015**, *68*, 40–45.

(8) Brånemark, P. I.; Breine, U.; Adell, R.; Hansson, B. O.; Lindström, J.; Ohlsson, A. Intra-Osseous Anchorage of Dental Prostheses. I. Experimental Studies. *Scand. J. Plast. Reconstr. Surg.* **1969**, *3*, 81–100.

(9) Brånemark, R.; Brånemark, P. I.; Rydevik, B.; Myers, R. R. Osseointegration in Skeletal Reconstruction and Rehabilitation: A Review. *J. Rehabil. Res. Dev.* **2001**, *38*, 175–181.

(10) Goutam, M.; Chandu, G. S.; Mishra, S. K.; Singh, M.; Tomar, B. S. Factors Affecting Osseointegration : A Literature Review. *J. Orofac. Res.* **2013**, *3*, 197–201.

(11) Sul, Y. T. The Significance of the Surface Properties of Oxidized Titanium to the Bone Response: Special Emphasis on Potential Biochemical Bonding of Oxidized Titanium Implant. *Biomaterials* **2003**, *24*, 3893–3907.

(12) Davies, J. E.; Mendes, V. C.; Ko, J. C. H.; Ajami, E. Topographic Scale-Range Synergy at the Functional Bone/implant Interface. *Biomaterials* **2014**, *35*, 25–35.

(13) Davies, J. E. Bone Bonding at Natural and Biomaterial Surfaces. *Biomaterials* **2007**, *28*, 5058–5067.

(14) Steflik D. E., Sisk A. L., Parr G. R., Gardner L. K., Hanes P. J., Lake F. T., *et al.* High-Voltage Electron Microscopy and Conventional Transmission Electron Microscopy of the Interface Zone between Bone and Endosteal Dental Implants. *J. Biomed. Mater. Res.* **1992**, *26*, 529-545.

(15) Klinger, M. M.; Rahemtulla, F.; Prince, C. W.; Lucas, L. C.; Lemons, J. E. Proteoglycans at the Bone-Implant Interface. *Crit. Rev. Oral Biol. Med.* **1998**, *9*, 449–463.

(16) McKee, M. D.; Nanci, a. Osteopontin at Mineralized Tissue Interfaces in Bone, Teeth, and Osseointegrated Implants: Ultrastructural Distribution and Implications for Mineralized Tissue Formation, Turnover, and Repair. *Microsc. Res. Tech.* **1996**, *33*, 141–164.

(17) Kim, J.; Kang, S.; Seo, K.; Nahm, K.; Chung, K.; Kim, S.; Ahn, J. Nanoscale Bonding between Human Bone and Titanium Surfaces : Osseohybridization. **2014**.

(18) Thorfve, A.; Palmquist, A.; Grandfield, K. Three-Dimensional Analytical Techniques for Evaluation of Osseointegrated Titanium Implants. *Mater. Sci. Technol.* **2015**, *31*, 174–179.

(19) Grandfield, K.; Gustafsson, S.; Palmquist, A. Where Bone Meets Implant: The Characterization of Nano-Osseointegration. *Nanoscale* **2013**, *5*, 4302–4308.

(20) Sundell, G.; Dahlin, C.; Andersson, M.; Thuvander, M. The Bone-Implant Interface of Dental Implants in Humans on the Atomic Scale. *Acta Biomater.* **2016**, *48*, 445–450.

(21) Karlsson, J.; Sundell, G.; Thuvander, M.; Andersson, M. Atomically Resolved Tissue Integration. *Nano Lett.* **2014**, *14*, 4220–4223.

(22) Grandfield, K.; Palmquist, A.; Engqvist, H. High-Resolution Three-Dimensional Probes of Biomaterials and Their Interfaces. *Philos. Trans. R. Soc. A* **2012**, *370*, 1337–1351.

(23) Möbus, G.; Doole, R. C.; Inkson, B. J. Spectroscopic Electron Tomography. *Ultramicroscopy* **2003**, *96*, 433–451.

(24) Haberfehlner, G.; Orthacker, A.; Albu, M.; Li, J.; Kothleitner, G. Nanoscale Voxel Spectroscopy by Simultaneous EELS and EDS Tomography. *Nanoscale* **2014**, *6*, 14563–14569.

(25) Ercius, P.; Alaidi, O.; Rames, M. J.; Ren, G. Electron Tomography: A Three-Dimensional Analytic Tool for Hard and Soft Materials Research. *Adv. Mater.* **2015**, *27*, 5638–5663.

(26) Kelly, T. F.; Larson, D. J. Atom Probe Tomography 2012. *Annu. Rev. Mater. Res.* **2012**, *42*, 1–31.

(27) Devaraj, A.; Perea, D. E.; Liu, J.; Gordon, L. M.; Prosa, T. J.; Parikh, P.; Diercks, D. R.; Meher, S.; Kolli, R. P.; Meng, Y. S.; *et al.* Three-Dimensional Nanoscale Characterisation of Materials by Atom Probe Tomography. *Int. Mater. Rev.* **2017**, *0*, 1–34.

(28) Gordon, L. M.; Joester, D. Nanoscale Chemical Tomography of Buried Organic-Inorganic Interfaces in the Chiton Tooth. *Nature* **2011**, *469*, 194–197.

(29) Perea, D. E.; Liu, J.; Bartrand, J.; Dicken, Q.; Thevuthasan, S. T.; Browning, N. D.; Evans, J. E. Atom Probe Tomographic Mapping Directly Reveals the Atomic Distribution of Phosphorus in Resin Embedded Ferritin. *Sci. Rep.* **2016**, *6*, 22321.

(30) Gordon, L. M.; Tran, L.; Joester, D. Atom Probe Tomography of Apatites and Bone-Type Mineralized Tissues. *ACS Nano* **2012**, *6*, 10667–10675.

(31) Langelier, B.; Wang, X.; Grandfield, K. Atomic Scale Chemical Tomography of Human Bone. *Sci. Rep.* **2017**, *7*, 39958.

(32) Hitchcock, A. P. Soft X-Ray Imaging and Spectromicroscopy. In *the Handbook on Nanoscopy*; Wiley, 2012; pp. 745–791.

(33) Schmid, G.; Obst, M.; Wu, J.; Hitchcock, A. P. 3D Chemical Imaging of Nanoscale Biological, Environmental and Synthetic Materials by Soft X-Ray Spectro-Tomography. In *X-ray and Neutron Techniques for Nanomaterials Characterization*; Springer: Berlin, 2016; pp. 43–94.

(34) Obst, M.; Wang, J.; Hitchcock, a. P. Soft X-Ray Spectro-Tomography Study of Cyanobacterial Biomineral Nucleation. *Geobiology* **2009**, *7*, 577–591.

(35) Cosmidis, J.; Benzerara. K. Soft X-Ray Scanning Transmission Spectromicroscopy. In *Biomineralization Sourcebook*; CRC Press: London, UK, 2014.

(36) Cosmidis, J.; Benzerara, K.; Nassif, N.; Tyliszczak, T.; Bourdelle, F. Characterization of Ca-Phosphate Biological Materials by Scanning Transmission X-Ray Microscopy (STXM) at the Ca L2,3-, P L2,3- And C K-Edges. *Acta Biomater.* **2015**, *12*, 260–269.

(37) Devaraj, a.; Gu, M.; Colby, R.; Yan, P.; Wang, C. M.; Zheng, J. M.; Xiao, J.; Genc, a.; Zhang, J. G.; Belharouak, I.; *et al.* Visualizing Nanoscale 3D Compositional Fluctuation of Lithium in Advanced Lithium-Ion Battery Cathodes. *Nat. Commun.* **2015**, *6*, 8014.

(38) Arslan, I.; Marquis, E. a.; Homer, M.; Hekmaty, M. a.; Bartelt, N. C. Towards Better 3-D Reconstructions by Combining Electron Tomography and Atom-Probe Tomography. *Ultramicroscopy* **2008**, *108*, 1579–1585.

(39) Goode, A. E.; Porter, A. E.; Ryan, M. P.; McComb, D. W. Correlative Electron and X-Ray Microscopy: Probing Chemistry and Bonding with High Spatial Resolution. *Nanoscale* **2015**, *7*, 1534–1548.

(40) Wang, X.; Shah, F. a.; Palmquist, A.; Grandfield, K. 3D Characterization of Human Nano-Osseointegration by On-Axis Electron Tomography without the Missing Wedge. *ACS Biomater. Sci. Eng.* **2017**, *3*, 49–55.

(41) Egerton, R. F.; Li, P.; Malac, M. Radiation Damage in the TEM and SEM. *Micron* **2004**, *35*, 399–409.

(42) Bushinsky, D. A.; Gavrilov, K. L.; Chabala, J. A. N. M.; Levi-setti, R. Contribution of Organic Material to the Ion Composition of Bone. *J. Bone Miner. Res.* **2000**, *15*, 2026–2032.

(43) Albano, G.; Moor, M.; Dolder, S.; Siegrist, M.; Wagner, C. a.; Biber, J.; Hernando, N.; Hofstetter, W.; Bonny, O.; Fuster, D. G. Sodium-Dependent Phosphate Transporters in Osteoclast Differentiation and Function. *PLoS One* **2015**, *10*, 1–13.

(44) Irizarry, A. R.; Yan, G.; Zeng, Q.; Lucchesi, J.; Hamang, M. J.; Ma, Y. L.; Rong, J. X. Defective Enamel and Bone Development in Sodium-Dependent Citrate Transporter (NaCT) Slc13a5 Deficient Mice. *PLoS One* **2017**, *12*, e0175465.

(45) Hu, Y.-Y.; Rawal, a.; Schmidt-Rohr, K. Strongly Bound Citrate Stabilizes the Apatite Nanocrystals in Bone. *Proc. Natl. Acad. Sci.* **2010**, *107*, 22425–22429.

(46) Xie, B.; Nancollas, G. H. How to Control the Size and Morphology of Apatite Nanocrystals in Bone. *Proc. Natl. Acad. Sci.* **2010**, *107*, 22369–22370.

(47) Eliaz, N.; Metoki, N. Calcium Phosphate Bioceramics: A Review of Their History, Structure, Properties, Coating Technologies and Biomedical Applications. *Materials (Basel).* **2017**, *10*.

(48) Srot, V.; Bussmann, B.; Salzberger, U.; Koch, C. T.; van Aken, P. a. Linking Microstructure and Nanochemistry in Human Dental Tissues. *Microsc. Microanal.* **2012**, *18*, 509–523.

(49) Beniash, E.; Metzler, R. a.; Lam, R. S. K.; Gilbert, P. U. P. a. Transient Amorphous Calcium Phosphate in Forming Enamel. *J. Struct. Biol.* **2009**, *166*, 133–143.

(50) Mahamid, J.; Aichmayer, B.; Shimoni, E.; Ziblat, R.; Li, C.; Siegel, S.; Paris, O.; Fratzl, P.; Weiner, S.; Addadi, L. Mapping Amorphous Calcium Phosphate Transformation into Crystalline Mineral from the Cell to the Bone in Zebrafish Fin Rays. *Proc. Natl. Acad. Sci.* **2010**, *107*, 6316–6321.

(51) Lazar, P.; Redinger, J.; Strobl, J.; Podloucky, R.; Rashkova, B.; Dehm, G.; Kothleitner, G.; Šturm, S.; Kutschej, K.; Mitterer, C.; *et al.* N-K Electron Energy-Loss near-Edge Structures for TiN/VN Layers: An Ab Initio and Experimental Study. *Anal. Bioanal. Chem.* **2008**, *390*, 1447–1453.

(52) Hofer, F.; Warbichler, P.; Scott, a.; Brydson, R.; Galesic, I.; Kolbesen, B. Electron Energy Loss near Edge Structure on the Nitrogen K-Edge in Vanadium Nitrides. *J. Microsc.* **2001**, *204*, 166–171.

(53) McCracken, M. Dental Implant Materials: Commercially Pure Titanium and Titanium Alloys. *J. Prosthodont.* **1999**, *8*, 40–43.

(54) Zubavichus, Y.; Zharnikov, M.; Schaporenko, a.; Grunze, M. NEXAFS Study of Glycine and Glycine-Based Oligopeptides. *J. Electron Spectros. Relat. Phenomena* **2004**, *134*, 25–33.

(55) Stewart-Ornstein, J.; Hitchcock, A. P.; Cruz, D. H.; Henklein, P.; Overhage, J.; Hilpert, K.; Hale, J. D.; Hancock, R. E. W. Using Intrinsic X-Ray Absorption Spectral Differences to Identify and Map Peptides and Proteins. *J. Phys. Chem. B* **2007**, *111*, 7691–7699.

(56) Justicia, J.; Rosales, A.; Bañuel, E.; Oller-López, J. L.; Valdivia, M.; Haïdour, A.; Oltra, J. E.; Barrero, A. F.; Cárdenas, D. J.; Cuerva, J. M.; *et al.* To Print This Article, Please Use the Print Button in the Bottom Toolbar of the Web Reader. *J. Clin. Nurs.* **2004**, *19*, 3274–3290.

(57) Conforto, E.; Caillard, D.; Aronsson, B.-O.; Descouts, P. Crystallographic Properties and Mechanical Behaviour of Titanium Hydride Layers Grown on Titanium Implants. *Philos. Mag.* **2004**, *84*, 631–645.

(58) Kaznatcheev, K. V.; Karunakaran, C.; Lanke, U. D.; Urquhart, S. G.; Obst, M.; Hitchcock, a. P. Soft X-Ray Spectromicroscopy Beamline at the CLS: Commissioning Results. *Nucl. Instruments Methods Phys. Res. Sect. A Accel. Spectrometers, Detect. Assoc. Equip.* **2007**, *582*, 96–99.

(59) Hitchcock, A.P., 2017. aXis2000 is written in Interactive Data Language (IDL). It is available free for non-commercial use from http://unicorn.mcmaster.ca/aXis2000.html.

4.7 Acknowledgements

K.G. and A.P.H. acknowledge support from the Natural Sciences and Engineering Research Council of Canada (NSERC) Discovery Grant program. X.W is supported by an Ontario Trillium Scholarship. Electron and atom probe microscopy was performed at the Canadian Centre for Electron Microscopy at McMaster University, a facility supported by NSERC and other governmental sources. STXM data was acquired with the ambient STXM at the Canadian Light Source, which is supported by Canada Foundation for Innovation, NSERC, the University of Saskatchewan, the Government of Saskatchewan, Western Economic Diversification Canada, the National Research Council Canada, and the Canadian Institutes of Health Research. We thank the CLS-SM beamline staff, in particular Dr. Jian Wang, for maintaining the instrument in top form. A.P and F.A.S acknowledge support from the BIOMATCELL VINN Excellence Center of Biomaterials and Cell Therapy, the Region Västra Götaland, an ALF/LUA grant, the IngaBritt and Arne Lundberg Foundation, the Dr. Felix Neubergh Foundation, Promobilia, the Hjalmar Svensson Foundation, and the Materials Science Area of Advance at Chalmers and the Department of Biomaterials, University of Gothenburg.

4.8 Supporting Information

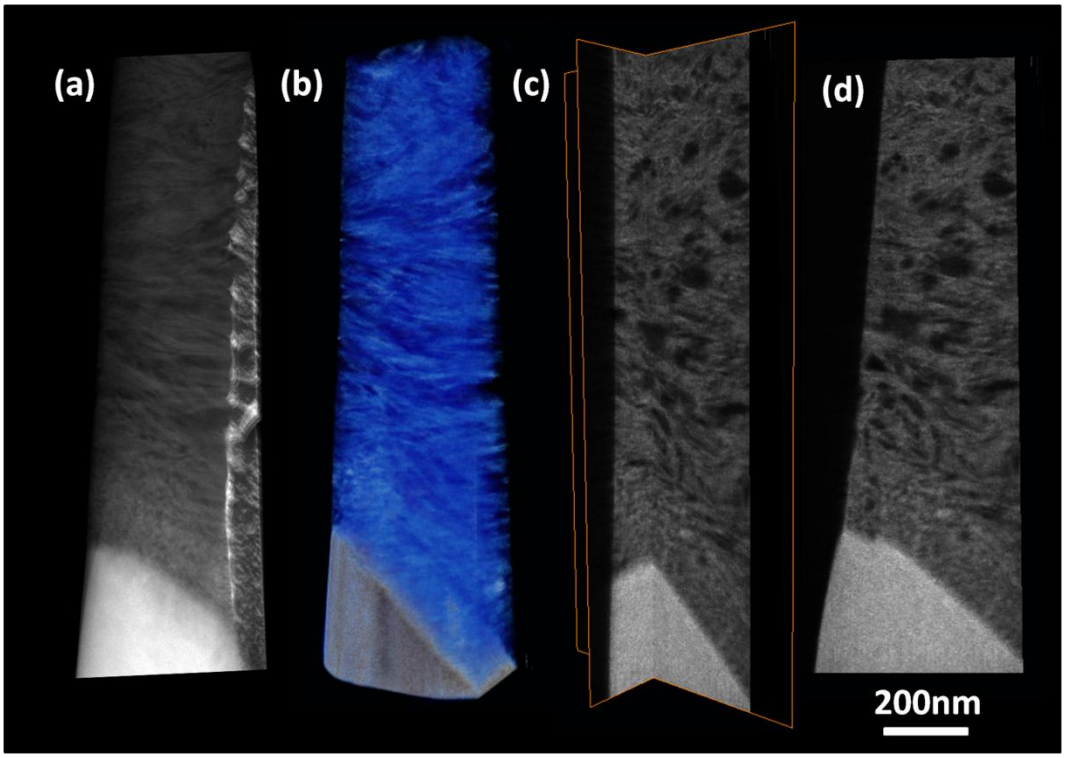

Supplementary Figure 4-1. On-axis electron tomographic reconstruction of the implant-bone interface. (a) 2D HAADF-STEM image of the bone-implant interface. (b) 3D renderings in color, and orthogonal slices through the reconstructed volume in the (c) XY, and (d) YZ planes.

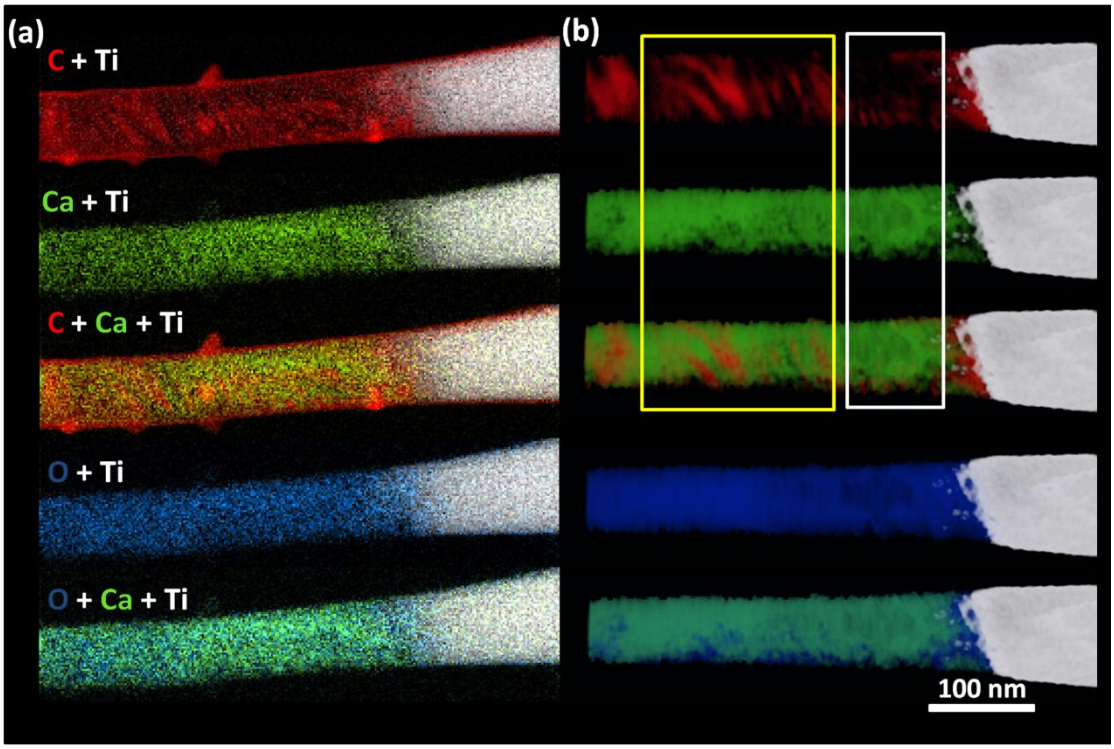

Supplementary Figure 4-2. On-axis EELS tomography of the bone-implant interface. (a) Representative EELS elemental distribution 2D maps from the 0 ° tilt angle for elements present in bone and at the bone-implant interface. (b) The corresponding 3D reconstructed elemental volumes from EELS maps acquired over a tilt range of ±70 °. The yellow box highlights the mature bone region with ordered collagen fibrils and the white box highlights the transition layer bonding to implant.

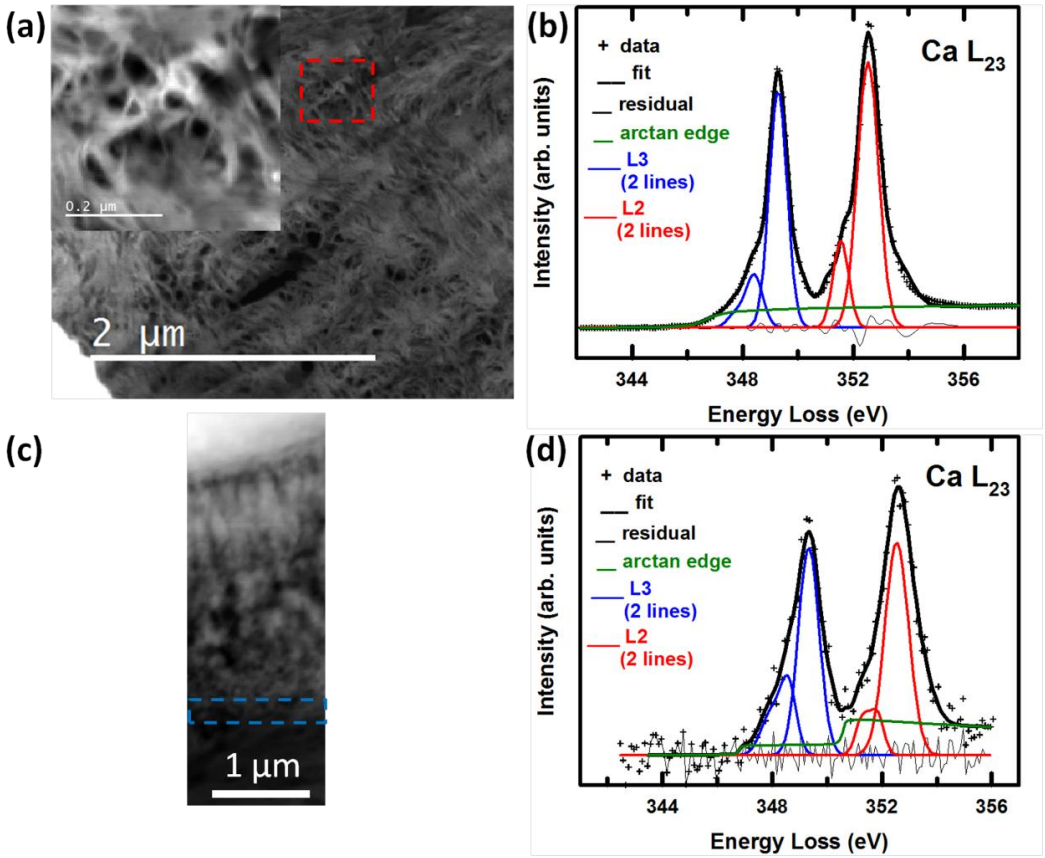

Supplementary Figure 4-3. ELNES of Ca-$L_{2,3}$ from bone (a, b) and interface (c, d). The peaks are deconvoluted into four peaks by Gaussian fitting.

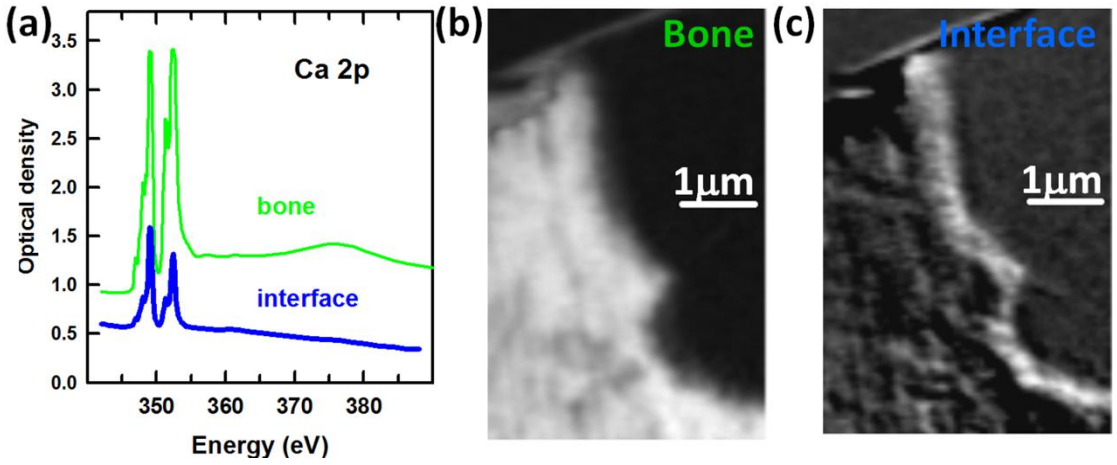

Supplementary Figure 4-4. STXM-XANES at the Ca 2p edge. (a) Ca 2p spectra of bone and the interface extracted from the Ca 2p stack. Component maps of (b) bone and (c) interface derived from a fit of the spectra of (a) to the Ca 2p stack after excluding images at the energies of peak saturation.[1] While most of the Ca 2p signals were absorption saturated, changes in the unsaturated subsidiary peaks (seen at 348 eV and 351 eV) at the interface allowed differentiation of an interface component

from unsaturated bone calcium. The interface spectrum was extracted from the interface region and 40% of bone signal was subtracted.

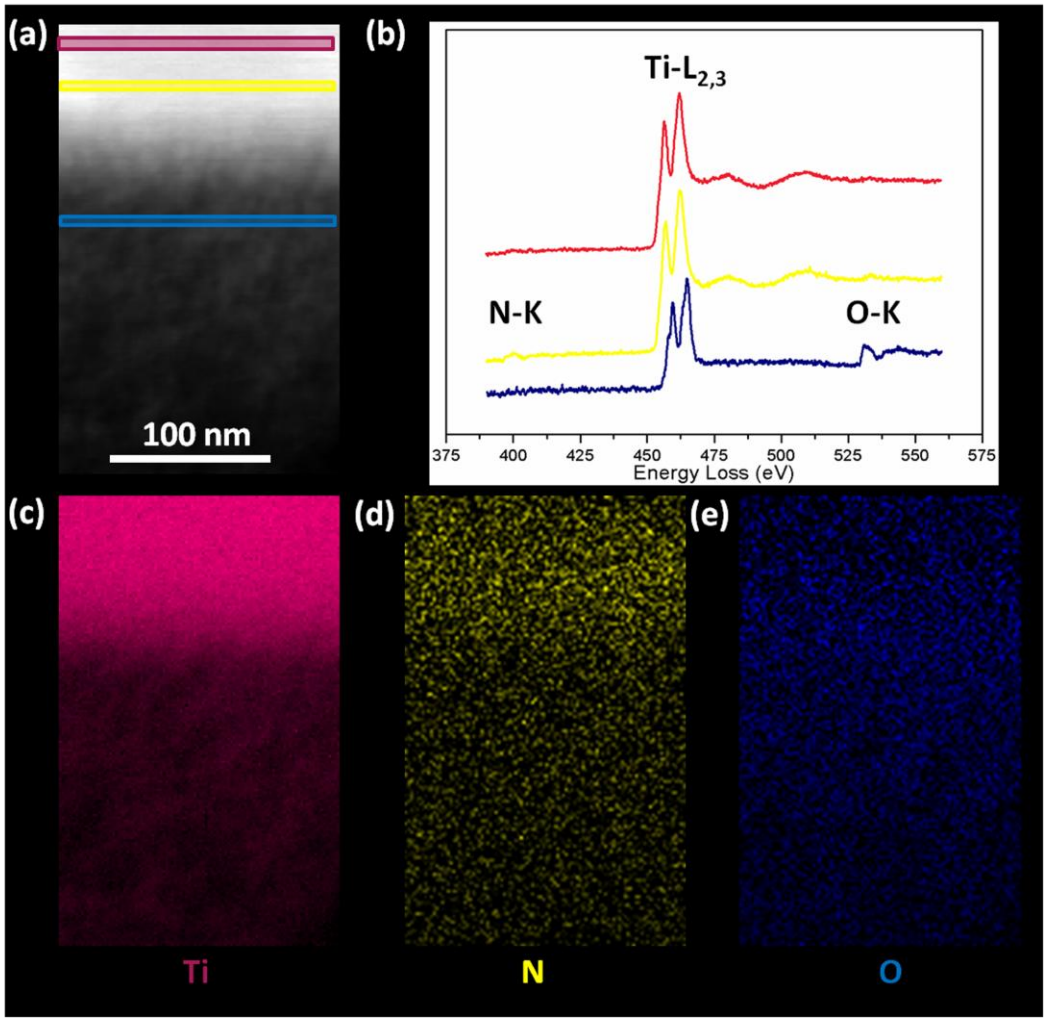

Supplementary Figure 4-5. Spatially-resolved EELS spectra and elemental distribution maps of native Ti implant. (b) Spatially-resolved EELS spectra extracted from regions marked in the HAADF STEM image (a) by red, yellow and blue rectangles. In the red spectrum (bulk Ti region), the Ti $L_{2,3}$-edge is clearly visible. In the yellow spectrum (the start of titanium oxide region), both Ti $L_{2,3}$-edge and N K-edge are discernible. In the blue spectrum (the surface oxide region), both Ti $L_{2,3}$-edge and O K-edge are detected. (c-e) Complementary EELS elementary distribution maps. The N-rich layer can be discerned from (d).

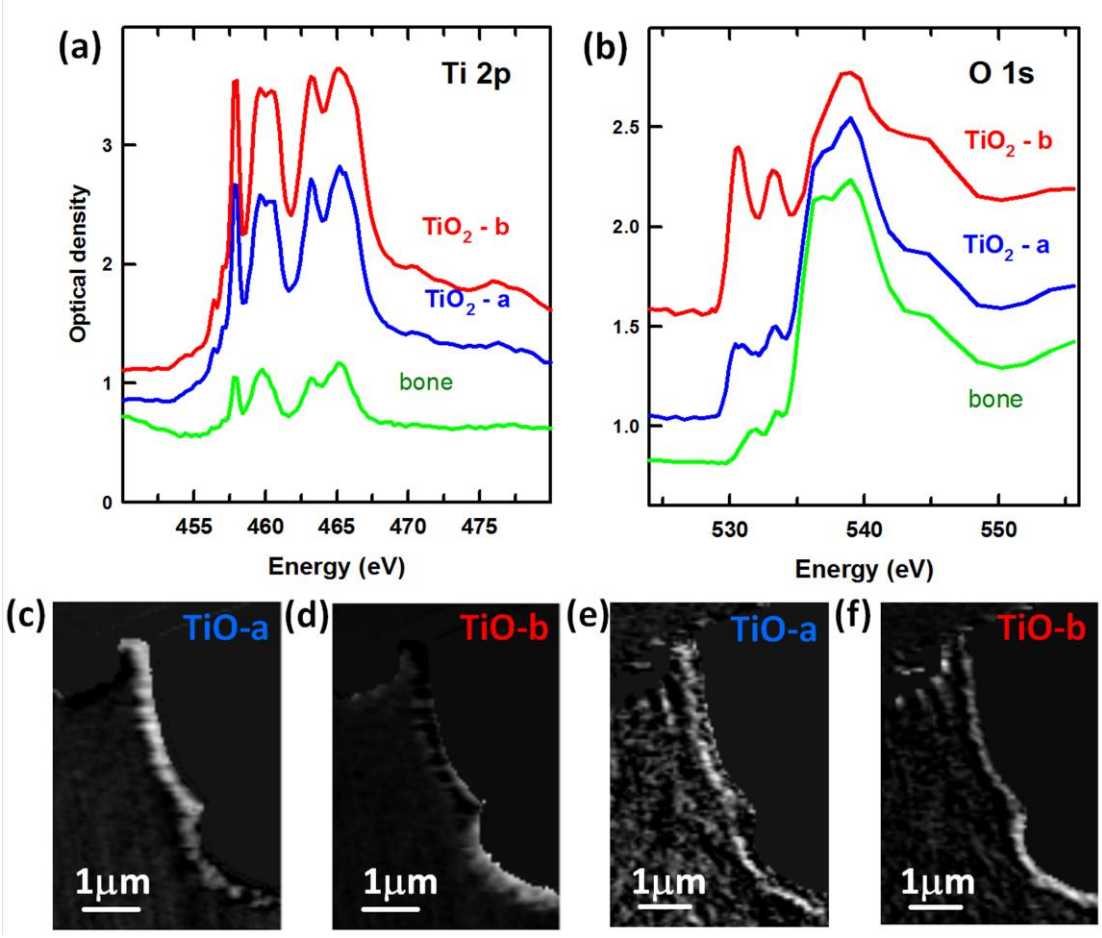

Supplementary Figure 4-6. STXM-XANES at the Ti 2p and O 1s edges. (a) Ti 2p spectra of two differentiable TiO_2 species, extracted from the Ti 2p stack, and that of the bone region. (b) O 1s spectra of two differentiable TiO_2 interface species and bone. Component maps of (c) TiO-a (d) TiO-b, from Ti 2p stack, and (e) TiO-a (f) TiO-b, from O 1s stack. The signal from the main Ti implant region is saturated throughout the Ti 2p region. The Ti-L_{23} spectra of the interface are partially saturated but the TiO_2-a and TiO_2-b signals are clearly differentiable. The O 1s signals are unsaturated, except in the thick part of the implant. The characteristic Ti oxide O 1s signatures complement the Ti 2p results, allowing differentiation and spectral characterization of two interface components. The absorption by main implant Ti metal signal is grossly saturated, and has been masked so as to not obscure the analysable interface and bone signals.

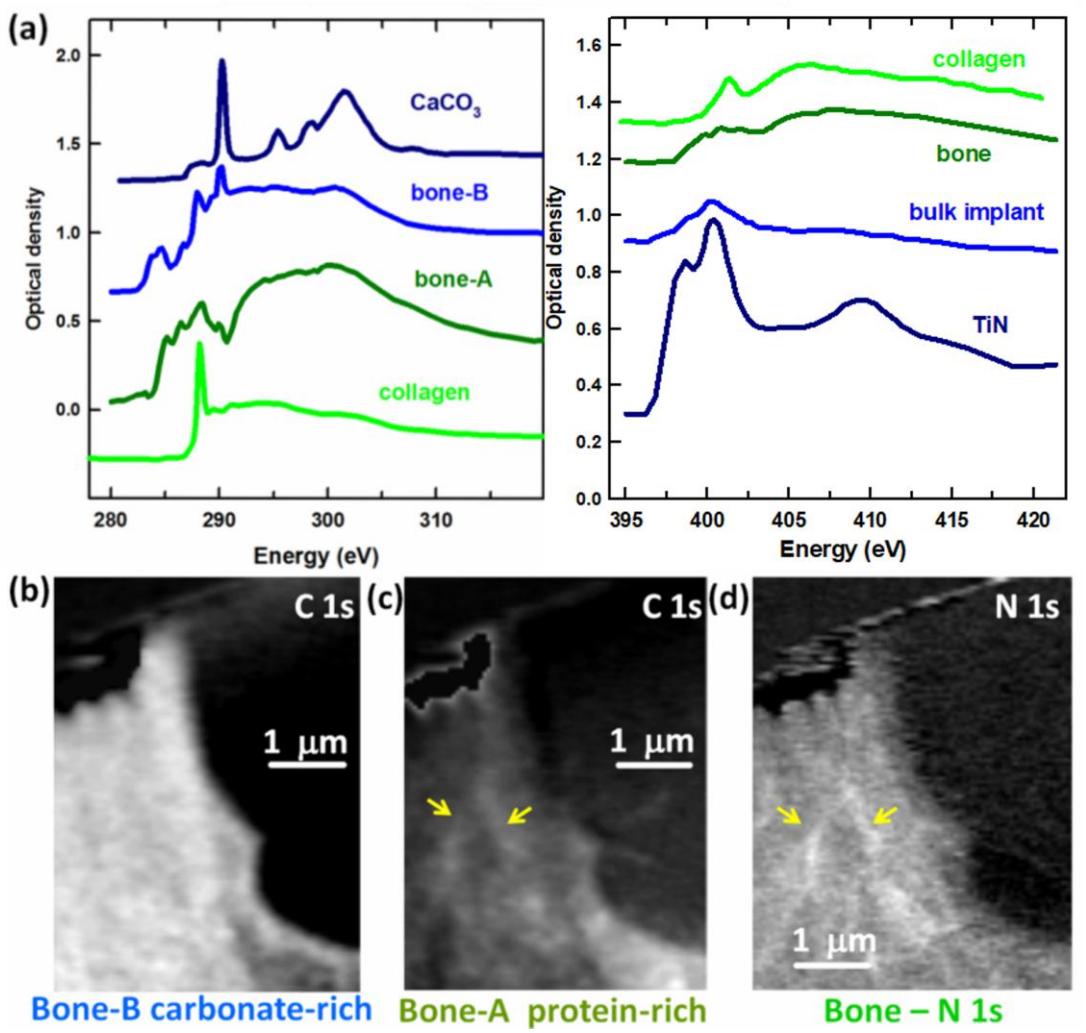

Supplementary Figure 4-7. STXM-XANES at the C 1s and N 1s edge. (a-d) Analysis of C 1s stack: (a) (left) Comparison of spectra of two distinct components in the bone region, extracted from the C 1s stack compared to reference spectra of $CaCO_3$ and collagen. The stack spectra are on the indicated OD scale while the $CaCO_3$ and collagen spectra are offset, rescaled. (right) N 1s spectra of bone, bulk implant and the TiN layer (with 0.7 OD subtracted) extracted from the N 1s stack, compared to the N 1s spectrum of collagen (offset, rescaled). Component maps of (b) C signal from carbonate containing species (Bone-B), (c) C signal from non-carbonate species (Bone-A), (d) Map of bone-N 1s signal from collagen in bone. The carbonate containing species might be the mineral components (carbonated hydroxyapatite) of bone and the non-carbonate species might be the collagen. The carbonate-rich region (c) overlaps with the N rich region (d) (highlighted by yellow arrows), which provides further evidence. The N 1s map of the TiN layer is presented in Figure 4-5.

References

(1) Hanhan, S.; Smith, a. M.; Obst, M.; Hitchcock, a. P. Optimization of Analysis of Soft X-Ray Spectromicroscopy at the Ca 2p Edge. *J. Electron Spectros. Relat. Phenomena* **2009**, *173*, 44–49.

Chapter 5 Biomineralization of Calcium Phosphate Revealed by *in situ* Liquid-Phase Electron Microscopy

---

In Chapter 5, the project design was performed by myself with discussion and advice from Dr. Kathryn Grandfield and Dr. Leyla Soleymani. *In-situ* liquid cell TEM experiments were performed by Jie Yang and myself. *Ex-situ* biomineralization experiments were performed by myself. Dr. Danielle Covelli performed XPS experiments. Dr. Carmen Andrei aided with EELS and *in situ* experiments. All data were analyzed by myself and co-authors. The manuscript was drafted and edited to the final version by myself, Jie Yang, Dr. Kathryn Grandfield and Dr. Leyla Soleymani.

Biomineralization of Calcium Phosphate Revealed by *in situ* Liquid-Phase Electron Microscopy

Xiaoyue Wang[1†], Jie Yang[2†], Carmen Andrei[3], Leyla Soleymani[2,4*], Kathryn Grandfield[1,2*]

[1.] Department of Materials Science and Engineering, McMaster University, Hamilton, Canada.
[2.] School of Biomedical Engineering, McMaster University, Hamilton, Canada.
[3.] The Canadian Centre for Electron Microscopy, McMaster University, Hamilton, Canada.
[4.] Department of Engineering Physics, McMaster University, Hamilton, Canada.

5.1 Abstract

Calcium phosphate (CaP) biomineralization is essential to the formation of bones and teeth, and other pathological calcifications. Unravelling the mechanism of CaP nucleation and growth contributes significantly to understanding diseases caused by pathological mineralization, and also to designing biomimetic materials with suitable properties. Recently, CaP was proposed to mineralize following a non-classical crystal growth pathway of pre-nucleation cluster aggregation. However, all observations have been based on *ex-situ* studies which are not sufficient evidence to prove the existence of this dynamic formation process. The advent of liquid-phase transmission electron microscopy (LP-TEM) allows for recording dynamic processes in liquid. Here, by using this real-time imaging technique, we present the first direct real-time evidence to demonstrate that CaP mineralization from simulated body fluid occurs by particle attachment, shown with nanoscale spatial resolution and sufficient temporal resolution. This work lays the foundation to investigating mineralization in other relevant biological systems in humans and vertebrates.

Keywords
calcium phosphate, *in situ,* liquid-phase transmission electron microscopy, biomineralization

[†]These authors contributed equally to this work.
* Correspondence and requests for materials should be addressed to K.G. or L.S. (Email: kgrandfield@mcmaster.ca, soleyml@mcmaster.ca).

5.2 Introduction

Biominerals are diverse natural minerals formed by living organisms. Their elaborate hierarchical structure, distinctive mechanical properties and varied physiological functions have motivated decades of research on their mineralization processes.[1,2] Calcium phosphates (CaP) are one of the most highly researched classes of biominerals, for the reason that the carbonated calcium phosphate apatite crystal is the essential mineral component of both bones and teeth of vertebrates.[3] Also, CaP deposition plays an important role in several pathological calcifications (e.g. arteriosclerosis, and physical calculus).[4–6] Therefore, understanding the mineralization process of CaP will aide in unveiling biomineralization mechanisms of healthy tissues such as bone, dentin and cementum, pathological calcifications (e.g. kidney stones), and also contribute towards research in applied sciences related to human health, such as the development of biomimetic materials and realization of mineralization mechanisms toward synthetic implant systems.[5]

Currently, the mechanism of CaP nucleation and growth is not fully understood. Based on Cryo-TEM[7] and Atomic Force Microscopy (AFM) studies[8], CaP was suggested to mineralize through complex pathways involving pre-nucleation cluster aggregation, sequential morphological transformations, and finally traversing into the crystalline phase.[7–9] Amorphous calcium phosphate (ACP) has been reported as the transient phase in both *in vivo* and *in vitro* studies.[10–12] It has been proposed that the existence of ACP pre-nucleation clusters decreases the energy barrier to nucleation and enables biominerals, such as CaP, to mineralize following a non-classical crystal growth process defined as crystallization by particle attachment.[13] In this process, the pre-nucleation particles, which are regarded as building blocks, are initiated from the solvated state and aggregate with each other to form clusters with chain-like or branched morphology. These pre-nucleation particles could vary from multi-ion complexes to nano-crystals in different mineralization systems.[13] Although these chain-like or branched morphologies

of the formed particles captured at defined time points provide important evidence to infer mineralization by attachment-based growth,[7,8] they alone are not sufficient evidence to prove the existence of this dynamic formation process. However, most studies on crystallization by particle attachment are still based on these *ex-situ* observations of crystals made after the pathway of initial nucleation.[9] Therefore, the need arises for a technique to render real-time observation of this dynamic process with nanoscale spatial resolution and necessary temporal resolution.[13–15]

Liquid-phase transmission electron microscopy (LP-TEM), with the ability to record events in confined liquid between two electron-transparent membranes with nanoscale spatial resolution and real-time temporal resolution,[16,17] is a promising technique to image dynamic nucleation and growth process of CaP. This approach has been used to study the nucleation and growth of $CaCO_3$ [13,14,18] and provided direct experimental evidence for the existence of indirect formation pathways through the transformation of amorphous or crystalline precursors.[15] Also, the dynamic process of calcium ions binding to biopolymers in the formation of metastable amorphous calcium carbonate was recorded *via in situ* LP-TEM observation.[14] Looking beyond nucleation mechanisms of CaP, the functions of non-collagenous proteins (NCPs)[19] and the collagen matrix[20,21] on crystal nucleation and subsequent growth are also poorly understood. Therefore, *in situ* TEM research on CaP nucleation and growth could lay a foundation for applying LP-TEM techniques to explore these unsolved issues of bone biomineralization.

In this study, we present the first real-time imaging of CaP nucleation and growth with *in situ* LP-TEM, which provides direct evidence to demonstrate that CaP mineralization occurs by particle attachment.

5.3 Results and Discussion

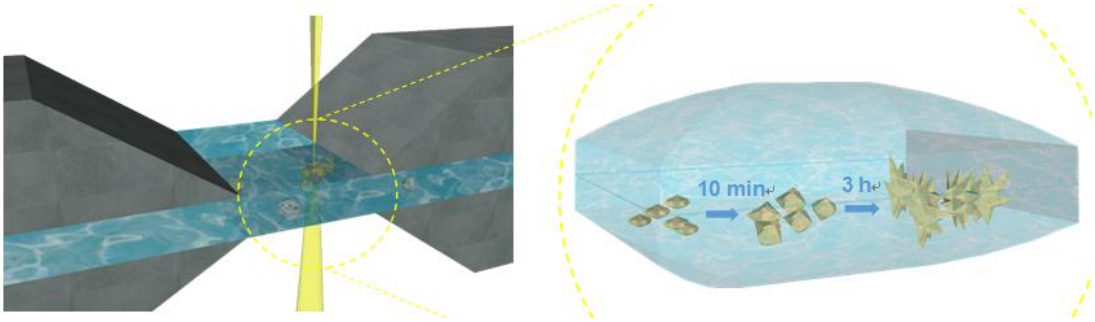

Figure 5-1. Schematic of the *in situ* liquid cell in scanning TEM and CaP mineralization process.

In order to perform real-time imaging inside the TEM, an *in situ* scanning LP-TEM system was used to visualize the mineralization process, as shown in the schematic drawing in Figure 5-1. The *in situ* system, composed of two overlapping silicon nitride membranes on silicon chips, confines a limited amount of solution to form a miniaturized cell. The *in situ* observations were conducted by scanning the focused electron beam across an area of interest where mineralization occurred in the solution, and capturing video of these events.

The free radicals generated through radiolysis of aqueous solution, such as hydrated electrons, $H^{\cdot}$, $OH^{\cdot}$, and so on, can interact with existing active species from solution as reducing and oxidizing agents. These reactions are determined by the concentration of the generated radicals, which are further dependent on the conditions of the microscope and liquid cell, including beam dose rate, solution composition, and temporal and spatial concentration evolution by diffusion and reaction.[22] It has been reported that beam-induced species below a certain concentration result in negligible radiolysis-related reactions.[23] For the system in this study, having a solution with a stable pH of 7.4, a beam dose rate of 21 electrons/frame.nm^2 was identified to reduce the beam effect and maintain sufficient spatial resolution at the same time. Furthermore, the beam dose chosen for this *in situ* study was much lower than the threshold value of beam induced

crystallization reported in previous studies[24]. In addition, the presence of a buffer solution may have contributed to the maintenance of a stable pH which helped to reduce the chemically active species interacting with calcium and phosphate ions contained in the solution to produce beam-induced crystals.

The membranes between which liquid is encapsulated have been reported to bulge[25] due to pressure difference between the liquid inside the cell and the vacuum environment in TEM, as shown encircled in Figure 5-1. This bulge contributes to the reduction of the resolution based on an increased thickness of the liquid layer and multiple scattering of the electron beam. In order to reduce the liquid layer thickness and consequently enhance the resolution, the thinnest liquid layer was used (50 nm spacers) and imaging was always preferred at the corner of a liquid cell where the bulging is minimal. In this study, the bottom chip was patterned with micro-wells (400 μm x 200 μm each well), which helped to decrease interference among each individual micro-well by confining the generated radical species to each well.[22, 25, 26] Based on the *in situ* setup shown in Figure 1, a series of *in situ* studies were performed and followed by characterization and analysis of the products formed.

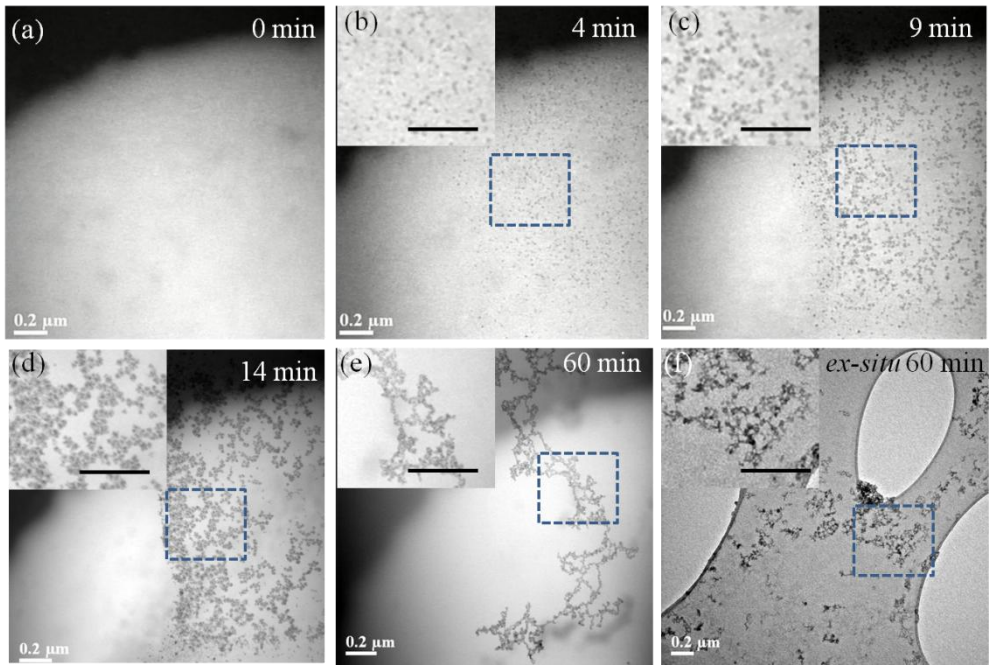

Figure 5-2. *In situ* BF-STEM images showing initial nucleation and growth of CaP over 60 min. (a–d), continuous mineralization from 0–14 min, showing the nucleation and growth of CaP particles (e), final branched particle morphology after 60 min (f), BF-TEM image of ex-situ mineralization with similar resulting particle size and morphology after the same growth time. The scale bars in the insets represent 200 nm.

Real-time observation of the morphological evolution of CaP mineralization

With the help of *in situ* scanning LP-TEM, the CaP nucleation and mineralization process was recorded by bright-field (BF) scanning TEM (STEM) images with time-resolved and nanoscale spatial resolution (Figure 5-2). After a delay of around 2 min, small particles appeared and began increasing in quantity. At around 4 min (Figure 5-2 (b)), these particles were clearly discernable and their average diameter measured 10 nm. These particles had the ability to move and aggregate with each other in solution (Supplementary Video 1). Initially, they aggregated with the nearby particles to randomly generate branched particle assemblies (Figure 5-2 (c)). After the branched assemblies were formed, smaller particles continued to move towards the assemblies and aggregate. With increasing time, these branched assemblies increased in size, and at 14 min aggregated sphere-like particles were obvious (Figure 5-2 (d)). In order to limit the

electron beam dose exposure to the *in situ* mineralization solution, we blocked the electron beam by closing the microscope column and let the *in situ* mineralization continue without electron beam exposure. The column was then reopened, and a single image was taken at 60 minutes (Figure 5-2 (e)), showing the final branched assemblies formed during this time period. We performed a beam-blank comparison to validate that the *in situ* morphology observations were not solely artifacts of the electron beam. A bright-field TEM image of an *ex-situ* synthesized and mineralized sample after 60 minutes is shown in Figure 5-2 (f) with similar particle size and branched assembly morphology.

The initial morphology evolution observed *in situ* agrees well with results of cryo-TEM studies on similar CaP systems.[7,21] In those studies, pre-nucleation clusters of calcium triphosphate ions were proposed to exist as the nanometer-sized building blocks for CaP, which decreased the energy barrier for nucleation. These pre-nucleation precursors can aggregate into branched polymeric structures. However, cryo-TEM investigations can only infer the morphology evolution according to images at segregated time points and is unable to record the dynamic mineralization process. In our *in situ* study, we observed in real-time the nucleation, movement, and morphology evolution of CaP nanoparticles, which provides direct evidence to demonstrate the active mobility of CaP nucleation clusters and supports that CaP mineralizes by particle attachment. It has been suggested that the CaP pre-nucleation precursor is the initial phase formed during the bone mineralization process to be delivered into the extracellular matrix.[10,19] Here, real-time recording with sufficient temporal and spatial resolution showed the active mobility of initial CaP clusters, which also supports the possibility of their movement towards collagen fibrils in aqueous environments for their eventual mineralization. This work lays the foundation for further investigation of the mediating functions of the extracellular matrix, as well as non-collagenous proteins on CaP mineralization *in situ*.

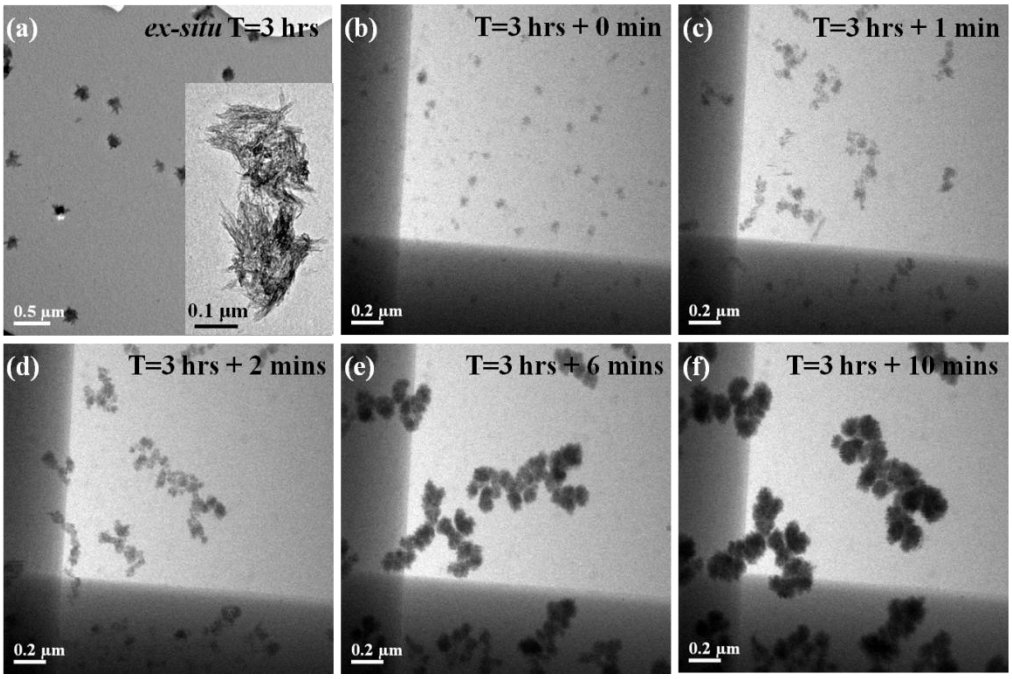

Figure 5-3. CaP growth and morphology after 3 h pre-mineralization. (a), BF-TEM images of flake-like particles that resulted after ex-situ mineralization on E-chips without exposure to the electron beam, (b–f), corresponding *in situ* BF-STEM images showing CaP growth progression after 3 h, and the growth of dark particles with roughened borders.

In addition to initial nucleation and growth, it is also critical to investigate the particle morphology after longer growth times, since CaP biomineralization involves sequential morphological transformations which could serve as indications of phase changes.[8,9] In *in vitro* CaP mineralization studies, the morphology of ribbon-like structures was observed after 3 hours[8,27], also noted here in a similar *ex-situ* experiment of Figure 5-3 (a) flake-like particles developed. This phase of CaP mineralization was also studied here by another representative *in situ* TEM experiment shown in Figure 5-3. In this experiment, the silicon nitride microchips patterned with discrete micro-wells were used. After 3 hrs the electron beam was moved to a new micro-well that had not experienced electron beam exposure and the images in Figure 5-3 (b-f) were captured. This enabled the capture of mineralization events after the initial nucleation and growth period. While this approach assumes that the liquid is confined to each separate micro-well, and therefore,

at time t=3hrs represents growth that was not beam induced, recent works have shown that radiolysis products are largely beam-confined[22] and unlikely to effect a neighboring micro-well. Now, sphere-shaped aggregates that were larger than those formed during initial nucleation under electron beam exposure at time zero were observed (Figure 5-3 (b)), which during further real-time TEM imaging (Figure 5-3 (c-f)), grew into aggregated assemblies (Figure 5-3 (c)) with roughened borders arising from their needle-like nature, which grew darker (Figure 5-3 (d)), and larger while they rotated within the liquid (Figure 5-3 (e) and (f)). After around 6 minutes, the aggregates still had the ability to move by rotation in the liquid, and by 10 minutes further darkened and grew slightly due to what appears to be conventional crystal growth. Since the particle morphology from *ex-situ* experiments, shown in Figure 5-2 (f) and 5-3 (a), so closely matches the events shown *in situ* after 1 hr and 3 hrs, respectively, we can assume that the beam effects on the mineralization pathway are not substantial.

Based on our real-time *in situ* investigation of this dynamic process, the early mineralization of CaP can be divided into several stages. Initially, nanoscale particles appeared after around 2 minutes, these continued to aggregate to form branched assemblies within 1 hr. In other works, these assemblies were proposed to directly assemble into ribbon aggregates[8]. Here, we see this transformation after 3 hrs, where the formation of similar needle-like aggregates occurs by particle attachment, and subsequent continued growth takes place by seemingly conventional methods.

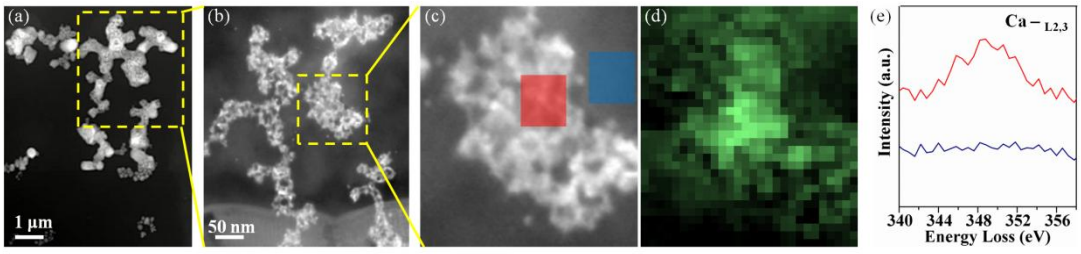

Figure 5-4. *Post-situ* characterization of the *in situ* synthesized particles. (a–c), HAADF STEM

images of (a), the *in situ* region of interest and (b), the same area once the silicon nitride microchips have been opened, and shown at (c), higher magnification and as (d), an EELS Ca-map as extracted from the *post-situ* (e), EELS spectra of the Ca-$L_{2,3}$ edge which demonstrates these particles are Ca-based. The Ca $L_{2,}$3-edge was identified inside mineralized particles (red), and absent in the surrounding regions (blue).

Post-situ correlative chemical composition analysis

Due to the relatively thick liquid layer in LP-TEM compared to conventional TEM specimens, spectroscopy characterization *in situ* is a challenge. Here, we exploited several so-called *post-situ*, or post *in situ* correlative spectroscopy characterization approaches to probe the mineralization products, specifically X-ray photoelectron spectroscopy (XPS) and electron energy loss spectroscopy (EELS) on the removed *in situ* chips. After the *in situ* experiment presented in Figure 5-1, the silicon nitride microchips were removed from the liquid TEM holder and dried for *post-situ* characterization *via* XPS. XPS (Supplementary Figure 5-1) showed the existence of Ca and P, and the high-resolution spectrum of P contains the peak at 133.89 eV which matches with the photoelectron line of P in CaP. In addition, the quantitative elemental ratio of XPS analysis showed the Ca/P is ~0.67, which has a nice agreement with the calculated Ca/P ratio range of 0.55 to 0.75 in other studies[8]. This same sample was then probed by EELS, where Figure 5-4 (a) and (b) highlight the region of interest *in situ* and after drying, respectively. An EELS spectrum image (Figure 5-4 (d)) and extracted Ca-$L_{2,3}$ edges (Figure 5-4 (e)) confirm the presence of Ca inside mineralized particles and absence in the surrounding regions which demonstrates these particles are Ca-based. The correlative *post-situ* chemical analyses by XPS and EELS provide strong evidence that the *in situ* mineralized particles are CaP-based. Also, the Ca/P ratio from the XPS quantitative data reported as 0.67 from the one-hour *in situ* mineralized sample suggests that the phase of these branched assemblies is not amorphous calcium phosphate (ACP) whose Ca/P ratio is 1.5. ACP was considered as the nanometer-sized building blocks of CaP in other studies.[8] Due to the large liquid layer, and small particle size, obtaining a

reliable diffraction pattern *in situ* to determine the exact phase of the CaP formed was not possible.

5.4 Conclusions

For the first time, the real-time observation of CaP mineralization was recorded, which is a direct demonstration that CaP initially mineralizes by particle attachment. Complementary *in situ*, *post-situ* characterization and *ex-situ* beam-blank experiments were designed to support this claim. According to *post-situ* TEM-EELS and XPS analysis, the *in situ* mineralized particles were confirmed to be CaP-based. The samples mineralized in *ex-situ* beam-blank experiments follow similar morphologies as *in situ* samples, which validates that the *in situ* morphological observations were not solely artifacts of electron beam dose. This study lays the foundation for further investigation of CaP biomineralization involving more complex organic-inorganic physiological interactions.

5.5 Materials and Methods

Mineralization solution The CaP mineralizing solution was prepared according to Lausch and co-workers[20,28] who have demonstrated selective remineralization on demineralized murine dentin with this solution. The solution was made up of two parts: 1) a phosphate solution (9.5 mM Na_2HPO_4 (Sigma-Aldrich, USA) in 125 mM NaCl, 50 mM Tris (Sigma-Aldrich, USA), pH 7.40), and 2) a calcium solution (1.7 mM $CaCl_2$ in 125 mM NaCl, 50 mM Tris, pH 7.40). All reagents were purchased from Sigma Aldrich and dissolved in Milli-Q water. These two solutions were mixed and filtered through a 0.2 μm acrodisc syringe filter right before sealing in the liquid TEM holder for *in situ* experiments or placing in the beakers for *ex-situ* experiments at room temperature.

***In situ* STEM** The *in situ* TEM holder (Poseidon 500, Protochips Inc., Raleigh, NC,

USA) used in this study contains a liquid cell placed at the holder tip. Two microfabricated silicon nitride microchips with 50 nm silicon nitride membranes were sealed inside the liquid cell and *in situ* imaging was performed by electrons passing through the overlapped silicon nitride membranes. A small amount (2 μL) of CaP mineralizing solution was put in between the two membranes, one of which was patterned with microwells, which assists in maintaining a relatively stable solution during the *in situ* mineralization process, and reducing beam effect interference between the individual microwells. The E-chips used in this study were commercially available bottom large chips (ETP-42A1, Protochips Inc., Raleigh, NC, USA) containing an 8 x 16 array of 10 μm x 10 μm microwell on a 400 μm x 200 μm SiN membrane and top chips of 300 μm x 90 μm SiN membrane without spacers (ECB-39A, Protochips Inc., Raleigh, NC, USA). Real-time imaging was performed using a JEOL 2010F TEM operated at 200 kV. Bright-field scanning transmission electron microscopy (BF-STEM) mode was used under beam dose of 2.198 x 10^3 e/Å^2 s. *In situ* images were acquired using DigiScan II (Gatan, model 788) unit with a BF detector with time resolution of 0.555 s/frame. The whole *in situ* process was recorded by a CCD camera and series of *in situ* images were either extracted from the *in situ* video or captured every 4 s by blanking the electron beam in between.

***Post-situ* and *ex-situ* TEM** To confirm mineralization products formed were similar to those formed without the interaction of any electron beam, so-called *ex-situ* experiments were performed completely outside of the TEM. To confirm 1 h experiments, mineralization products were acquired by dropping dispersed mineralized solution after 1 h onto carbon-coated TEM copper grids followed by immersion in methanol to halt any further particle development. For the confirmation of products after 3 h under confinement, the same amount of CaP mineralization solution (0.2 μl) was sealed inside the *in situ* TEM liquid cell for 3 h, but not placed under the electron beam. The E-chips

were then taken out, washed with methanol to terminate further mineralization, and viewed in the TEM.

After the *in situ* experiment, the E-chips were removed from the liquid TEM holder, separated and then dried for further *post-situ* characterization. The *post-situ* experiments were conducted sequentially, with XPS performed first (detailed below), and EELS performed after mounting the sample to a molybdenum grid to mount on a standard double-tilt holder. As for all experiments, a JEOL 2010F TEM with the accelerating voltage of 200 kV was employed to characterize the *post -situ* mineralized samples on the dried E-chips, as well as the *ex-situ* mineralized samples above in both TEM and STEM bright field imaging modes, and by STEM-EELS. Principle component analysis (PCA) was used to decrease noise in the Ca elemental distribution EELS map.

X-Ray Photoelectron Spectrometry (XPS) Both *in situ* mineralized samples on the dried E-chips and *ex-situ* mineralized samples on TEM grids were characterized by an imaging and scanning X-ray photoelectron spectrometer (PHI Quantera Ⅱ, Physical Electronic, MN). The time-dependent *ex-situ* mineralized samples were prepared by spin-coating dispersed mineralized solution onto cleaned silicon wafer substrates and then immersing them in methanol to wash away NaCl. All the selected regions of interest were scanned by monochromated Al Kα (280 eV) with 5 sweeps for 200 micron beam (50 power) and 20 sweeps for 7.5 micron beam (0.8 W power). 55 eV pass energy scanning with 200 micron beam and 120 sweeps was used for the P1s high resolution spectra. Dual beam neutralization was used to prevent samples from charging. Calibration was done by calibrating to a clean piece of silver foil.

5.6 References

1. Weiner, S. & Dove, P. M. An overview of biomineralization processes and the problem of the vital effect. *Rev. Mineral. …* **54,** 1–29 (2003).
2. Addadi, L. & Weiner, S. Biomineralization: mineral formation by organisms. *Phys. Scr.* **89,**

98003 (2014).

3. Dorozhkin, S. V. Calcium orthophosphates in nature, biology and medicine. *Materials (Basel).* **2,** 399–498 (2009).
4. Guangbin, L. *et al.* Spontaneous Calcification of Arteries and Cartilage in Mice Lacking Matrix GLA Protein. *Nature* **386,** 78–81 (1997).
5. Dorozhkin, S. V & Epple, M. Biological and medical significance of calcilum phosphates. *Angew. Chemie Int. Ed.* **41,** 3130–3146 (2002).
6. Yiu, A. J., Callaghan, D., Sultana, R. & Bandyopadhyay, B. C. Vascular Calcification Stone Disease: A new look towards the mechanism. *J. Cardiovasc. Dev. Dis.* **2,** 141–164 (2015).
7. Dey, a *et al.* The role of prenucleation clusters in surface-induced calcium phosphate crystallization. *Nat. Mater.* **9,** 1010–1014 (2010).
8. Habraken, W. J. E. M. *et al.* Ion-association complexes unite classical and non-classical theories for the biomimetic nucleation of calcium phosphate. *Nat. Commun.* **4,** 1507 (2013).
9. Van Driessche, A. E. S., Kellermeier, M., Benning, L. G. & Gebauer, D. *New Perspectives on Mineral Nucleation and Growth*. (Springer, 2017). doi:10.1007/978-3-319-45669-0
10. Nudelman, F., Lausch, A. J., Sommerdijk, N. a J. M. & Sone, E. D. In vitro models of collagen biomineralization. *J. Struct. Biol.* **183,** 258–269 (2013).
11. Mahamid, J. *et al.* Mapping amorphous calcium phosphate transformation into crystalline mineral from the cell to the bone in zebrafish fin rays. *Proc. Natl. Acad. Sci.* **107,** 6316–6321 (2010).
12. Boonrungsiman, S. *et al.* The role of intracellular calcium phosphate in osteoblast-mediated bone apatite formation. *Proc. Natl. Acad. Sci.* **109,** 14170–14175 (2012).
13. De Yoreo, J. J. *et al.* Crystallization by particle attachment in synthetic, biogenic, and geologic environments. *Science (80-.).* **349,** aaa6760-aaa6760 (2015).
14. Smeets, P. J. M., Cho, K. R., Kempen, R. G. E., Sommerdijk, N. A. J. M. & De Yoreo, J. J. Calcium carbonate nucleation driven by ion binding in a biomimetic matrix revealed by in situ electron microscopy. *Nat. Mater.* **14,** 394–399 (2015).
15. Nielsen, M. H., Aloni, S. & Yoreo, J. J. De. In situ TEM imaging of CaCO 3 nucleation reveals coexistence of direct and indirect pathways. *Science (80-.).* **218,** 213–218 (2013).
16. De Jonge, N. & Ross, F. M. Electron microscopy of specimens in liquid. *Nat. Nanotechnol.* **103,** 695–704 (2011).
17. Ross, F. M. Opportunities and challenges in liquid cell electron microscopy. *Science (80-.).* **350,** 1–9 (2015).
18. Verch, A., Morrison, I. E. G., Locht, R. Van De & Kr öger, R. In situ electron microscopy studies of calcium carbonate precipitation from aqueous solution with and without organic additives. *J. Struct. Biol.* **183,** 270–277 (2013).
19. Olszta, M. J. *et al.* Bone structure and formation: A new perspective. *Mater. Sci. Eng. R Reports* **58,** 77–116 (2007).
20. Lausch, A. J., Quan, B. D., Miklas, J. W. & Sone, E. D. Extracellular Matrix Control of Collagen Mineralization In Vitro. *Adv. Funct. Mater.* n/a-n/a (2013).
21. Nudelman, F. *et al.* The role of collagen in bone apatite formation in the presence of

hydroxyapatite nucleation inhibitors. *Nat. Mater.* **9,** 1004–1009 (2010).
22. Schneider, N. M. *et al.* Electron-Water interactions and implications for liquid cell electron microscopy. *J. Phys. Chem. C* **118,** 22373–22382 (2014).
23. Woehl, T. J. *et al.* Ultramicroscopy Experimental procedures to mitigate electron beam induced artifacts during in situ fluid imaging of nanomaterials. *Ultramicroscopy* **127,** 53–63 (2013).
24. Smeets, P. J. M., Cho, K. R., Kempen, R. G. E., Sommerdijk, N. a J. M. & De Yoreo, J. J. Calcium carbonate nucleation driven by ion binding in a biomimetic matrix revealed by in situ electron microscopy. *Nat. Mater.* **4193,** 1–6 (2015).
25. Holtz, M. E., Yu, Y., Gao, J., Abruña, H. D. & Muller, D. a. In Situ Electron Energy-Loss Spectroscopy in Liquids. *Microsc. Microanal.* **19,** 1027–1035 (2013).
26. Schneider, N. M. in *liquid cell electron microscopy* 140–163 (Cambridge, 2017). doi:10.1017/9781316337455.008
27. Nitiputri, K. *et al.* Nanoanalytical Electron Microscopy Reveals a Sequential Mineralization Process Involving Carbonate-Containing Amorphous Precursors. *ACS Nano* **10,** 6826–6835 (2016).
28. Deshpande A.S., B. E. Bio-inspired Synthesis of Mineralized Collage Fibrils. *Cryst Growth Des.* **8,** 3084–3090 (2008).

5.7 Acknowledgements

K.G. acknowledges financial support from the Discovery Grant program of the Natural Sciences and Engineering Research Council of Canada (NSERC). L.S. acknowledges financial support from the Natural Sciences and Engineering Research Council of Canada and the Canada Research Chair program. X.W. acknowledges support from the Ontario Trillium Scholarship. Electron microscopy was performed at the Canadian Centre for Electron Microscopy (CCEM), a facility supported by NSERC and other governmental agencies. Gianluigi Botton, scientific director of the CCEM, is gratefully acknowledged for his continued support and guidance.

5.8 Supporting Information

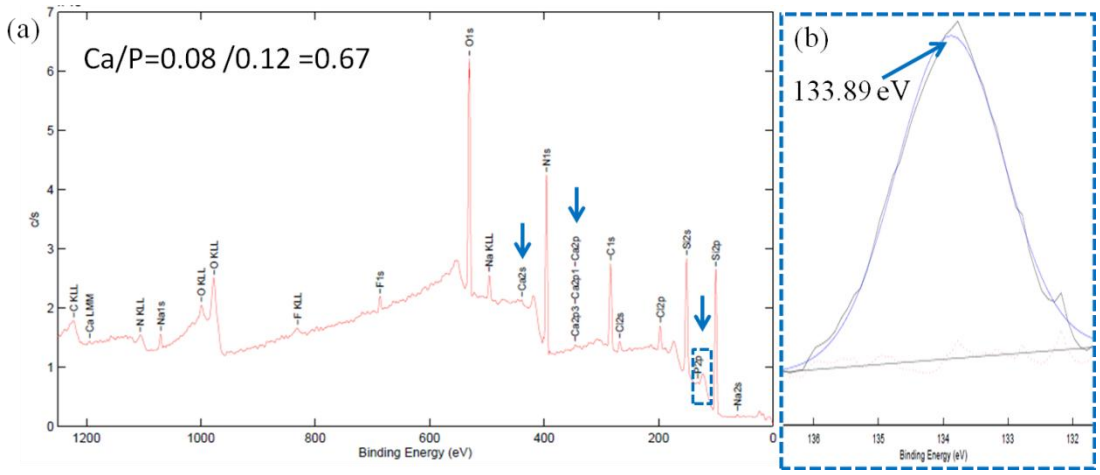

Supplementary Figure 5-1. The *in situ* synthesized particles are characterized by *post-situ* XPS. The deconvoluted P high energy resolution peak matches with the photoelectron line of 2p3/2 of P in CaP.

Chapter 6 Concluding Remarks

In this thesis, correlative multi-dimensional microscopy techniques have been applied to investigate the origins and distribution of calcium-based (i.e. inorganic) and carbon-based (i.e. organic) components at the bone-implant interface. Understanding these concepts are some of the key remaining questions needed to completely understand the mechanism of osseointegration. The morphological and chemical changes observed by these correlative characterizations revealed the existence of a transitional biointerphase at the bone-implant interface. This thesis also demonstrated the application of liquid-phase transmission electron microscopy (LP-TEM) to investigating the dynamic process of calcium phosphate (CaP) biomineralization so as to subsequently to understand the mechanism of bone formation and osseointegration. This thesis has explored the application of state-of-the-art advanced microscopy in mineralized biological samples while optimizing experimental strategies and this lays a foundation for future studies on biomaterials using these advanced techniques.

6.1 Key Findings and Contributions

The research objectives proposed in Chapter 1 were achieved, and the detailed key findings and contributions of this work are listed as follows:

1. The first application of on-axis electron tomography (ET) of human bone and laser-modified titanium implant interfaces was presented. By circumventing the missing wedge artifacts, this technique visualized a quantitative 3D reconstruction of the nanotopographies of the implant surface oxide layer and bone growth into these features.
2. The 3D visualization of human bone-titanium implant interface using on-axis ET (based on needle-shape samples) was compared with that by conventional single-axis ET (based on lamellar samples). The on-axis ET is capable of circumventing missing wedge artifacts, while the lamellar samples allow for a larger field of view of the

interface. Both ET techniques reveal useful and complementary information about the bone-implant interface, such as 3D visualization of nanoscaled features of implant surface oxide layer and bone growth into them.

3. Electron energy loss spectroscopy (EELS) tomography was applied for the first time to characterize the nanoscale elemental distribution at the human bone-implant interface in 3D. Both Ca and C were observed to distribute at the interface in immediate vicinity to the oxide layer of implant, while collagen fibrils were observed in close (~100nm) proximity. Also, the Ca at the interface was revealed to originate from amorphous calcium apatite (ACP) by electron energy-loss near-edge structure (ELNES), while that in bone was hydroxyapatite.
4. The atomic level 3D chemical mapping of human bone-implant interface was visualized with atom probe tomography (APT). Both Ca (representing bone mineral) and C (representing organic components) are shown in direct contact with the oxide layer at implant surface, which corroborates the observations from correlative EELS tomography. The gradient concentration change of Ca and Ti across the interface provides a vital piece of experimental evidence to the atomic continuum of osseointegration. This also involved exploration and optimization of APT experimental parameters and sample coating strategies for characterizing natural biomineral and biointerface samples.
5. Both APT and X-ray absorption spectroscopy (XAS) in soft X-ray scanning transmission X-ray microscopes (STXM) demonstrated the existence of a distinct N-rich layer between the oxide layer and Ti metal of the commercial pure titanium dental implant (BioHelix™). This N-rich region was considered to be formed during the laser modification of the implant surface in an ambient air environment. And the origin of N in this layer was identified as TiN by STXM X-ray absorption near edge structure (XANES).
6. This thesis presented the first correlative 4D chemical tomography study of a

bone-implant interface, including on-axis electron tomography, EELS tomography, and APT performed on the same sample. The correlative 4D tomography workflow based on the same needle-shape sample was established here, which is transferable to other applications in materials science or biological studies.

7. The first real-time observation of CaP nucleation and growth was recorded by using LP-TEM. This is direct experimental evidence to prove that CaP initially mineralizes via particle attachment. Also, *in-situ*, *post-situ* characterization and *ex-situ* beam-blank experiments were designed to support and complement each other.

Therefore, based on these observations, this thesis supports most closely, but not identically, the three-zone-structure at the bone-implant interface proposed by Albrektsson *et al*. As the first zone, both Ca and C were shown distributing intimately at the implant surface, but for the first time at the atomic level by APT. An intervening transition zone was defined as the second zone by EELS tomography observation, connecting the fibrillary mature bone and implant surfaces. The organized collagen fibrils, representing the mature bone structure, appeared 100 nm away from the implant surface, which also matched with the description of Albrektsson *et al.* of the third zone. However, this work also unveiled new information on the bone-implant interface based on the spectroscopic characterizations carried out. Specifically, the phase of Ca directly distributed at the implant interface was confirmed as amorphous calcium phosphate. However, the phase of C is still not fully understood and requires further spectroscopic studies to determine whether its origin is collagenous or proteoglycan-based as proposed in the other theories of osseointegration.

6.2 Future Work

In this thesis, correlative 4D tomography techniques have been explored and successfully applied to characterize the interface between human bone and a commercially pure

laser-modified titanium implant. The established workflow of correlative tomographies can be applied to study and evaluate other type of implants with different surface modifications, such as implants made of Ti6Al4V titanium alloy or titanium implants with mesoporous titania coatings doped with Ca or Sr. In this way, the general characteristics of the nanoscale chemical structure at bone-implant interfaces can be elucidated, which helps to understand the mechanism of bone growth onto different types of implant surfaces. Moreover, exploring these techniques on time-resolved animal studies would shed light on the dynamic process of bone formation at implant surfaces. This workflow would also be greatly advanced by the introduction of cryogenic sample preparation techniques, which avoids the need for potentially damaging fixation, dehydration and embedding procedures. Substantial technical development is still needed to enable cryogenic transfer between all the microscopes involved in this thesis.

Also, the phases of carbon-based (i.e. organic) components at the bone-implant interface are crucial evidence to unveil the osseointegration mechanisms, which was not fully investigated in this thesis. STXM-XANES is an efficient spectroscopic technique to differentiate different phases of C, including collagen, so as to determine whether collagen directly contacts with implant surfaces. Additionally, further work to understand the crystallinity and phase of bone mineral apatite throughout the transition layer from the mature bone to implant surface is also important information for osseointegration research, which could be explored by convergent beam electron diffraction. Suitable standards would need to be determined for the apatite phases, and it is expected that several phases may overlap due to the limited spatial resolution of the technique, requiring efforts to separate multiple patterns appearing from spatially overlapping phases.

The *in-situ* LP-TEM research on CaP mineralization presented in this thesis has laid a

foundation for exploring complex bone mineralization processes. Looking beyond CaP nucleation and growth, bone mineralization also includes various dynamic organic-inorganic physiological interactions which have significant effects on mineralization outcomes. Thus, LP-TEM will be a promising technique to achieve real-time recording of these dynamic processes and help to understand the mechanism of bone mineralization.

Appendix 1 High-Resolution Visualization of the Osteocyte Lacuno-Canalicular Network Juxtaposed to the Surface of Nanotextured Titanium Implants in Human

This paper presented the investigation of osteocyte lacuno-canalicular network adjoining the nanotextured surface of a clinical-retrieved titanium dental implant. Osteocytes, whose mechanotransduction function was reported to play a key role in bone remodeling, are also believed to influence on the maintenance of long-term osseointegration. With advanced electron microscopy and electron tomography, this work visualized the direct connection of osteocyte processes onto the implant surface and their ultrastructures, which could be used to infer the cellular events at the bone-implant interface. This work is a complementary approach to studying the mineral-organic structure of interface to my thesis. The electron tomography experiments and data analysis were performed by myself. Also, I helped with revising the manuscript. This paper has been published in ACS Biomaterials Science & Engineering, 2015, 1, pp 305-313. DOI: 10.1021/ab500127y.

ACS Biomaterials SCIENCE & ENGINEERING

Article

pubs.acs.org/journal/abseba

High-Resolution Visualization of the Osteocyte Lacuno-Canalicular Network Juxtaposed to the Surface of Nanotextured Titanium Implants in Human

Furqan A. Shah,[†,‡] Xiaoyue Wang,[§] Peter Thomsen,[†,‡] Kathryn Grandfield,[§] and Anders Palmquist*[,†,‡]

[†]Department of Biomaterials, Institute of Clinical Sciences, and [‡]BIOMATCELL VINN Excellence Center of Biomaterials and Cell Therapy, Sahlgrenska Academy at University of Gothenburg, SE-405 30 Gothenburg, Sweden

[§]Department of Materials Science and Engineering, McMaster University, Hamilton, ON L8S 4L7, Canada

Supporting Information

ABSTRACT: Osseointegration is controlled by a number of cellular mechanisms. Although factors governing bone formation are well-understood, the maintenance of bone at the bone-implant interface is less clear. Of some interest is the role of osteocytes, which via mechanotransduction are believed to be responsible for mechanical loading-based remodelling events in bone. Using a resin cast etching technique, we investigated the osteocyte lacuno-canalicular network adjacent to nanostructured titanium human dental implants after four years in clinical function. Correlative electron microscopy showed nanoscale osteocyte processes extending directly onto the implant surface. Calcium signal mapping via electron energy loss spectroscopy (EELS) showed apatite ingrowth into the nanotextured surface, while the apatite platelet *c*-axis was oriented approximately parallel to the collagen fibril direction. Furthermore, Z-contrast electron tomography demonstrated that natural bone-osteocyte and engineered bone-implant interfaces are similar in ultrastructural morphology. The present ultrastructural observation of multiple connections between osteocyte canaliculi and the nanotextured surface oxide suggests that osteocytes contribute toward the maintenance of osseointegration in long-term clinical function.

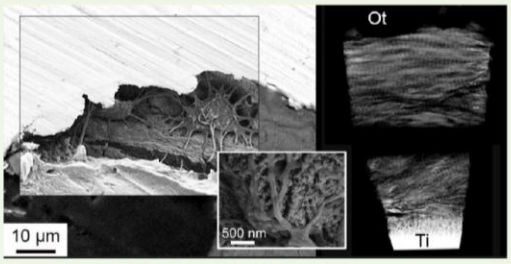

KEYWORDS: *dental implant, bone remodelling, osteocyte, interface, electron microscopy, osseointegration*

1. INTRODUCTION

Dental rehabilitation by osseointegrated implants has become widely popular in dentistry[1] with reliable long-term clinical results.[2] Other recent applications of osseointegration include bone-anchored hearing aids and major limb amputation prostheses, considerably improving the quality of life for patients.[3] Bone is a complex hierarchical structure[4] with its formation and maintenance governed by cellular events. Implant surfaces with nanostructures superimposed on a micron scale topography mimic this structural hierarchy of bone.[5] These nanostructures promote mesenchymal stem cell differentiation toward an osteogenic lineage,[6] and have been shown to be important for osseointegration.[7] During bone formation, osteoblasts produce tropocollagen,[8] which self-assembles into an extracellular matrix of collagen fibrils.[9] Subsequent mineralization causes the osteoblasts to become entrapped within the bone matrix and differentiate into osteocytes.[10] The alignment of the osteocyte lacuno-canalicular network reflects the pattern of extracellular matrix formation,[11] i.e., osteocyte lacunae are aligned parallel to the lamellar direction while the canaliculi extend perpendicularly, and could be used to interpret the formation and remodelling processes. The osteocyte network is believed to be responsible for sensing mechanical loading, and via mechanotransduction, orchestrates suitable bone remodelling to support the mechanical loading profiles by communicating with the osteoclasts and osteoblasts, the bone resorbing and bone building cells, to maintain an optimum bone mass.[12] Osteocyte processes (dendrites) reside within interconnecting channels known as canaliculi. Moreover, these dendritic connections between osteocytes are not permanent but rather the dendrites are frequently extended and retracted.[13] The osteocyte may sense mechanical loading in several ways, for example via the cell body, the dendritic extensions, or by bending of cell surface cilia.[14] The dendritic extensions remain of considerable significance, as indicated by the strain-amplification hypothesis based on the interaction between the pericellular matrix and the osteocyte process cytoskeleton.[15]

It is proposed that osteocytes in the vicinity of implant surfaces give insight into the healing process around metallic implants. In a canine model, early attempts to study the osteocyte processes in relation to the implant surface by high-voltage transmission electron microscopy (TEM) suggested an intimate contact to the implant surface.[16,17] However, the precise location and quality of the interface zone could not be ensured because of their use of a

Received: November 19, 2014
Accepted: March 27, 2015
Published: March 27, 2015

DOI: 10.1021/ab500127y
ACS Biomater. Sci. Eng. 2015, 1, 305−313

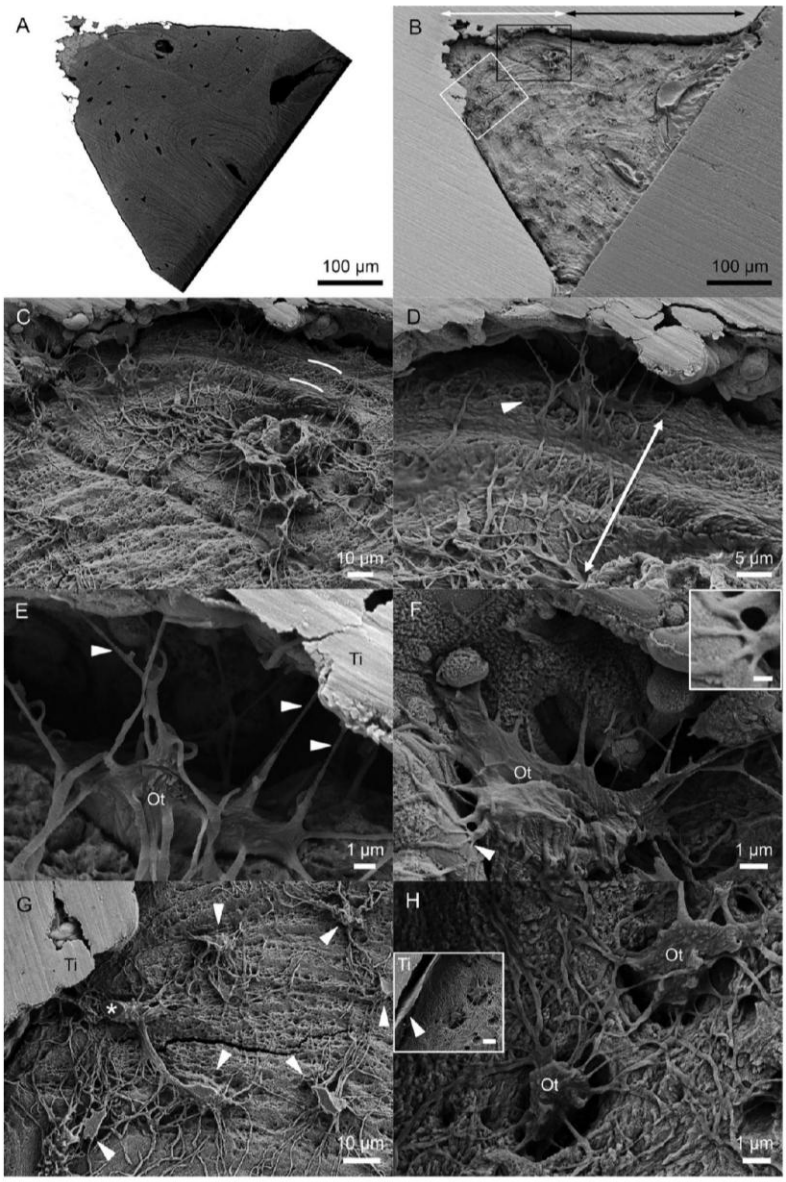

Figure 1. (A) Cortical-type osteonal bone fills the implant thread, with osteocyte lacunae aligned along the concentric lamellae (BSE-SEM). (B) After the resin cast etching procedure, numerous osteocytes are exposed along the lamellar directions. Arrows demarcate regions of the laser-modified nanosurface (white) and unaltered machined surface (black). (C) Osteocytes are seen in close association with the implant surface (black box in B) with several canaliculi running perpendicularly away from the implant surface, branching and rejoining, crossing several bone lamellae (white arcs) to reach a central Haversian canal. (D) In higher resolution, several canaliculi from an osteocyte (arrowhead) extend toward the implant surface as well as in the direction of a central Haversian canal approximately 30 μm (arrow) away from the implant surface. (E, F) On closer inspection, osteocytes are in close contact with the implant surface, with a large number of canaliculi (arrowheads) extending toward the surface oxide layer. Inset in F: Enlargement of an area of a branched canaliculus (arrowhead). Scale bar = 500 nm. (G) A network of interconnected osteocytes (arrowheads) exists in close proximity to the laser-ablated part of the implant surface (white box in B) and communicates with a blood vessel (*). (H) Two osteocytes may be observed extending a branching, interconnected network of canaliculi in an area adjacent to the machined part of the implant surface. Inset in H: Overview of the area shown. The tissue has separated from the implant surface (an artifact of tissue processing: fixation, dehydration, resin embedding) resulting in a narrow continuous gap, which may subsequently be infiltrated by the embedding resin (arrowhead). Scale bar = 5 μm.

cryofracture technique, where the metal is purposefully separated from the surrounding tissue. Experimental animal studies have demonstrated osteoblasts[18] and osteocyte processes approaching the surface of titanium coated plastic implants[19] at relatively short healing times in unloaded conditions. However, osteocytes have not previously been demonstrated at long-term healing, in functionally loaded conditions, particularly in humans.

Although the role of osteocytes is certainly relevant to the maintenance of osseointegration, the lack of appropriate studies to investigate this phenomenon gives rise to number of questions:

DOI: 10.1021/ab500127y
ACS Biomater. Sci. Eng. 2015, 1, 305−313

Is there an interconnecting network of osteocytes (and the lacuno-canalicular system) in the vicinity of osseointegrated implant surfaces? Do osteocytes make direct contact with implant surfaces via dendritic processes, for example to sense mechanical loading? What is the structure and morphology of the bone tissue between the implant surface and the nearest osteocyte lacunae? Is the engineered bone-implant interface analogous to the naturally existing bone-osteocyte interface? By utilizing advanced characterization approaches, and human bone-implant specimens, the present work was able to address these pertinent scientific questions regarding the role of osteocytes and bone growth surrounding nanostructured implants.

2. MATERIALS AND METHODS

Three clinically retrieved partly laser-modified commercially pure titanium dental implants (Biohelix, Brånemark Integration AB, Mölndal, Sweden) from a previous study were used.[20] In brief, after 47 months in service, the implants were removed due to mechanical failure, from the jaw of a 66-year-old female with a dental history of severe bruxism. The implants were processed for histology by fixation, dehydration and resin embedding.[21]

The characteristics of the implant surface have been reviewed in detail elsewhere.[22] In brief, Biohelix implants have a dual surface structure consisting of an as-machined surface combined with a laser-ablated region occupying the deepest 1/3rd of the thread (Figure S1 in the Supporting Information). The laser-ablated areas consist of combined micro and nano roughness, with a thickened surface titanium oxide of mainly rutile structure.

2.1. Resin Cast Etching Technique. The bone-implant materials were fixed in formalin, dehydrated in a graded series of ethanol, embedded in LR White resin (London Resin Company, UK), and bisected longitudinally.[21] One half-block was polished using 400−2400 grit silicon carbide paper to expose the external curvature of the implant. The samples were air-dried overnight prior to low-vacuum backscattered electron (BSE) SEM imaging in a Quanta 200 environmental SEM (FEI Company, The Netherlands) operated at 20 kV and 0.5 Torr water vapor pressure. The samples were immersed in 9% H_3PO_4 (for 30 s), rinsed in Milli-Q water (for 5 s), immersed in 5% NaOCl (for 5 min), rinsed again (for 30 s) and air-dried overnight. The samples were Au sputter-coated (~10 nm) for high vacuum secondary electron SEM imaging in an Ultra 55 FEG SEM (Leo Electron Microscopy Ltd., UK) operated at 5 kV. The lateral dimensions of the osteocyte canaliculi, the average number of canaliculi per osteocyte lacuna (N.Ot.Ca/Ot.Lc), and the average length of canaliculi extending from the nearest osteocyte toward the implant surface were quantified in ImageJ (imagej.nih.gov/ij).

2.2. TEM Sample Preparation, Imaging, and Spectroscopy. The remaining half-block was polished and Au/Pd sputter-coated (~10 nm). A TEM sample (200−300 nm thick) was prepared across the bone-implant interface and the bone-osteocyte interface using a focused ion beam (FIB) in situ lift-out technique[23] in a Versa 3D Dualbeam FIB/SEM (FEI Company, The Netherlands).

High-angle annular dark-field STEM (HAADF-STEM) was used for *Z*- (atomic number) contrast imaging and chemical analysis of the bone-implant interface and the bone-osteocyte interface in Tecnai F20 and Titan^3 80−300 (FEI Company, The Netherlands). Selected area electron diffraction (SAED) was performed to investigate the crystalline orientation of apatite in TEM mode.

Electron energy loss spectroscopy (EELS) was performed on a monochromated double aberration-corrected Titan^3 80−300 (FEI Company, The Netherlands) equipped with a GIF Quantum (Gatan Inc., Pleasanton, CA, USA) postcolumn energy filter and operated at 300 kV. EELS spectrum images were collected with a 10^{-4} s exposure time, and 2.5−8.7 nm step size; and were processed using Digital Micrograph (Gatan Inc., Pleasanton, CA, USA).

2.3. Electron Tomography (ET). ET was performed on a Titan^3 80−300 operated at 300 kV. HAADF-STEM images were recorded every 2° in a single-axis tilt scheme spanning ±70° using FEI Explore 3D software. Reconstructions were carried out in FEI Inspect 3D using a simultaneous iterative reconstruction (SIRT) technique, with 25 iterations. Visualizations were created in Amira (FEI Visualization Sciences Group).

3. RESULTS AND DISCUSSION

The general histological picture of the bone-implant junction discerned from BSE imaging is of organized cortical-type osteonal lamellar bone filling the threads and around the implant (Figure 1A). Osteocytes were generally aligned along concentric lamellae. The three-dimensional osteocyte network was exposed by employing a resin cast etching technique,[24] which preferentially removes mineralized tissue leaving resin-infiltrated osteocyte lacuno-canalicular network and the vascular network intact (Figure 1B). The osteocyte lacuno-canalicular network was configured in concentric layers, connecting the central Haversian canal to the implant surface by multiple branching and rejoining canaliculi, often traversing 30−50 μm while crossing multiple interlamellar seams (Figure 1C). The interlamellar seams were affected relatively more and etched deeper than the lamellae themselves thus indicating compositional differences between the two structures (Figure 1C). The distance between the implant surface and the nearest osteocytes often spanned 3−5 μm (Figure 1E, 1F), numerous canaliculi nevertheless extended toward the laser-modified (Figure 1G), and the machined (Figure 1H) regions along the implant surface giving rise to interconnected canalicular networks.

In high-resolution, an intimate contact was observed between the canaliculi and the nanotextured surface (Figure 2). The

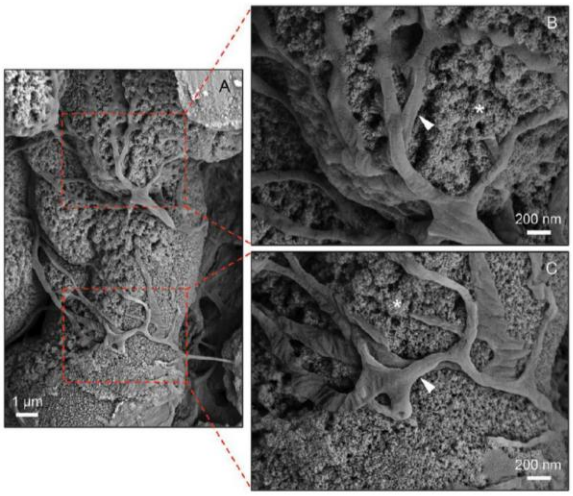

Figure 2. Branching canaliculi (arrowheads) are closely attached to the implant surface (asterisk).

nanotopography of the implant surface remained intact following the resin cast etching procedure, and appeared comparable to the native implant surface (Figure S1). Further, the lateral dimensions of the canaliculi, 362 ± 167 nm (n = 100), were within the range described by other methods.[25,26]

It is not possible to directly visualize the osteocytes or their dendritic extensions by the resin cast etching technique. In fact, the embedding resin infiltrates into the pericellular space while the cellular components remain encapsulated inside. Indeed, certain conditions, for instance hypoxia and skeletal microdamage may induce osteocyte apoptosis and/or the disruption of

DOI: 10.1021/ab500127y
ACS Biomater. Sci. Eng. 2015, 1, 305−313

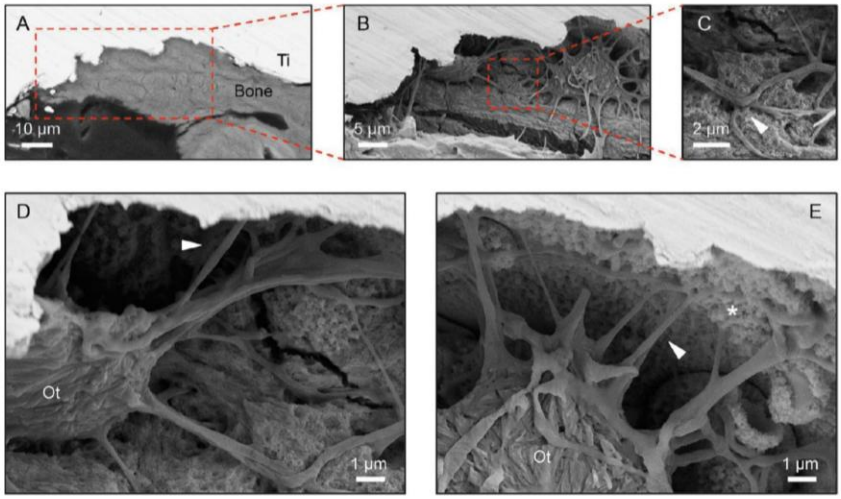

Figure 3. (A) Area of new bone formation, with both mineralized and unmineralized areas close to the implant surface (BSE-SEM). (B) After the acid-etching procedure, two osteocytes (box in A) were exposed immediately below the surface. (C) Interconnectivity of canaliculi from the two osteocytes (box in B) suggests cell-to-cell communication. (D, E) In high-resolution, numerous canaliculi from the osteocytes, seen in B, extend toward the implant surface, making intimate contact with the nanotextured oxide layer.

osteocyte processes. In such cases, although the cells and their dendritic extensions may be affected, the resin casts of the network remain intact.[24] Although with the use of this technique, no evidence can be provided regarding whether the osteocyte processes were actually within the canaliculi, it may be assumed that the visualized osteocytes would include viable osteocytes as well as a certain unknown proportion of osteocytes in various stages of aging and apoptosis. Osteocyte death is believed to represent a major contributor to lacunar hypermineralisation and their subsequent occlusion.[27] Even in situations where the osteocyte lacuna and the canaliculi become mineralized in vivo—a condition known as micropetrosis,[28] "fossilized" osteocytes with an apoptotic-like morphology have been identified within the mineralized mass.[29]

Across the periphery of an osteon and into the interstitial bone, the continuity of the canalicular network provides a framework for information exchange between the osteonal and the interstitial osteocytes.[30] Analogous to this observation in bone, the present ultrastructural observations suggest that the direct connectivity between osteocyte canaliculi and the implant surface may partly represent the architecture that is required for information exchange between osteocytes in the interfacial bone and the implant surface. While it cannot be said for certain whether the osteocyte processes within the canaliculi are indeed attached to the titanium oxide, it is plausible that the close attachment of osteocyte processes to the implant surface serves a particular function, whether it is one of anchorage,[31,32] or to sense mechanical stimuli as strain[15,33] or vibrations.[34] Indeed, lack of mechanical stimulation has been shown to be related to increased osteocyte apoptosis and the loss of cell viability.[35] Using a similar resin cast etching technique, Milovanovic and co-workers have demonstrated a reduction in the average number of canaliculi per osteocyte lacuna with advancing tissue age, implying reduced connectivity between osteocytes and the surrounding tissue.[30] Osteocyte apoptosis is generally believed to be associated with osteoclast activation and remodelling of bone.[36] And indeed, regions of localized remodelling were observed at the bone-implant interface (Figure S2).

The average number of canaliculi per osteocyte lacuna (N.Ot.Ca/Ot.Lc) decreases with advancing osteonal tissue age, implying reduced connectivity between osteocytes and the surrounding bone tissue, and therefore a diminished capacity to sense mechanical stimuli.[30] The N.Ot.Ca/Ot.Lc close to the implant surface (25 ± 6; $n = 9$) was higher ($p < 0.005$; two-tailed, two-sample unequal variance Student's t-test) than in bone located external to the implant thread (17 ± 3; $n = 9$), indicating "less aged" tissue adjacent to the implant surface. Canaliculi from the osteocytes nearest to the implant surface extended 4.4 ± 1.8 μm toward the surface. In an area of new bone formation (Figure 3A), osteocytes just below the bone surface were exposed after the resin cast etching procedure (Figure 3B). Canaliculi also extended toward the bone formation front, where an interconnectivity of canaliculi from individual osteocytes could be seen (Figure 3C), suggesting direct cell-to-cell communication. At this close length scale, bone formation is directed outward from the surface, where presumably the differentiating osteogenic cells make contact with the implant surface (Figure 3D, E), and begin to produce de novo bone by contact osteogenesis,[37] to later become entrapped within the surrounding bone as they terminally differentiate into osteocytes. However, the eventual fate of these osteocytes could not be known. Therefore, complementary to electron microscopy, the presence (or absence) of osteocytes at the bone-implant interface was confirmed by histological examination (Figure S2). And indeed, the presence of osteocyte-containing lacunae with osteocyte processes extending toward the implant surface after long-term healing in humans has been reported previously.[20]

More recently, using a similar acid-etching procedure, preferential etching at the bone-implant interface has been attributed to mineral deficiency.[38] Young osteocytes are believed to be able to both add and remove mineral from the lacunae and canaliculi.[14] And while it may be that the interfacial tissue is mineral-deficient because of localized osteocyte-mediated remodelling of the perilacunar tissue by means of load transfer from the implant into surrounding tissue and nearest osteocytes, it is equally likely that there is more inorganic component that

DOI: 10.1021/ab500127y
ACS Biomater. Sci. Eng. 2015, 1, 305−313

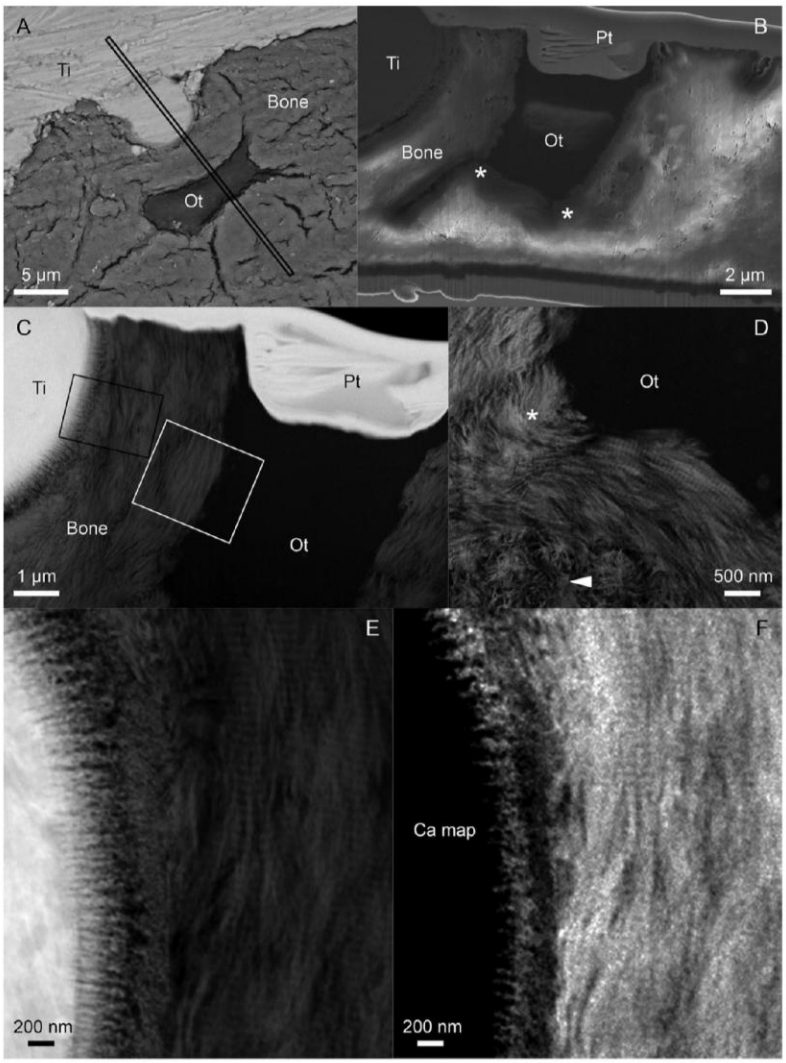

Figure 4. (A) Osteocyte lacuna in close proximity to the implant surface. The TEM sample site is outlined in black (SE-SEM). B) TEM specimen during the FIB-SEM milling process. Protective platinum (Pt) layer deposited prior to ion milling. The implant surface (Ti) and adjacent bone containing an osteocyte (Ot) can be seen, with two extending osteocyte processes (*). (C) HAADF-STEM image of the electron transparent TEM sample showing highly aligned bone tissue between Ti and the Ot. The outlined areas were used for subsequent electron tomography. (D) Bundles of collagen fibrils are seen parallel to the osteocyte surface, while at a distance (arrowhead) some are also observed to run into the plane of the image. The site of a canaliculus (*) is organized poorly. (E) On higher magnification, highly regular collagen banding can also be seen adjacent to the implant surface. (F) EELS calcium map of the area seen in E, indicating calcium ingrowth into the nanotextured surface oxide, while the collagen fibrils laid down adjacent to the implant surface are also well-mineralized.

could have been removed to a greater extent during the initial acid-etching step.[39] An alternate explanation for the deeper etching at the bone-implant interface may be the appearance of separation artifacts during tissue preparation.[40] These are observed frequently at implant surfaces which afford less micromechanical interlocking,[41] and deeper penetration of the etching agent along areas of the thread lacking nanomodification (Figure 1B) is likely. During chemical fixation and dehydration by organic solvents, bone shrinks slightly and may pull away from the relatively smooth machined part of the implant surface resulting in a minor gap which may subsequently be infiltrated by the embedding resin, to appear as a thin sheetlike layer (Figure 1H) of mostly high carbon content.[42] This resin-filled artifact has been previously referred to as an "undecalcified substance".[38] Moreover, it is possible to visualize the machining grooves having been imprinted on to the resin surface.

To further unravel the ultrastructural relationship between osteocytes and the implant surface, we prepared a TEM sample by a FIB in situ lift-out technique (Figure 4A, B, and Figure S3). In HAADF-STEM, the bone tissue between the implant surface and the osteocyte lacuna appears highly ordered with collagen fibrils running coparallel to both surfaces, i.e., the implant surface and the osteocyte surface (Figure 4C). The bone-osteocyte interface appeared to be similar all around the periphery with collagen fibrils running parallel to the entire surface, except in areas of canalicular extensions, where a more indistinct

DOI: 10.1021/ab500127y
ACS Biomater. Sci. Eng. 2015, 1, 305−313

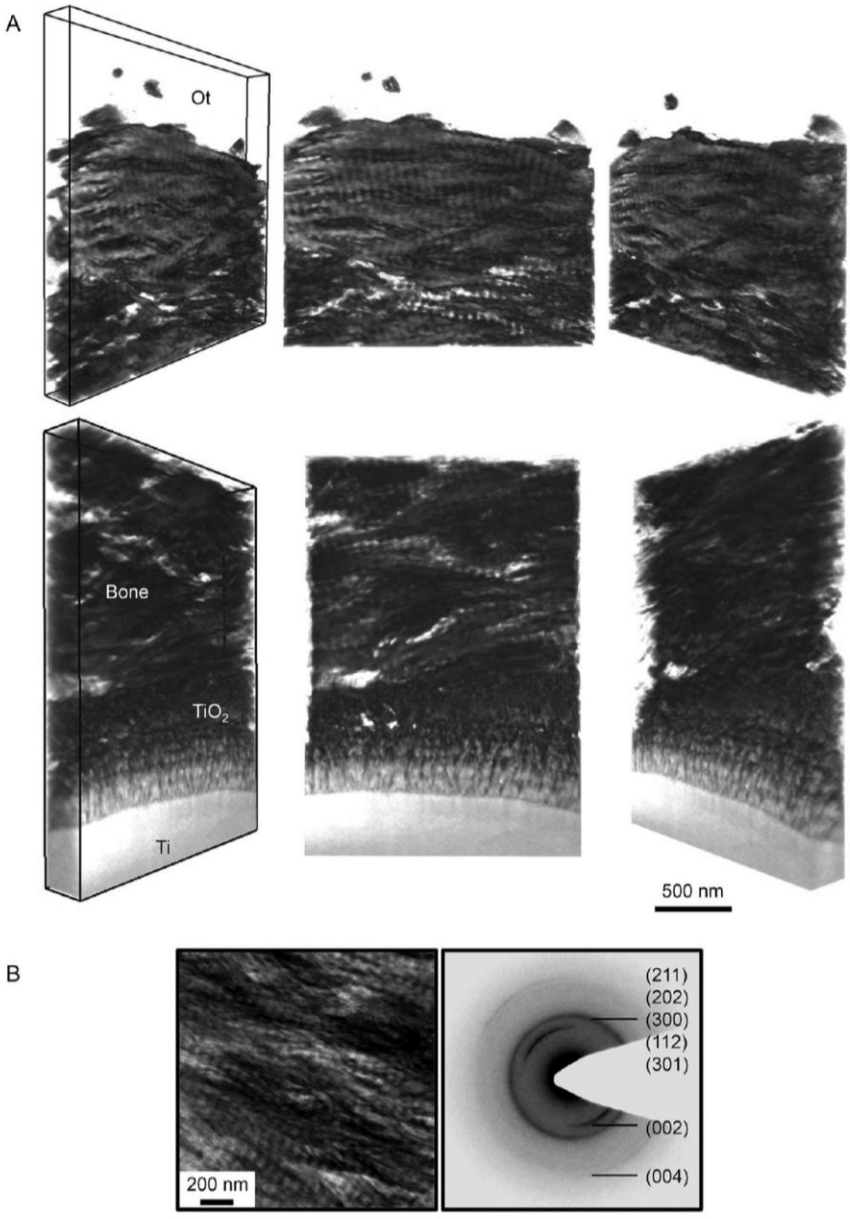

Figure 5. (A) Three-dimensional electron tomography reconstructions of the bone-osteocyte interface (upper row) and the bone-implant interface (lower row). At this hierarchical level, the organization of bone structure and collagen fibril alignment is demonstrated to be similar for both interfaces. (B) SAED shows apatite platelets typically oriented with their *c*-axis approximately parallel to the collagen fibril direction.

organization was observed presumably from collagen fibrils wrapping around the curvature of the canaliculus (Figure 4D). Indeed, bone ultrastructure has previously been described to be less well ordered directly around the canaliculi,[25] whereas better organization is seen within a short distance. Higher magnification (Figure 4E) showed an intimate contact at the bone-implant interface. Collagen fibrils were laid down parallel to the surface, almost making direct contact with surface oxide nanostructures that serve as a template for apatite formation.

Apatite ingrowth (approximately 200 nm) into the nanostructured surface oxide was confirmed by calcium signal mapping with EELS (Figure 4F), thus establishing the basis for a functionally graded interface between the nanostructured surface and mineralized bone tissue. In the case of de novo bone formation at biomaterial interfaces, a 500 nm thick, relatively hypermineralised, collagen-free, cement line interface is often described.[43] The precise composition of the cement lines associated with secondary osteons, whether poorly mineralized[44] or collagen deficient,[45] has been subject to much debate. Here, in contrast to the majority of previous studies, EELS demonstrates a zone of relatively higher intensity of calcium signal adjacent to the implant surface (Figure 4F), whereas a collagen-free zone could not be identified. In fact, well-aligned collagen fibrils were located immediately abutting the surface oxide. The ~200 nm

DOI: 10.1021/ab500127y
ACS Biomater. Sci. Eng. 2015, 1, 305−313

thick calcium deposition into the surface oxide (as seen by EELS calcium mapping) may be equivalent to the hypermineralized, collagen-free, cement line interface often described.[43] However, it must be recognized that the exclusion of collagen from these nanoscale oxide "channels" is a consequence of spatial constraints, i.e., the oxide surface features being too small to contain collagen fibrils. The present observation of well-aligned collagen fibrils directly abutting an implant surface after long-term clinical function confirms the observations made previously in human, after submerged short-term healing[41] and in experimental animal studies.[46]

It is important to state that the interpretation of the fine structure of the material-tissue interface is dependent on a large number of factors. In short, the species, the healing period, the material surface properties, the sample preparation methods, and the analytical techniques are all plausible factors in observing different results when resolving the interfacial ultrastructure. In the present work, the ultrastructure of the intact human bone-implant interface was demonstrated using sample preparation techniques that allowed a detailed investigation using a combination of correlative analytical techniques. Nevertheless, it may not be assumed that the ultrastructure of the bone-implant interface in specimens that have undergone functional loading for extended healing periods should be similar in humans (as investigated here) to what is observed either in vitro or in vivo after relatively brief healing periods in various animal models.

Electron tomography (ET) and 3D reconstructions allow a comprehensive analysis of bone ultrastructure at interfaces.[46,47] In this study, two volumes were reconstructed: (i) the bone-implant interface, and (ii) the bone-osteocyte interface (Figure 5A, B). Collagen fibrils ran along the plane of the sample in both cases and were parallel to the implant surface as well as the osteocyte. Although collagen fibrils make an immediate boundary to the lacunar space at the bone-osteocyte interface, the bone-implant interface appears to be structurally graded with apatite interdigitation into the oxide layer followed by well-aligned collagen fibrils interfacing the surface, further confirming the EELS findings. Nevertheless, the general morphology at both interfaces is that of collagen fibrils having a unidirectional alignment, exhibiting a ropelike twisting motif within a collagen fiber bundle, as seen in lamellar bone.[48] Interestingly, electron tomography suggests that the interfacial bone tissue exhibits a similar ultrastructural organization whether adjacent to functionally loaded implants or unloaded implants.[41]

Selected area electron diffraction (SAED) shows the *c*-axis of apatite platelets to be aligned approximately parallel to the long axis of collagen fibrils (Figure 5B), as seen from the arcs formed by the (002) and (004) reflections centered on the major fibril direction, subtending angles of ~35°.

From a biomechanical standpoint, the implants studied in this work had been in functional use for several years while supporting excessively high loads associated with bruxism (excessive parafunctional grinding of the teeth or clenching of the jaw),[20] and therefore suffered material failure rather than implant loosening. This attests to the potential role that osteocytes play in maintaining an intact interface between an implant and mineralized bone, which remains adaptive to applied loads long after initial osseointegration has occurred.

4. CONCLUSIONS

Ultrastructural similarities exist between the bone interfacing an implant surface (the bone-implant interface) and the bony wall of the osteocyte lacuna (the bone-osteocyte interface), both exhibiting comparable structural motifs such as the longitudinal orientation and ropelike twisting of mineralized collagen fibrils located directly at the surface. This work demonstrates that in humans, osteocytes, through canaliculi (which are believed to contain osteocyte processes), can make and retain intimate contact with implant surfaces, and appear to follow the surface contour, even after extended healing durations in functionally loaded conditions.

■ ASSOCIATED CONTENT

Supporting Information

The following file is available free of charge on the ACS Publications website at DOI: 10.1021/ab500127y.

Images showing (i) the hierarchically structured implant surface (Figure S1), (ii) histological evaluation of bone formed within the implant threads (Figure S2), and (iii) the focused ion beam (FIB) in situ lift-out technique for TEM sample preparation (Figure S3) (PDF)

ACS_BS&E_SupportingInformation.PDF.

■ AUTHOR INFORMATION

Corresponding Author

* E-mail: anders.palmquist@biomaterials.gu.se. Tel: +46 31 786 29 71.

Notes

The authors declare no competing financial interest.

■ ACKNOWLEDGMENTS

This study was supported by the Swedish Research Council (grant K2015-52X-09495-28-4), the BIOMATCELL VINN Excellence Center of Biomaterials and Cell Therapy, the Region Västra Götaland, an ALF/LUA grant, the IngaBritt and Arne Lundberg Foundation, the Dr. Felix Neubergh Foundation, Promobilia and the Hjalmar Svensson Foundation. F.A.S. holds a PhD position financed by the Swedish Government Strategic Funding of Materials Science Area of Advance, provided to Chalmers and Department of Biomaterials, University of Gothenburg. K.G. acknowledges support from the NSERC Discovery Grant Program, and X.W. the Ontario Trillium Scholarship. ET was performed at the Canadian Centre for Electron Microscopy at McMaster University, a facility supported by NSERC and other governmental agencies. The grant providers were not involved in the study design, data acquisition, interpretation, writing, and submission of the article.

■ REFERENCES

(1) Haïat, G.; Wang, H.-L.; Brunski, J. Effects of Biomechanical Properties of the Bone−Implant Interface on Dental Implant Stability: From In Silico Approaches to the Patient's Mouth. *Annu. Rev. Biomed. Eng.* **2014**, *16*, 187−213.

(2) Astrand, P.; Ahlqvist, J.; Gunne, J.; Nilson, H. Implant treatment of patients with edentulous jaws: a 20-year follow-up. *Clin. Implant Dent. Relat. Res.* **2008**, *10*, 207−17.

(3) Brånemark, R.; Berlin, Ö.; Hagberg, K.; Bergh, P.; Gunterberg, B.; Rydevik, B. A novel osseointegrated percutaneous prosthetic system for the treatment of patients with transfemoral amputation: A prospective study of 51 patients. *Bone Joint J.* **2014**, *96b*, 106−13.

(4) Weiner, S.; Wagner, H. D. The Material Bone: Structure-Mechanical Function Relations. *Annu. Rev. Mater. Sci.* **1998**, *28*, 271−298.

(5) Davies, J. E.; Ajami, E.; Moineddin, R.; Mendes, V. C. The roles of different scale ranges of surface implant topography on the stability of the bone/implant interface. *Biomaterials* **2013**, *34*, 3535−46.

DOI: 10.1021/ab500127y
ACS Biomater. Sci. Eng. 2015, 1, 305−313

(6) Dalby, M. J.; Gadegaard, N.; Tare, R.; Andar, A.; Riehle, M. O.; Herzyk, P.; Wilkinson, C. D.; Oreffo, R. O. The control of human mesenchymal cell differentiation using nanoscale symmetry and disorder. *Nat. Mater.* **2007**, *6*, 997−1003.
(7) Ballo, A.; Agheli, H.; Lausmaa, J.; Thomsen, P.; Petronis, S. Nanostructured model implants for in vivo studies: influence of well-defined nanotopography on de novo bone formation on titanium implants. *Int. J. Nanomed.* **2011**, *6*, 3415−28.
(8) Neve, A.; Corrado, A.; Cantatore, F. P. Osteoblast physiology in normal and pathological conditions. *Cell Tissue Res.* **2011**, *343*, 289−302.
(9) Silver, F. H.; Freeman, J. W.; Seehra, G. P. Collagen self-assembly and the development of tendon mechanical properties. *J. Biomech.* **2003**, *36*, 1529−53.
(10) Franz-Odendaal, T. A.; Hall, B. K.; Witten, P. E. Buried alive: how osteoblasts become osteocytes. *Dev. Dyn.* **2006**, *235*, 176−90.
(11) Kerschnitzki, M.; Wagermaier, W.; Roschger, P.; Seto, J.; Shahar, R.; Duda, G. N.; Mundlos, S.; Fratzl, P. The organization of the osteocyte network mirrors the extracellular matrix orientation in bone. *J. Struct. Biol.* **2011**, *173*, 303−11.
(12) Klein-Nulend, J.; Bakker, A. D.; Bacabac, R. G.; Vatsa, A.; Weinbaum, S. Mechanosensation and transduction in osteocytes. *Bone* **2013**, *54*, 182−90.
(13) Webster, D. J.; Schneider, P.; Dallas, S. L.; Müller, R. Studying osteocytes within their environment. *Bone* **2013**, *54*, 285−295.
(14) Bonewald, L. F. The amazing osteocyte. *J. Bone Miner. Res.* **2011**, *26*, 229−238.
(15) Han, Y.; Cowin, S. C.; Schaffler, M. B.; Weinbaum, S. Mechanotransduction and strain amplification in osteocyte cell processes. *Proc. Natl. Acad. Sci. U. S. A.* **2004**, *101*, 16689−16694.
(16) Steflik, D. E.; Hanes, P. J.; Sisk, A. L.; Parr, G. R.; Song, M. J.; Lake, F. T.; McKinney, R. V. Transmission electron microscopic and high voltage electron microscopic observations of the bone and osteocyte activity adjacent to unloaded dental implants placed in dogs. *J. Periodontol.* **1992**, *63*, 443−52.
(17) Steflik, D. E.; Sisk, A. L.; Parr, G. R.; Lake, F. T.; Hanes, P. J.; Berkery, D. J.; Brewer, P. Transmission electron and high-voltage electron microscopy of osteocyte cellular processes extending to the dental implant surface. *J. Biomed. Mater. Res.* **1994**, *28*, 1095−107.
(18) Morinaga, K.; Kido, H.; Sato, A.; Watazu, A.; Matsuura, M. Chronological Changes in the Ultrastructure of Titanium-Bone Interfaces: Analysis by Light Microscopy, Transmission Electron Microscopy, and Micro-Computed Tomography. *Clinical Implant Dentistry and Related Research* **2009**, *11*, 59−68.
(19) Okamatsu, K.; Kido, H.; Sato, A.; Watazu, A.; Matsuura, M. Ultrastructure of the Interface Between Titanium and Surrounding Tissue in Rat Tibiae − A Comparison Study on Titanium-Coated and -Uncoated Plastic Implants. *Clin. Implant Dent. Relat. Res.* **2007**, *9*, 100−111.
(20) Shah, F. A.; Nilson, B.; Brånemark, R.; Thomsen, P.; Palmquist, A. The bone-implant interface − nanoscale analysis of clinically retrieved dental implants. *Nanomedicine* **2014**, *10*, 1729−37.
(21) Donath, K.; Breuner, G. A method for the study of undecalcified bones and teeth with attached soft tissues. The Sage-Schliff (sawing and grinding) technique. *J. Oral Pathol. Med.* **1982**, *11*, 318−26.
(22) Palmquist, A.; Engqvist, H.; Lausmaa, J.; Thomsen, P. Commercially Available Dental Implants: Review of Their Surface Characteristics. *J. Biomater. Tissue Eng.* **2012**, *2*, 112−124.
(23) Jarmar, T.; Palmquist, A.; Brånemark, R.; Hermansson, L.; Engqvist, H.; Thomsen, P. Technique for preparation and characterization in cross-section of oral titanium implant surfaces using focused ion beam and transmission electron microscopy. *J. Biomed. Mater. Res., Part A* **2008**, *87A*, 1003−1009.
(24) Kubek, D. J.; Gattone, V. H.; Allen, M. R. Methodological assessment of acid-etching for visualizing the osteocyte lacunar-canalicular networks using scanning electron microscopy. *Microsc. Res. Tech.* **2010**, *73*, 182−6.
(25) Reznikov, N.; Shahar, R.; Weiner, S. Three-dimensional structure of human lamellar bone: the presence of two different materials and new insights into the hierarchical organization. *Bone* **2014**, *59*, 93−104.
(26) Shah, F. A.; Johansson, B. R.; Thomsen, P.; Palmquist, A. Ultrastructural evaluation of shrinkage artefacts induced by fixatives and embedding resins on osteocyte processes and pericellular space dimensions. *J. Biomed Mater. Res. A* **2014**, *103*, 1565−1564.
(27) Busse, B.; Djonic, D.; Milovanovic, P.; Hahn, M.; Puschel, K.; Ritchie, R. O.; Djuric, M.; Amling, M. Decrease in the osteocyte lacunar density accompanied by hypermineralized lacunar occlusion reveals failure and delay of remodeling in aged human bone. *Aging Cell* **2010**, *9*, 1065−75.
(28) Frost, H. M. Micropetrosis. *J. Bone Joint Surg.* **1960**, *42a*, 144−50.
(29) Bell, L. S.; Kayser, M.; Jones, C. The mineralized osteocyte: A living fossil. *Am. J. Phys. Anthropol.* **2008**, *137*, 449−456.
(30) Milovanovic, P.; Zimmermann, E. A.; Hahn, M.; Djonic, D.; Püschel, K.; Djuric, M.; Amling, M.; Busse, B. Osteocytic Canalicular Networks: Morphological Implications for Altered Mechanosensitivity. *ACS Nano* **2013**, *7*, 7542−7551.
(31) You, L. D.; Weinbaum, S.; Cowin, S. C.; Schaffler, M. B. Ultrastructure of the osteocyte process and its pericellular matrix. *Anat. Rec.* **2004**, *278*, 505−13.
(32) McNamara, L. M.; Majeska, R. J.; Weinbaum, S.; Friedrich, V.; Schaffler, M. B. Attachment of osteocyte cell processes to the bone matrix. *Anat. Rec.* **2009**, *292*, 355−63.
(33) You, L.; Cowin, S. C.; Schaffler, M. B.; Weinbaum, S. A model for strain amplification in the actin cytoskeleton of osteocytes due to fluid drag on pericellular matrix. *J. Biomech.* **2001**, *34*, 1375−1386.
(34) Lau, E.; Al-Dujaili, S.; Guenther, A.; Liu, D.; Wang, L.; You, L. Effect of low-magnitude, high-frequency vibration on osteocytes in the regulation of osteoclasts. *Bone* **2010**, *46*, 1508−1515.
(35) Mann, V.; Huber, C.; Kogianni, G.; Jones, D.; Noble, B. The influence of mechanical stimulation on osteocyte apoptosis and bone viability in human trabecular bone. *J. Musculoskel. Neuron. Interact.* **2006**, *6*, 408−417.
(36) Cardoso, L.; Herman, B. C.; Verborgt, O.; Laudier, D.; Majeska, R. J.; Schaffler, M. B. Osteocyte Apoptosis Controls Activation of Intracortical Resorption in Response to Bone Fatigue. *J. Bone Miner. Res.* **2009**, *24*, 597−605.
(37) Davies, J. E. Understanding peri-implant endosseous healing. *J. Dent. Educ.* **2003**, *67*, 932−49.
(38) Du, Z.; Ivanovski, S.; Hamlet, S. M.; Feng, J. Q.; Xiao, Y. The Ultrastructural Relationship Between Osteocytes and Dental Implants Following Osseointegration. *Clin. Implant Dent. Relat. Res.* **2014**, DOI: 10.1111/cid.12257.
(39) Boyde, A., Scanning Electron Microscope Studies of Bone. In *The Biochemistry and Physiology of Bone*, 2nd ed.; Bourne, G. H., Ed.; Academic Press: New York, 1972; Vol. *I*.
(40) Palmquist, A.; Lindberg, F.; Emanuelsson, L.; Brånemark, R.; Engqvist, H.; Thomsen, P. Morphological studies on machined implants of commercially pure titanium and titanium alloy (Ti6Al4V) in the rabbit. *J. Biomed. Mater. Res., Part B* **2009**, *91B*, 309−319.
(41) Palmquist, A.; Grandfield, K.; Norlindh, B.; Mattsson, T.; Brånemark, R.; Thomsen, P. Bone-titanium oxide interface in humans revealed by transmission electron microscopy and electron tomography. *J. R. Soc., Interface* **2012**, *9*, 396−400.
(42) Palmquist, A.; Jarmar, T.; Emanuelsson, L.; Brånemark, R.; Engqvist, H.; Thomsen, P. Forearm bone-anchored amputation prosthesis: a case study on the osseointegration. *Acta Orthopaedica* **2008**, *79*, 78−85.
(43) Davies, J. E. Bone bonding at natural and biomaterial surfaces. *Biomaterials* **2007**, *28*, 5058−5067.
(44) Burr, D. B.; Schaffler, M. B.; Frederickson, R. G. Composition of the cement line and its possible mechanical role as a local interface in human compact bone. *J. Biomech* **1988**, *21*, 939−45.
(45) Skedros, J. G.; Holmes, J. L.; Vajda, E. G.; Bloebaum, R. D. Cement lines of secondary osteons in human bone are not mineral-deficient: New data in a historical perspective. *Anat. Rec., Part A* **2005**, *286A*, 781−803.

DOI: 10.1021/ab500127y
ACS Biomater. Sci. Eng. 2015, 1, 305−313

(46) Grandfield, K.; Gustafsson, S.; Palmquist, A. Where bone meets implant: the characterization of nano-osseointegration. *Nanoscale* **2013**, *5*, 4302−8.
(47) Grandfield, K.; McNally, E. A.; Palmquist, A.; Botton, G. A.; Thomsen, P.; Engqvist, H. Visualizing biointerfaces in three dimensions: electron tomography of the bone−hydroxyapatite interface. *J. R. Soc., Interface* **2010**, *7*, 1497−1501.
(48) Reznikov, N.; Shahar, R.; Weiner, S. Bone hierarchical structure in three dimensions. *Acta Biomater.* **2014**, *10*, 3815−3826.

DOI: 10.1021/ab500127y
ACS Biomater. Sci. Eng. 2015, 1, 305−313

Appendix 2 Atomic Scale Chemical Tomography of Human Bone

This paper presented the first atomic-length-scale visualization of human bone structure with elemental distribution overlaid in three dimensions (3D). In this work, the atom probe tomography (APT) experimental parameters for human bone samples were optimized and the mass spectra of human bone were provided as reference for future research, which laid down the foundation to apply APT to study the more complex sample bone-implant interface in the thesis. The APT experiments and data analysis were performed by Dr. Brian Langelier and myself. Dr. Kathryn Grandfield and I performed electron microscopy. The manuscript was drafted and edited to the final version by Dr. Kathryn Grandfield, Dr. Brian Langelier and myself. This paper has been published in Scientific Reports, 2017, 7:39958, pp 1-9. DOI: 10.1038/srep39958. Permission from

SCIENTIFIC REPORTS

OPEN

Atomic scale chemical tomography of human bone

Brian Langelier[1], Xiaoyue Wang[1] & Kathryn Grandfield[1,2]

Received: 30 September 2016
Accepted: 28 November 2016
Published: 05 January 2017

Human bone is a complex hierarchical material. Understanding bone structure and its corresponding composition at the nanometer scale is critical for elucidating mechanisms of biomineralization under healthy and pathological states. However, the three-dimensional structure and chemical nature of bone remains largely unexplored at the nanometer scale due to the challenges associated with characterizing both the structural and chemical integrity of bone simultaneously. Here, we use correlative transmission electron microscopy and atom probe tomography for the first time, to our knowledge, to reveal structures in human bone at the atomic level. This approach provides an overlaying chemical map of the organic and inorganic constituents of bone on its structure. This first use of atom probe tomography on human bone reveals local gradients, trace element detection of Mg, and the co-localization of Na with the inorganic-organic interface of bone mineral and collagen fibrils, suggesting the important role of Na-rich organics in the structural connection between mineral and collagen. Our findings provide the first insights into the hierarchical organization and chemical heterogeneity in human bone in three-dimensions at its smallest length scale – the atomic level. We demonstrate that atom probe tomography shows potential for new insights in biomineralization research on bone.

The human skeletal system has a profound importance for our daily lives: acting as the main mechanism for coordinating mobility, and as the largest ion exchanger in our bodies to maintain homeostasis. Understanding the structure of human bone at all hierarchical levels has major implications for mineralization mechanisms, mechanical support, and assessment and treatment of bone pathologies. It is generally accepted that bone consists of two main components: Type I collagen, and carbonated hydroxyapatite crystals, with other minor constituents: water, non-collagenous proteins, such as proteoglycans, cells and blood vessels[1,2]. These main components self-assemble into mineralized collagen fibers that are used as the building blocks for higher-level architectures. The organization of these components and their subsequent arrangement into hierarchical levels has large implications for the structure-function relationships of bone, including its mechanical properties[3,4]. Many studies have focused on the relationship between the mineral and organic components of bone, highlighting the energetic basis for their interaction[5], and mapping out their structure with various electron microscopies[6,7]. Yet the biomineralization mechanisms of human bone remain debated[8], partly due to the inability to characterize both bone structure and composition at its building block level. The appeal of studies with high spatial and chemical resolution, such as that presented herein, is the possibility to elucidate mechanisms of mineralization, and the structure-function relationships that govern behavior of bone from the sub-nanometer scale up.

The characterization of the nanoscale structural and chemical architecture of bone embodies a number of challenges, particularly in three-dimensions. Established techniques, such as nano-computed tomography (nano-CT), can probe the 3D structure of bone on the order of 100 nm yet the constituents of bone, collagen fibrils and carbonated hydroxyapatite crystals, are orders of magnitude smaller[9]. Similarly, techniques such as NMR have the capability to probe chemical structures of bone to the molecular level, even in hydrated states. Recent work with this technique has shown strong evidence for the presence of citrate bridges between bone-mineral and collagen, however the technique lacks the site-specificity to accurately describe the exact locale of species detected[10]. Other techniques to probe chemical composition of bone on the molecular level, such as Raman and Fourier-Transform Infrared spectroscopy are widespread. These can be linked to identifying markers of bone crystallinity, aging and disease state, as well as to specific changes in composition, such as degree of carbonate substitution in bone mineral[11]. Advances towards probing 3D chemical composition and collagen orientation simultaneously have been made by employing polarized Raman spectroscopy[12]. However, it is important to note these analyses resolve molecular information only spatially at the micron scale, probing features such as

[1]Department of Materials Science and Engineering, McMaster University, Hamilton, ON, L8S 4L7, Canada. [2]School of Biomedical Engineering, McMaster University, Hamilton, ON, L8S 4L7, Canada. Correspondence and requests for materials should be addressed to K.G. (email: kgrandfield@mcmaster.ca)

osteonal and lamellar bone. Recently, focused ion beam (FIB) serial sectioning has surfaced as another potential 3D imaging modality for bone structure, however present studies[2,6] report demineralized bone tissue and this modality is restricted to the resolution limits of scanning electron microscopy (SEM). Indeed the transmission electron microscope (TEM) provides a suitable approach to nanoscale imaging, with possibilities in both 2D and 3D with electron tomography. Yet the inherent energy and spatial resolution limits of analytical spectroscopic techniques, such as energy dispersive x-ray spectroscopy (EDX) and electron energy loss spectroscopy (EELS) on beam-sensitive bone, have prevented the possibility for combined TEM and chemical analysis in 3D at the nanometer level.

To circumvent these challenges, we demonstrate herein that correlative compositional contrast imaging in the TEM with atom probe tomography (APT) provides a both a structural and chemical nanotomography of human bone. This technique has enabled us to perform the first APT on human bone to identify chemical heterogeneities and localization of trace elements.

APT is based on the successive field evaporation of atoms as ions from the surface of a specimen within an electric field, which are then collected by a lateral (x, y) position-sensitive detector. Field evaporation is triggered in pulses, which allows for both the sequence of evaporation and ion time-of-flight to be recorded for each ion. From these parameters, the original z-coordinates of the ions and an atomic mass-to-charge (m/z) spectrum can be determined. The data produced by an APT experiment can therefore be reconstructed to provide a 3D model of the analyzed volume, detailing the spatial and chemical features of the sample with sub-0.3 nm spatial resolution to 1 ppm chemical sensitivity[13].

Traditionally, field evaporation in atom probe experiments was triggered by a pulsed electric field, which limited the type of specimens suitable for this technique to materials with good electrical conductivity and reasonable ductility (i.e. metals). However, the development of laser-pulsing techniques has widened the applicability of APT to nearly all manner of solid material[13,14]. The detailed investigation of apatites and biominerals with APT was first pioneered by the group of Joester *et al.* They have reported APT on hydroxyapatite, elephant dentin, rat femur cortical bone, and dental enamel, for example[15–18]. Since their successful demonstration of APT as a powerful characterization technique for bone-like materials and biominerals, the application of APT to other bone-related research, such as the investigation of implant-bone interfaces, has been noted[19,20].

Although APT has been demonstrated on several biominerals, human bone presents unique challenges for successful APT analysis, including its high organic content (~35 wt%) and therefore chemically and crystallographically heterogeneous structure, not to mention its complex ionic and covalent bonding and its low conductivity. The system used for the current analysis utilized a pulsed 355 nm UV laser to illuminate the bone specimen tip in a static DC electric field, and promote field evaporation of surface atoms. Unfortunately, as human bone is a relatively poor conductor of heat at room temperature (0.16–0.34 W/m°C[21]), it is relatively slow to cool down following heating by the laser pulses, even at the low cryogenic temperatures used in APT. This means that in many cases the timing of atomic evaporation may substantially lag behind the timing of the laser pulse. This effect degrades the mass resolving power of the technique and leads to so-called thermal tails trailing form the ion peak to higher mass-to-charge values in the spectra. An attempt was made to optimize the laser pulse energy to minimize thermal tails while keeping background counts low, which yielded values lower than in previous reports of similar organic materials[15,16]. However, the very heterogeneous and highly organic nature of bone has generally made it difficult to identify the most optimum operating parameters, as so clearly demonstrated for other less heterogeneous bone-like materials, like hydroxyapatite. To highlight the complexity of achieving APT data on human bone, in this work more than 10 samples of human bone were prepared and analyzed in the atom probe, of which only ~60% of samples yielded more than 1×10^6 ions, and only ~25% yielding more than 3×10^6 ions. This paper primarily reports data from 3 of these samples, representing approximately 13×10^6 total collected ions. Therefore, while a sufficient amount of data for analysis was obtained, the sample yield remained too low to allow for clear optimization of many APT operating parameters.

Results and Discussion

Human bone tissue from the maxilla was shaped into a sharpened nano-pillar for TEM and APT using an *in-situ* FIB technique (Fig. S1). Z-contrast images were recorded on a high-angle annular dark-field (HAADF) detector to provide compositional contrast for structural cues. Using the same sample, APT unveiled the chemical distributions at the near sub-nanometer level, which could then be correlated with the electron microscopic images. The combination of these techniques enables us to report bone architectures and chemical distributions with unparalleled spatial accuracy and confidence.

In this work, we push the analysis of human bone to the smallest length scale possible today-to the individual atoms that compose the tissue. Indeed, the complexity associated with APT experiments and data reconstruction with bone is compounded by its highly heterogeneous nature, as most standard APT theory and reconstruction algorithms are based on homogeneous materials. In this regard, the importance of correlative microscopies is highlighted. By comparing to STEM images of the specimen prior to APT analysis (e.g. a typical dataset shown in Fig. 1), we can measure the shank half angle accurately to assist with reconstruction, and do not have to depend on the relation between applied DC voltage and tip radius, which can be irregular for non-conductive materials. To improve the spatial accuracy of the reconstructions, the evaporation field would be estimated such that the Ca-rich features in the reconstruction were consistent with the bright contrast regions in the STEM images. The data acquisition and reconstruction procedures are further elaborated on within the Materials and Methods section of the manuscript. In addition, comparison with features in the STEM image enabled us to ascertain accurate reconstruction parameters to correctly distribute elements in 3D space. For example, the HAADF STEM image (Fig. 1a) can be easily interpreted based on its compositional contrast – the platelet-like bright rods are the calcium and phosphate-rich bone mineral crystals, seen in this image oriented slightly at an angle to the long axis of the APT needle. Less dense, organic-rich regions are darker in contrast. Knowledge of these features noted in the

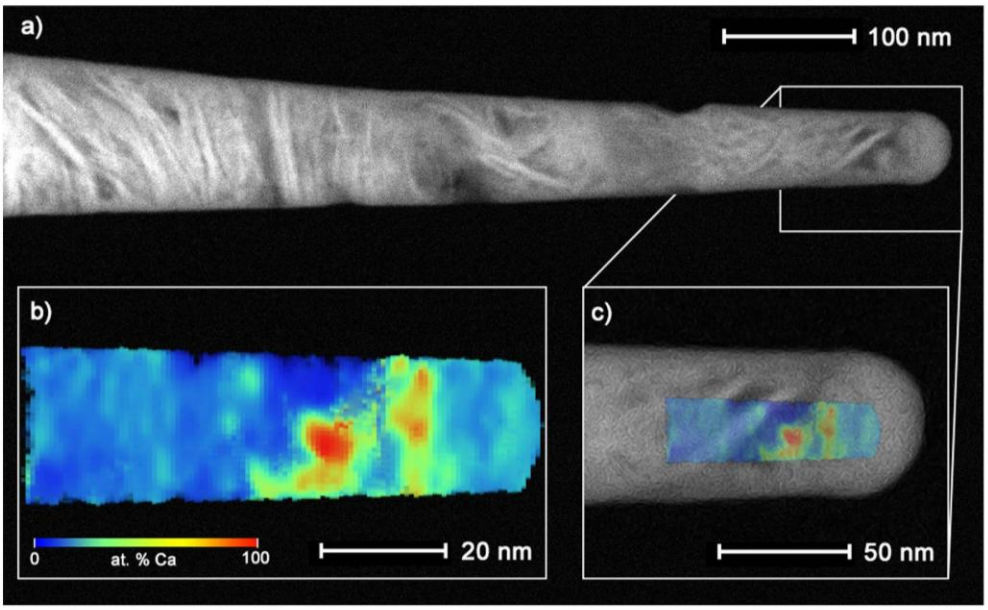

Figure 1. Correlative electron microscopy and APT reveal structural and chemical distributions in bone. Reconstruction parameters were optimized for detector and evaporation efficiency by utilizing the structural information from STEM HAADF imaging of the bone tip before APT (**a**), to produce the Ca concentration gradient map from APT analysis (**b**), shown overlapped in (**c**). Regions rich in Ca (red) correspond well to the plate like crystals imaged in STEM (bright needle-like features).

STEM image were key for optimizing the reconstruction parameters for the APT dataset overlaid in Fig. 1b and c. The reconstruction parameters generated from correlative data could also be applied to datasets when correlative data was not available.

APT spectra from several bone specimens were collected; a representative spectrum highlighting the chemical complexity is shown in Fig. 2, for the full bone specimen (Fig. 2a) and sub-volumes related to mineral and matrix regions (Fig. 2b and c, respectively). Reconstruction of these spectra into gradient maps (e.g. Figs 1 and 3) provides a convenient way to visualize the compositional and spatial mineral-matrix relationships, which are less easy to visualize in 3D atom maps or isoconcentration surfaces due the dense heterogeneity of bone. Table 1 reports the overall composition of human bone as measured by APT and averaged over all datasets. Values are in close agreement with anticipated concentrations based on the assumption that the mineral phase in bone is hydroxyapatite. The Ca:P atomic ratio is measured to be 2.26 ± 0.51, near to the stoichiometric ratio of 1.67 in hydroxyapatite. Our datasets generally exhibit smaller thermal tails and lower background than many other bone-like minerals investigated, and thus show significantly more peaks above background. The unambiguous identification of many of these smaller peaks is very challenging, as there is typically an abundance of possible complex ions, and few supporting peaks of other isotopes that can be used confirm ranging. Additionally, it is still expected that many other peaks are present below the background or in the major thermal tails, and cannot be accounted for. This challenge with ranging ions is exemplified for P-related ions, where the low contribution to the Ca:P ratio is likely due to unranged P-containing compounds, either unidentified or lost to the background. Furthermore, some composition variation may be due to ambiguity in ranging for molecular ions whose peaks overlap due to equivalent mass:charge ratios, such as $P_2O_4^{2+}$ which overlaps with PO_2^{+}. Unfortunately, standards for ranging these ions do not presently exist.

Mineral-matrix organization. Our findings emphasize the plate-like structure of hydroxyapatite crystals, best highlighted in Ca-concentration gradient maps from a dataset of over 10×10^6 ions, shown in Fig. 3. We find that the arrangement of Ca-rich mineral structures depends on their location or orientation within the sample. They appear as plates adjacent to C-rich regions (Fig. 3b) or as circular-like shapes encompassing C-rich and N-rich (not shown) regions that resemble fibrillar like collagen structures, although slightly smaller in diameter (Fig. 3c). This finding, and the general observation that the locations of Ca and C-rich regions are complementary to one another (Fig. 4), could further support the theory that some of the mineral component of bone exists as extrafibrillar mineral exterior to the gap zones in collagen fibril arrangement[22,23], also described as mineral lamellae in other works[7]. Since the orientation of collagen in this bone sample from the maxilla is difficult to predetermine, we believe that future studies that restrict APT sample geometry to known collagen arrangements, such as in long bones, would aid in deciphering the location of hydroxyapatite within or exterior to collagen fibrils. To better visualize the overlay of organic matrix (C-rich) and inorganic mineral (Ca-rich) components, we refer readers to the Movie S1.

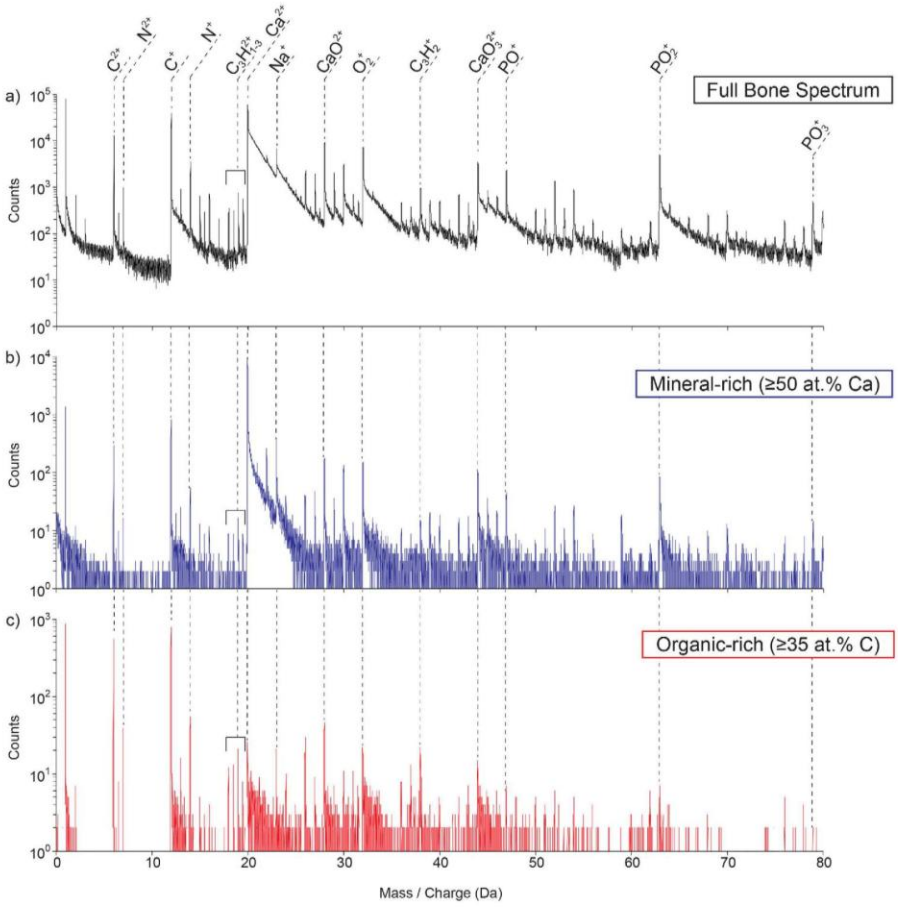

Figure 2. APT mass spectra of bone. Typical mass spectra for an APT analysis of human bone (**a**), as well as subvolumes corresponding to mineral Ca-rich (**b**), and matrix C-rich phases (**c**). The sub-volumes in (**b,c**) were selected as regions with ≥50 at.% Ca, and ≥35 at.% C, respectively. Select ionic species are also indicated on the spectra.

Co-localization of elements. Bone contains many trace elements such as Na, Mg, F and Sr. Studies with secondary ion mass spectroscopy (SIMS) have suggested that Na is located within the organic phase of bone[24]. APT of other mineralized tissues, including elephant tusk dentin and the invertebrate chiton, have detected the co-localization of Na^+ and Mg^{2+} ions with collagen, and attribute this to the presence of specific ion binding proteins or proteoglycans located in organic fibers[15,16]. Herein, Na has been found in throughout the bone, but is most concentrated in regions co-localized with the C-rich organic collagenous and non-collagenous protein components of bone (Fig. 4). When we plot compositions across a linear region of the reconstructed volume (Fig. 5), we can identify organic-inorganic boundaries as the regions showing sharp changes in composition between mineral (Ca-rich) and matrix (C-rich) regions, shown in the red and blue curves of Fig. 5. Adding Na to this plot (green curve, Fig. 5), we note that there are consistently slight enrichments in Na at the organic-inorganic interfaces, as marked by arrows (Fig. 5). While the localization of Na is clear in this work, similar conclusions for Mg are much more difficult to draw due to ambiguity in APT mass spectra caused by overlap between the major peaks of Mg and C in the mass spectra. Further explained figuratively in Fig. S2, the dominant peaks for Mg and C are $^{24}Mg^{2+}$ and $^{12}C^+$, which both appear at a mass:charge value of 12 Da. It could be confirmed that Mg and C co-localize by analyzing the location of $^{24}Mg^+$ ions at 24 Da, but that peak may also exhibit overlap with C, in the form of $^{12}C_2^+$ ions. As there are 3 possible isotopes for Mg: ^{24}Mg, ^{25}Mg, and ^{26}Mg, the minor isotopes of ^{25}Mg and ^{26}Mg could show peaks free of overlap, and confirm the co-localization of Mg with C. The $^{25}Mg^{2+}$ peak at 12.5 Da is observed for the Ca-rich regions, confirming the presence of trace amounts of Mg in the mineral component of the bone. However, the opposite is found for the C-rich collagen, where that peak is not observed at a sufficient level to appear from behind the thermal tail of the major $^{12}C^+$ peak at 12 Da. Therefore, in light of the uncertainty in identifying Mg in the collagen component, we are wary of drawing conclusions on the co-localization of Mg with C as seen in APT of other biominerals. Conversely, the peak for $^{23}Na^+$ at 23 Da may also be somewhat overlapped, in this case by the $^{40}Ca^{2+}$ thermal tail extending from 20 Da. However, we can confidently claim co-localization of Na and C because the $^{23}Na^+$ is found to be enriched in areas of the collagen

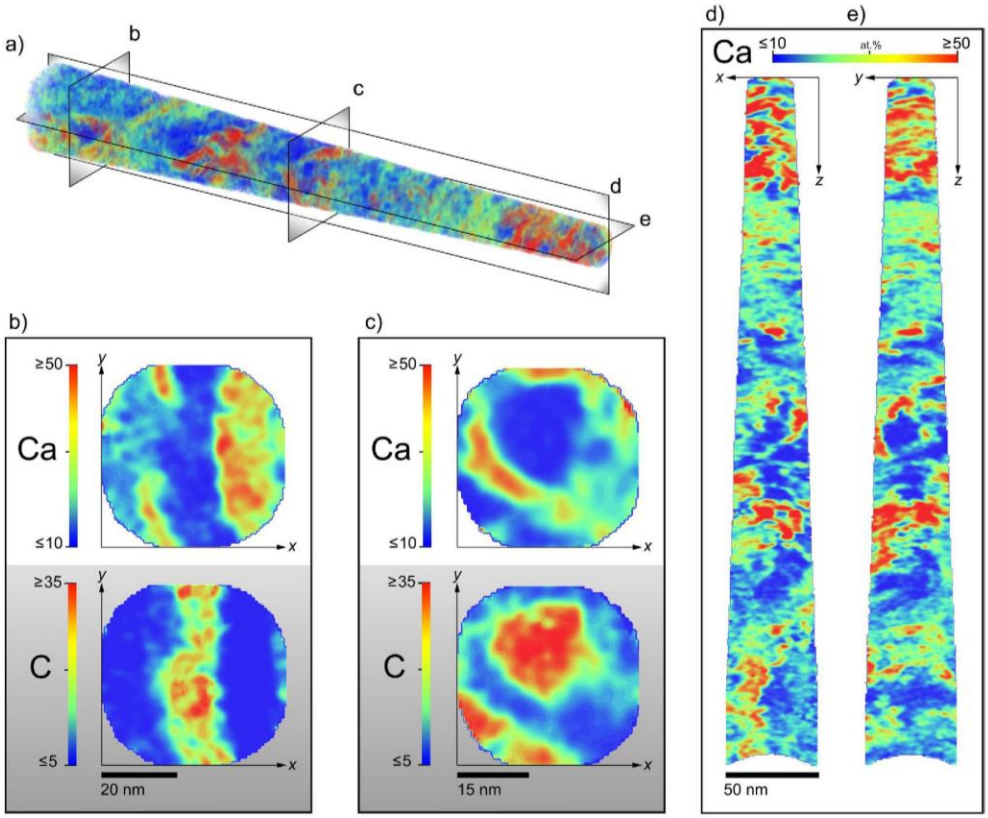

Figure 3. Mineral gradients in bone. 3D rendering shows the volume concentration of Ca, representing bone mineral, throughout a human bone specimen (**a**). Sections perpendicular to the specimen axis (**b,c**) and orthogonal sections parallel to the specimen axis (**d,e**) reveal details in structure variation. Sections perpendicular to the specimen axis highlight (**b**) alternating mineral and collagen-rich bands (shown by complementary C concentration maps), and (**c**) mineral rich regions surrounding circular organic-rich collagen fibrils, potentially locations of extrafibrillar mineral. Plate like crystals are clear in (**d,e**) showing alternating Ca-rich and deficient clusters that are on the order of 50–70 nm wide.

Element	Concentration from APT (at.%)
O	38.81 ± 4.18
Ca	27.44 ± 3.30
C	17.97 ± 6.19
P	12.28 ± 1.02
N	2.86 ± 0.35
Na	2.52 ± 0.80
Mg	0.15 ± 0.04

Table 1. Composition of human bone as measured by APT. Average concentrations of elements detected in human bone from APT data, with results weighted based on the total number of ions in each acquired dataset.

component, precisely where $^{40}Ca^{2+}$ is not. Therefore, within these regions of low Ca concentration, the $^{23}Na^{+}$ ion peak unambiguously represents Na, and there is no significant overlap with $^{40}Ca^{2+}$. A full list of ranged ion species is found in Table S1. Our findings clearly demonstrate that APT is capable of detecting trace elements such as Mg and Na, and we can confidently state that Na is segregated into areas associated with organic-rich regions, and further enriched at organic-inorganic boundaries, while Mg can only be confirmed within the mineral phase, likely as Mg-substituted bone mineral.

While related results from other biomineral-based specimens are interesting, the significance of the current findings in human bone, compared to invertebrates and other vertebrates with drastically different skeletal structures than humans, is marked. APT is presently the only technique available to confirm the elemental heterogeneities we have shown in human bone at the near sub-nanometer length scale. It is important to note that in this study, human bone from the maxilla was not retrieved in a known orientation, i.e. not perpendicular or parallel

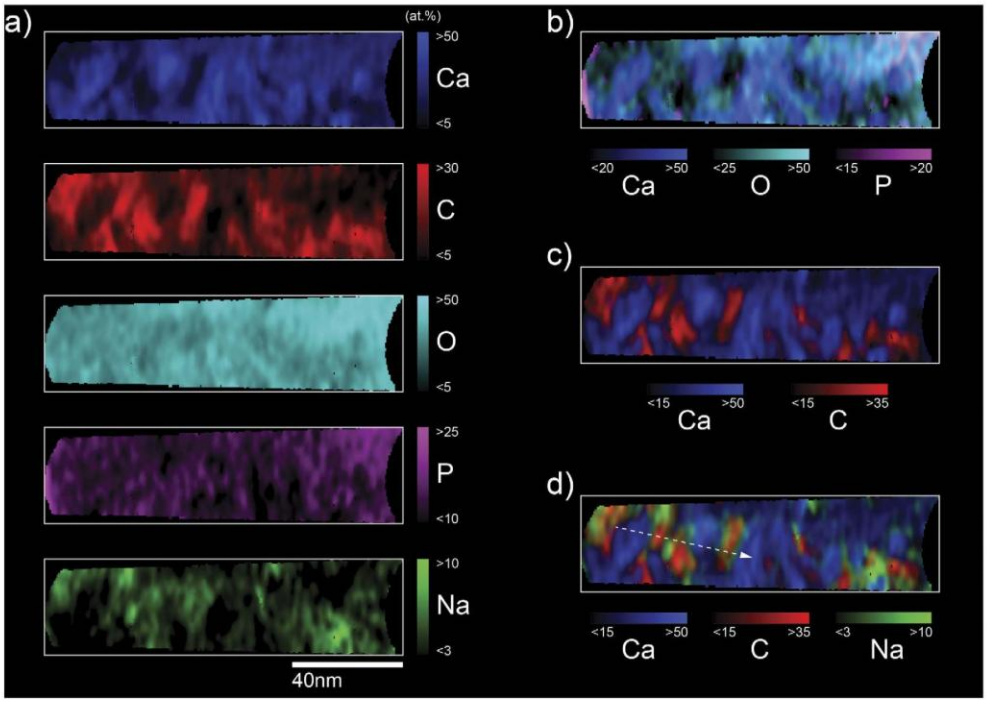

Figure 4. Composition mapping of major and minor elements in human bone by APT. The main components of bone (Ca, C, O, P and Na) from an 8 nm thick APT volume section (**a**). The mineral-rich elements of Ca, O, and P (**b**), are predominantly spatially inverse from regions of organic collagen fibrils (C-rich), as shown in (**c**). The Na concentration map overlaid onto the Ca, C concentration maps in (**d**) suggests the co-localization of Na with the organic components of bone, and at organic-inorganic interfaces. The dashed line in (**d**) indicates the region plotted in Fig. 5.

to any loading or known anatomical feature. In the future, selecting a specimen from a very well characterized anatomical location could provide easier interpretation of APT data. For example, collagen fibrils and bone mineral generally align along the long-axis of long bones – providing this *a priori* information into the assignment of structures would simplify ambiguity in reconstruction.

Conclusions

This work demonstrates the first successful APT of human bone, further improved by the correlation to STEM images to ensure accurate reconstruction. This near-atomic scale view highlights chemical heterogeneities and trace element detection of Mg and Na in human bone. The advanced resolution and three-dimensional chemical mapping capabilities of APT provide a platform for further investigation of other mineralized tissues, particularly with ideally prepared samples and operating conditions.

The low detection limits of APT open a new realm of characterization possibilities. In particular, it offers the opportunity to investigate the role of chemical heterogeneities within bone tissue at mineralization fronts, including both natural, i.e. osteonal structures, and engineered, i.e. implant-bone interfaces[19,25]. Furthermore, with continued technical advancements in APT, such as development of cryo-APT, we may be able remove ambiguity introduced by sample preparation, such as dehydration, of bone with the analysis of cryogenically frozen bone. This work has also highlighted the complex challenges still remaining with the successful acquisition and interpretation of APT data from such highly heterogeneous and organic-based non-conductive materials. Further development towards standards for data analysis of such materials is needed.

This successful APT of human bone, which highlighted the co-localization of Na with organic components and at inorganic-organic interfaces, and the detection of trace elements of Mg in bone mineral, sets the stage for further work in more complex scenarios of biomineralization. It is clear that a multitude of trace biomineralization details could be unveiled by further exploiting the chemical and spatial sensitivity of APT of human bone as we've demonstrated herein.

Methods

Bone sample preparation. The human bone used in this study was received with ethical approval from Biobank 513 at the Department of Biomaterials, University of Gothenburg, Sweden upon the removal of a fractured dental implant in place for 47 months in the maxilla of a 66-year old female patient (Courtesy of Drs. Thomsen and Palmquist) and studied with ethical approval from the Integrated Research Ethics Board at McMaster University, all experiments were performed in accordance with relevant guidelines and regulations.

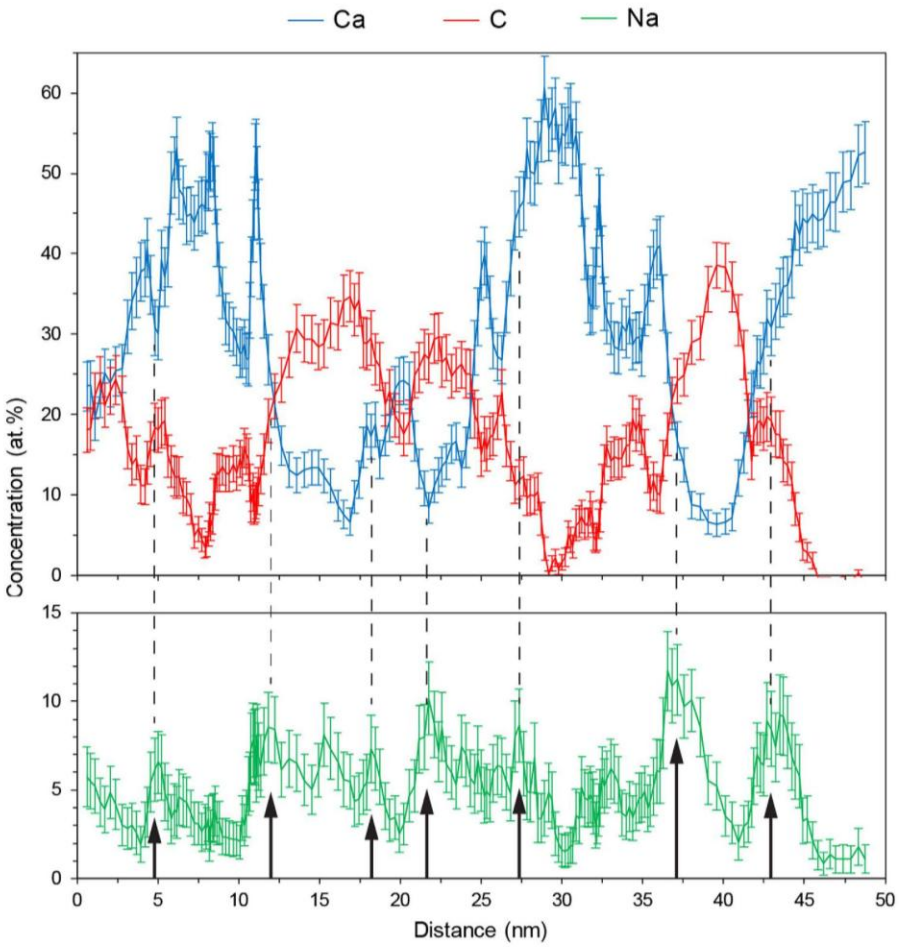

Figure 5. Composition profiles of Ca, C and Na. 1-D atomic concentration profiles for Ca, C and Na show that the concentrations of Ca and C are revealed to fluctuate opposite to each other, according to the relative amounts of mineral and organic phases being sampled. Na is predominantly co-localized with C, but frequently exhibits concentration peaks at mineral-organic interfaces (as indicated by arrows). These profiles were obtained by sampling the dataset shown in Fig. 4d, using a $5 \times 5 \times 50$ nm sub-volume.

The sample was fixed in formalin, dehydrated in a graded series of ethanol and embedded in plastic resin (LR White, London Resin Company, UK) according to a previous publication[26]. The embedded bloc was cut longitudinally and a bone region was selected for further study. APT on the LR White resin only was conducted to assist in eliminating ambiguities in ranging the bone dataset, and is included in Fig. S3.

STEM and APT sample preparation. Needle-shaped samples for correlative STEM imaging and APT were produced using a dual-beam focused ion beam (FIB) instrument (NVision 40, Carl Zeiss, Germany) and established protocols for APT sample production[27], Fig. S1. A site in mature lamellar bone, away from large features such as blood vessels, cement lines and osteocytes, was selected by viewing the specimen with secondary and back-scattered electron imaging in the FIB-SEM. A layer of tungsten ($10\,\mu m \times 2\,\mu m \times 0.5\,\mu m$) was deposited to protect the site of interest prior to rough milling of trenches and lift-out of a wedge-shaped sample. Using tungsten deposition, the lift-out wedge was either attached to the top of Si posts (CAMECA Scientific Instruments, Madison, WI) or to the top of electropolished tungsten wires mounted in 1.8 mm copper tubes. The mounted wedges were annularly milled into needles with diameters ranging between 56 nm and 180 nm. Initial milling was done using a 30 kV beam and successively lower currents (150-10 pA). A 10 kV 80 pA beam was used for final sharpening to minimize any potential damage or Ga ion implantation.

STEM methods. The needle-shaped samples produced by FIB on tungsten wires were mounted in a Model 2050 on-axis rotation tomography holder (E.A. Fischione Instruments, Inc., Export, PA) and imaged in a Titan 80–300 TEM (FEI Company, The Netherlands) operated at 300 kV using a high-angle annular dark-field (HAADF) detector. To avoid sample damage prior to APT, only three images were recorded at −60°, 0°, and +60° tilt at a magnification of 160 k times.

APT methods. Experiments on the needle-shaped specimens were conducted using a LEAP 4000XHR (CAMECA Scientific Instruments, Madison, WI). An ultraviolet laser pulse ($\lambda = 355$ nm) was used to incite field evaporation from the sample. Samples would frequently fracture before yielding a reasonable amount of data, with ~60% of samples yielding more than 1×10^6 ions, and only ~25% yielding more than 3×10^6 ions. The low yield of samples made optimization of experimental parameters difficult, so sample temperature (~43 K) and laser pulse rate (160 kHz) were kept constant, but the evaluation of laser pulse energy was attempted. Laser energies of 16, 75, 90, and 120 pJ were used for analysis, with 75 pJ and 90 pJ appearing to both yield the best quality data, considering both background counts (Fig. S4) and the "thermal tails" created by slow cooling of the specimen following a laser pulse (Fig. S5). Compositions appear consistent within this range of laser energies (Fig. S6); however, the small number of analyzed datasets makes it difficult to separate trends in the data from natural variability between samples. The pressure of the analysis chamber was $<3.7 \times 10^{-9}$ Pa. A target evaporation rate of 0.005 ions/pulse was maintained through varying the electric field on the sample, by means of controlling the DC voltage applied to the sample (typically 1.5–3.5 kV). Data was reconstructed using the Integrated Visualization and Analysis Software package (IVAS v3.6.6, CAMECA Scientific Instruments, Madison, WI). The reconstruction assumes the shape of a hemispherical tip on a truncated cone, with the shank half angle measured from STEM images. To improve the spatial accuracy of the reconstructions, the evaporation field would be estimated such that the Ca-rich features in the reconstruction were consistent with the bright contrast regions in the STEM images. The average evaporation field for human bone was determined to be $F = 15$ V/nm. The initial radius was calculated using the initial DC voltage applied to the specimen, given this evaporation field. A field factor of $k = 3.3$ and an image compression factor of $\zeta = 1.65$ were used for all reconstructions. The average atomic volume was calculated from the hydroxyapatite unit cell (excluding H atoms)[15]. A high percentage of detected ions (70–80%) appear in the mass spectrum not as part of main ion peaks, but in the thermal tails following major peaks. To avoid ambiguity in assigning ionic species, these thermal tails were left un-ranged, and only the main ion peaks were used for reconstruction. This large discrepancy between detected and reconstructed ions was accounted for by modifying the detection efficiency parameter during the reconstruction. For most datasets, a value of $\eta = 0.09$ was used. Unidentified peaks from the mass spectrum were included in the reconstruction, which accounted for <8% of the total ranged ions. Where possible, unidentified ions are indicated as being found coincident with either the mineral (i.e. Ca-rich) or organic (i.e. C-rich) regions of the datasets, Table S1. For the analysis of elemental distributions, all identified ion peaks were used, with complex ions decomposed into their atomic components. See Table S1 for a complete list of ranged ions.

References

1. Currey, J. D. *The structure of bone tissue.* (Bones: Structure and mechanics, 2002).
2. Reznikov, N., Shahar, R. & Weiner, S. Bone hierarchical structure in three dimensions. *Acta Biomaterialia* **10,** 3815–3826 (2014).
3. Gupta, H. S. *et al.* Cooperative deformation of mineral and collagen in bone at the nanoscale. *PNAS* **103,** 17741–17746 (2006).
4. Zimmermann, E. A., Barth, H. D. & Ritchie, R. O. The Multiscale Origins of Fracture Resistance in Human Bone and Its Biological Degradation. *JOM* **64,** 486–493 (2012).
5. Tao, J. *et al.* Energetic basis for the molecular-scale organization of bone. *Proc. Natl. Acad. Sci. USA* **112,** 326–331 (2015).
6. Reznikov, N., Shahar, R. & Weiner, S. Three-dimensional structure of human lamellar bone: The presence of two different materials and new insights into the hierarchical organization. *Bone* **59,** 93–104 (2014).
7. Schwarcz, H. P., McNally, E. A. & Botton, G. A. Dark-field transmission electron microscopy of cortical bone reveals details of extrafibrillar crystals. *J. Struct. Biol.* **188,** 240–248 (2014).
8. Cölfen, H. Biomineralization: A crystal-clear view. *Nature Publishing Group* **9,** 960–961 (2010).
9. Mueller, R. Hierarchical microimaging of bone structure and function. *Nat Rev Rheumatol* **5,** 373–381 (2009).
10. Davies, E. *et al.* Citrate bridges between mineral platelets in bone. *Proc. Natl. Acad. Sci. USA* **111,** E1354–E1363 (2014).
11. Mandair, G. S. & Morris, M. D. Contributions of Raman spectroscopy to the understanding of bone strength. *BoneKEy Reports* **4,** 1–8 (2015).
12. Schrof, S., Varga, P., Galvis, L., Raum, K. & Masic, A. 3D Raman mapping of the collagen fibril orientation in human osteonal lamellae. *J. Struct. Biol.* **187,** 266–275 (2014).
13. Kelly, T. F. & Miller, M. K. Atom probe tomography. *Review of Scientific Instruments* **78,** 031101 (2007).
14. Gault, B. *et al.* Design of a femtosecond laser assisted tomographic atom probe. *Review of Scientific Instruments* **77,** 043705 (2006).
15. Gordon, L. M., Tran, L. & Joester, D. Atom probe tomography of apatites and bone-type mineralized tissues. *ACS Nano* **6,** 10667–10675 (2012).
16. Gordon, L. M. & Joester, D. Nanoscale chemical tomography of buried organic-inorganic interfaces in the chiton tooth. *Nature* **469,** 194–197 (2011).
17. Gordon, L. M. *et al.* Dental materials. Amorphous intergranular phases control the properties of rodent tooth enamel. *Science* **347,** 746–750 (2015).
18. Gordon, L. M. & Joester, D. Mapping residual organics and carbonate at grain boundaries and the amorphous interphase in mouse incisor enamel. *Frontiers in Physiology* **6,** 57 (2015).
19. Karlsson, J., Sundell, G., Thuvander, M. & Andersson, M. Atomically resolved tissue integration. *Nano Lett.* **14,** 4220–4223 (2014).
20. Huang, J., Wang, X. & Grandfield, K. FIB Preparation of Bone-Implant Interfaces for Correlative On-Axis Rotation Electron Tomography and Atom Probe Tomography. *Microsc Microanal* **20,** 352–353 (2014).
21. Biyikli, S., Modest, M. F. & Tarr, R. Measurements of thermal properties for human femora. *J. Biomed. Mater. Res.* **20,** 1335–1345 (1986).
22. McNally, E. A., Schwarcz, H. P., Botton, G. A. & Arsenault, A. L. A Model for the Ultrastructure of Bone Based on Electron Microscopy of Ion-Milled Sections. *PLoS ONE* **7,** e29258 (2012).
23. Alexander, B. *et al.* The nanometre-scale physiology of bone: steric modelling and scanning transmission electron microscopy of collagen-mineral structure. *Journal of The Royal Society Interface* **9,** 1774–1786 (2012).
24. Bushinsky, D. A., Gavrilov, K. L., Chabala, J. M. & Levi-Setti, R. Contribution of organic material to the ion composition of bone. *J. Bone Miner. Res.* **15,** 2026–2032 (2000).
25. Grandfield, K. Bone, implants, and their interfaces. *Phys. Today* **68,** 40–45 (2015).
26. Shah, F. A., Nilson, B., Brånemark, R., Thomsen, P. & Palmquist, A. The bone-implant interface - nanoscale analysis of clinically retrieved dental implants. *Nanomedicine: Nanotechnology, Biology, and Medicine*, doi: 10.1016/j.nano.2014.05.015 (2014).
27. Thompson, K. *et al. In situ* site-specific specimen preparation for atom probe tomography. *Ultramicroscopy* **107,** 131–139 (2007).

Acknowledgements

This work was supported by a Discovery Grant from the Natural Sciences and Engineering Research Council of Canada (NSERC). X.W. acknowledges support from the Ontario Trillium Scholarship. Microscopy was performed at the Canadian Centre for Electron Microscopy (CCEM) at McMaster University, a facility supported by NSERC and other government agencies. We gratefully acknowledge the continued support and feedback from CCEM Scientific Director and colleague Prof. Gianluigi Botton. We thank Dr. Anders Palmquist and Prof. Peter Thomsen at the University of Gothenburg for providing the bone sample. We thank Prof. Henry F Schwarcz for his comments.

Author Contributions

K.G. designed the experiments. B.L. performed atom probe experiments; X.W. and K.G. performed electron microscopy. B.L. and X.W. analyzed the data. K.G. prepared the manuscript with major contributions and revisions from X.W. and B.L.

Additional Information

Supplementary information accompanies this paper at http://www.nature.com/srep

Competing financial interests: The authors declare no competing financial interests.

How to cite this article: Langelier, B. *et al.* Atomic scale chemical tomography of human bone. *Sci. Rep.* **7**, 39958; doi: 10.1038/srep39958 (2017).

Publisher's note: Springer Nature remains neutral with regard to jurisdictional claims in published maps and institutional affiliations.

Supplementary Information:

Atomic scale chemical tomography of human bone

Brian Langelier[1], *Xiaoyue Wang*[1], *Kathryn Grandfield*[1]†*

[1]Department of Materials Science and Engineering, McMaster University, Hamilton, ON, L8S 4L7, Canada; and †School of Biomedical Engineering, McMaster University, Hamilton, ON, L8S 4L7, Canada

SUPPLEMENTARY MATERIALS:

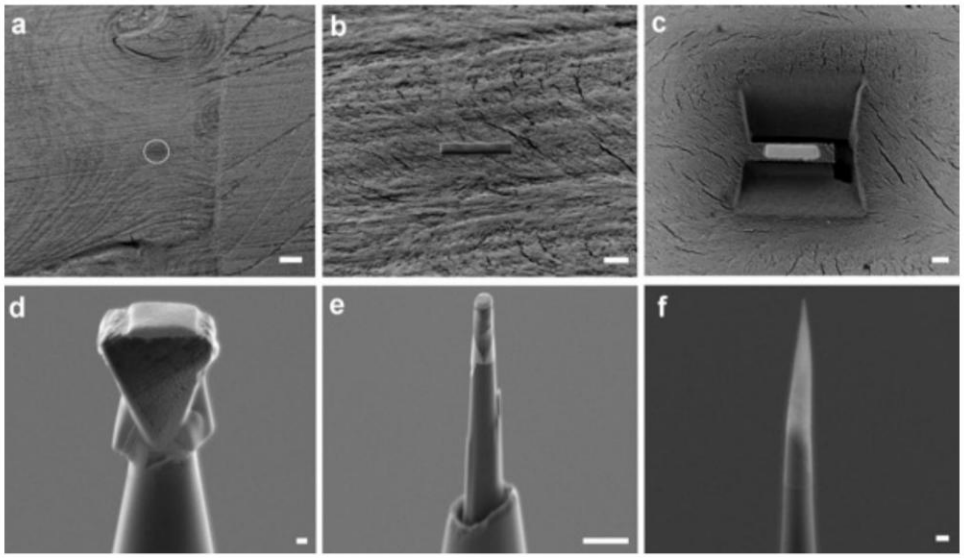

Figure S1. Focused ion beam sample preparation method. Following (a-f): site selection, protection with tungsten deposition, milling of rough trenches, lift-out and attachment of wedge to the tip of an electropolished W needle, and annular milling to a final needle-shaped pillar for APT. Scale bars (a) 40 μm, (b-e) 4 μm, (f) 200 nm.

Table S1. Ranged ion assignments from APT mass spectra

Mass/Charge (Da)	Ion
1	H^+
2	H_2^+
3	H_3^+
6, 6.5	C^{2+}
7	N^{2+}
12, 13	C^+
12.5	Mg^{2+}
14	N^+
15	NH^+
15.5	P^{2+}
16	O^+
17	OH^+
18	H_2O^+
18.5	C_3H^{2+}
19	$C_3H_2^{2+}$
19.5	$C_3H_3^{2+}$
20, 22	Ca^{2+}
23	Na^+
24	Mg^+
26	P_2O^{3+}
27	NaP^{2+}
27.5	$NaPH^{2+}$
28	CO^+
29	$CaPO^{3+}$
30	NO^+
31	P^+
31.5	P_2H^{2+}
32	$O2^+$
36	CaO_2^{2+}
37	C_3H^+
38	$C_3H_2^+$
39	P_2O^{2+}
40	Ca^+
41	*Unidentified*[1]
42	$Ca_3O_3^{4+}$
43	CP^+
43.5	$CaPO^{2+}$
44	CaO_3^{2+}
45	*Unidentified*[1]
46	P_2NO^{2+}
47	PO^+
48	Ca_2O^{2+}

Mass/Charge (Da)	Ion
49	*Unidentified*
50	*Unidentified*
50.5	*Unidentified*
51	*Unidentified*
52	CaO_4^{2+}
53	$Ca_2PO_3^{3+}$
54	*Unidentified*[1]
55	P_2Ca^{2+}
56	CaO^+
57	$CaOH^+$
58	*Unidentified*
59	*Unidentified*
60	*Unidentified*
61	*Unidentified*[2]
62	P_2^+
63	PO_2^+
64	PO_2H^+
66	*Unidentified*[1]
67	*Unidentified*
68	*Unidentified*[1]
69, 71	Ga^+
70	*Unidentified*[1]
72	CaO_2^+
73	*Unidentified*
74	*Unidentified*
75	*Unidentified*
76	*Unidentified*[2]
78	P_2O^+
79	PO_3^+
80	*Unidentified*[1]
81	*Unidentified*[1]
82	*Unidentified*
83	*Unidentified*
88	*Unidentified*
89	*Unidentified*
90	*Unidentified*
91	*Unidentified*[1]
92	*Unidentified*
94	*Unidentified*
96	*Unidentified*
100	*Unidentified*[2]
102	*Unidentified*

Mass/Charge (Da)	Ion
102.5	*Unidentified*[1]
103	*Unidentified*
105	*Unidentified*[1]
106	*Unidentified*[1]
107	*Unidentified*[1]
119.5	$CaPO_3^+$
134	$P_4O_9^{2+}$
142	$P_2O_5^+$
143	$P_2O_5H^+$
158	*Unidentified*[1]
205	*Unidentified*

[1]*Unidentified ion most common in mineral regions*

[2]*Unidentified ion most common in organic regions*

Note: Unidentified ions correspond to < 8 ionic % of total ranged ions.

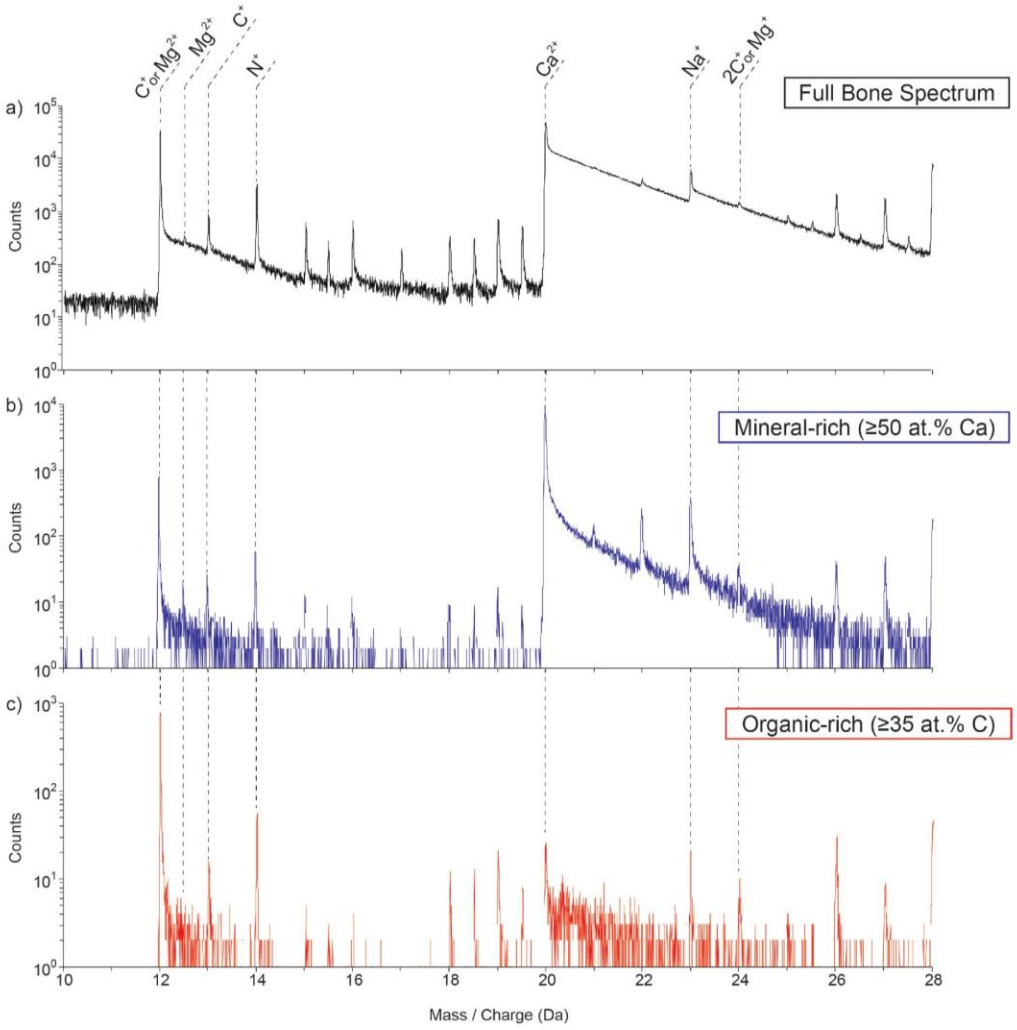

Figure S2. APT mass spectra over 10-28 Da range typical for human bone (a), as well as sub-volumes corresponding to Ca-rich mineral (≥ 50 at. % Ca) (b), and C-rich organic matrix (≥ 35 at. % C) phases (c). Select ionic species are also indicated on the spectra. The presence of the $^{23}Na^{+}$ peak at 23 Da shows that Na is detected in both the mineral and organic phases, but appears at relatively higher levels in the latter. Trace Mg is detected in the mineral, but cannot be disambiguated from C in the organic matrix phase due to overlap between $^{24}Mg^{2+}$ and $^{12}C^{+}$ at 12 Da, and $^{24}Mg^{+}$ and $^{12}C_2^{+}$ at 24 Da, and the $^{25}Mg^{2+}$ peak at 12.5 Da not appearing above the thermal tail for the $^{12}C^{+}$.

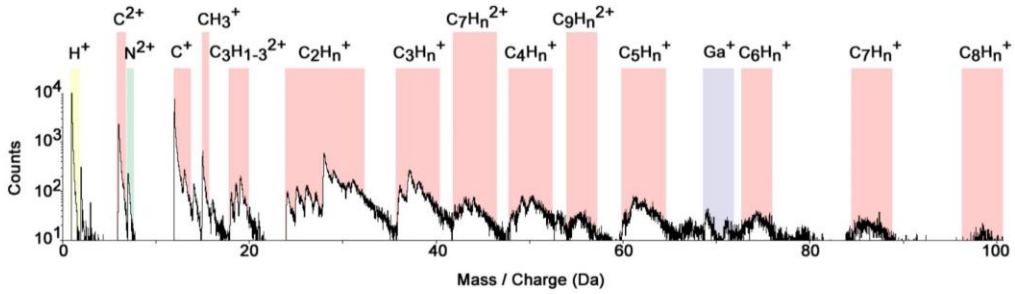

Figure S3. APT Mass Spectra of LR White Polymer Resin. APT mass spectrum from the embedding resin, with major ions labeled (n = 0, 1, 2 … 3-5). Note Ga^+ ions are present due to FIB preparation.

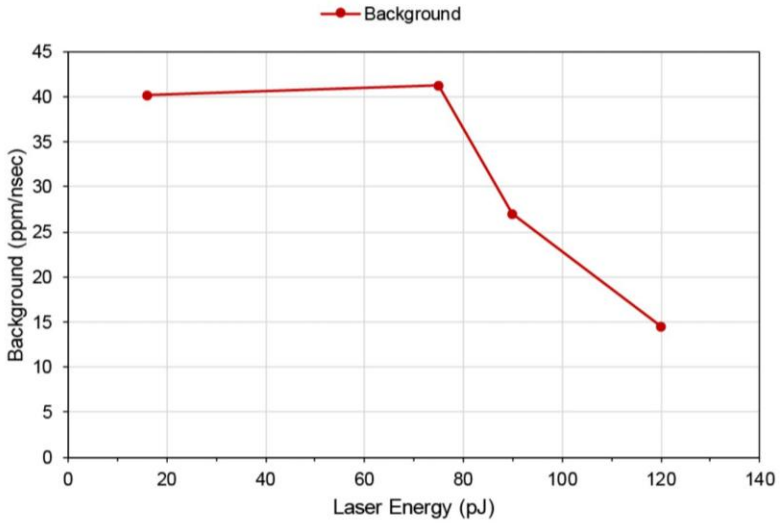

Figure S4. Effect of laser energy on background counts. The measured background signal is plotted for datasets obtained at 16, 75, 90 and 120 pJ. It is clear that below 90 pJ, the background level increases dramatically. This is the result of an increasing DC field needed to maintain evaporation at lower laser energies, and the resulting off-pulse DC evaporation it can produce.

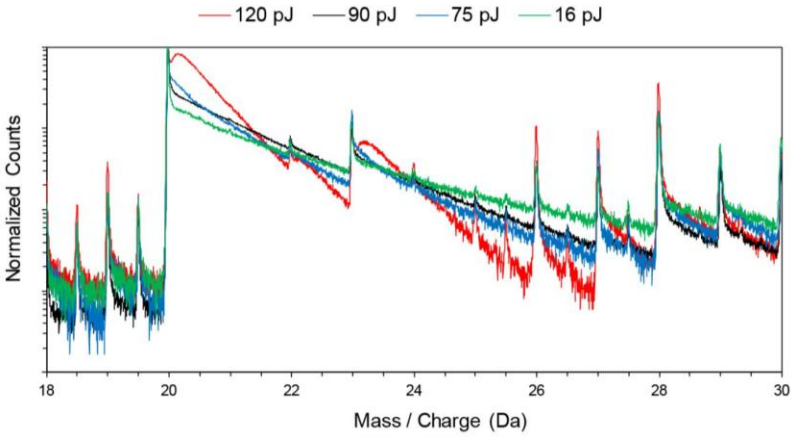

Figure S5. Effect of laser energy on the peaks in the mass spectrum. The mass spectrum showing the major $^{40}Ca^{2+}$ peak, normalized based the height of that peak, is plotted for datasets obtained at 16, 75, 90 and 120 pJ. The high laser energy of 120 pJ shows the lowest background levels, but also the largest thermal tails immediately following the peaks. The lowest laser energy of 16 pJ has the smallest tail in the vicinity of the peak, but it decays the least extending out to higher Da, due to the contribution from the high background level for that laser energy. Both the 75 pJ and 90 pJ datasets appear to provide the optimum balance between low background and short thermal tails.

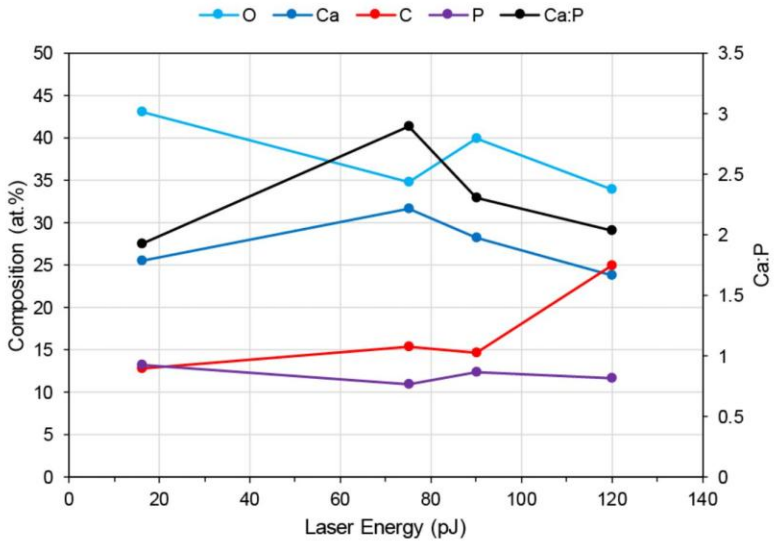

Figure S6. Effect of laser energy on measured composition. Compositions for major elements, as well as the Ca:P ratio, are plotted for datasets obtained at 16, 75, 90 and 120 pJ. No clear trends emerge over the range of 16-90 pJ, with only the 120 pJ data exhibiting a relatively high C concentration, and low O and Ca concentrations. This discrepancy may be due to sample-to-sample variability however.

Movie S1. APT of over 10 million ions of human bone showing Ca and C gradient maps, representing mineral and organic regions, respectively. (uploaded separately)